HADRONIC PHYSICS AND SCALE SETTING FROM LATTICE QCD WITH WILSON-TYPE FERMIONS

Memoria de Tesis Doctoral realizada por

Alejandro Sáez Gonzalvo

presentada ante el Departamento de Física Teórica
de la Universidad Autónoma de Madrid
para optar al Título de Doctor en Física Teórica

Supervisor: **Prof. Dr. Gregorio Herdoíza**

Instituto de Física Teórica UAM-CSIC
Departamento de Física Teórica
Facultad de Ciencias
Universidad Autónoma de Madrid

2024

A Joaquín.

Nature is the proof of dialectics, and it must be said for modern science that it has furnished this proof with very rich materials increasingly daily [...]

— Engels, Anti-Dühring

It is precisely the alteration of nature by men, not solely nature as such, which is the most essential and immediate basis of human thought.

— Engels, Dialectics of Nature.

ABSTRACT

The search for New Physics requires precise theoretical calculations that allow to discern deviations from the Standard Model in experiments. A rich arena for the search for New Physics is the flavor sector of the Standard Model and Quantum Chromodynamics. Recent experiments have revealed anomalies in B meson decays and the anomalous magnetic moment of the muon, to name a few. In all these processes, Quantum Chromodynamics plays a crucial role, hence the importance of performing precise theoretical predictions of strong interaction phenomena. Lattice Field Theory provides with a first-principles framework which allows to study strongly coupled theories like QCD.

In this thesis, we study a mixed action Lattice QCD setup aimed at high precision calculations of light and charm physics. The setup combines $N_f = 2 + 1$ $\mathcal{O}(a)$ non-perturbatively improved quarks in the sea with $N_f = 2 + 1 + 1$ twisted mass quarks in the valence, taking advantage of automatic $\mathcal{O}(a)$ improvement at maximal twist. This ensures absence of $\mathcal{O}(a)$ effects proportional to heavy valence masses, which is of particular importance for charm physics.

Here we focus on high precision scale setting and its impact in the study of charm physics using our mixed action setup. The use of the mixed action requires matching the physical quark masses of both the sea and valence sectors in order to recover unitarity of the theory in the continuum, in addition to tuning to maximal twist to obtain automatic $\mathcal{O}(a)$ improvement. With this setup, we set the scale using the pion and kaon decay constants and the gradient flow scale t_0. We employ model variation techniques in order to assess for systematic uncertainties and quote a high precision result for t_0 and the lattice spacing in physical units, with controlled continuum and physical point extrapolations. Furthermore we perform a study of the charm quark mass and of charmed mesons decay constants exploiting automatic $\mathcal{O}(a)$ improvement, and quote physical results using our determination of the scale t_0. Our results are among the most precise in the community for Wilson-like lattice regularizations.

RESUMEN

Blabla

PUBLICATIONS

[1] Andrea Bussone, Alessandro Conigli, Julien Frison, Gregorio Herdoíza, Carlos Pena, David Preti, Alejandro Sáez, and Javier Ugarrio. "Hadronic physics from a Wilson fermion mixed-action approach: charm quark mass and $D_{(s)}$ meson decay constants." In: *Eur. Phys. J. C* 84.5 (2024), p. 506. DOI: 10.1140/epjc/s10052-024-12816-4. arXiv: 2309.14154 [hep-lat].

[2] Andrea Bussone, Alessandro Conigli, Julien Frison, Gregorio Herdoíza, Carlos Pena, David Preti, Alejandro Sáez, Javier Ugarrio, and Jose Angel Romero. "Hadronic physisc from a Wilson fermion mixed-action approach I: Setup and scale setting." In: (Submitted for publication, 2024).

[3] Andrea Bussone, Alessandro Conigli, Gregorio Herdoiza, Julien Frison, Carlos Pena, David Preti, Jose Angel Romero, Alejandro Saez, and Javier Ugarrio. "Light meson physics and scale setting from a mixed action with Wilson twisted mass valence quarks." In: *PoS* LATTICE2021 (2022), p. 258. DOI: 10.22323/1.396.0258.

[4] Alessandro Conigli, Julien Frison, Gregorio Herdoíza, Carlos Pena, Alejandro Sáez, and Javier Ugarrio. "Towards precision charm physics with a mixed action." In: *PoS* LATTICE2022 (2023), p. 351. DOI: 10.22323/1.430.0351. arXiv: 2212.11045 [hep-lat].

[5] Alejandro Saez, Alessandro Conigli, Julien Frison, Gregorio Herdoíza, and Carlos Pena. "Determination of the Gradient Flow Scale t_0 from a Mixed Action with Wilson Twisted Mass Valence Quarks." In: *40th International Symposium on Lattice Field Theory*. Jan. 2024. arXiv: 2401.11546 [hep-lat].

[6] Alejandro Saez, Alessandro Conigli, Julien Frison, Gregorio Herdoiza, Carlos Pena, and Javier Ugarrio. "Scale Setting from a Mixed Action with Twisted Mass Valence Quarks." In: *PoS* LATTICE2022 (2023), p. 357. DOI: 10.22323/1.430.0357.

ACKNOWLEDGMENTS

Quiero expresar mi gratitud a la gente que ha estado ahí toda mi vida. En especial a mis amigas Marta Gracia, Marta González, Alicia y Marina. Os conozco desde los 3 años, y tengo mucha suerte de que en todo este tiempo nuestra relación haya acabado cristalizando en lo que es hoy. Sois las mejores amigas que se podría desear. Tenemos muchos recuerdos y anécdotas juntas y ya sois como de mi familia. Quiero en especial agradeceros vuestra amistad, cariño y honestidad en un momento crítico de mi vida; ayudasteis mucho a que todo esté bien. Tengo una suerte infinita de ser vuestro amigo.

Gracias también a mis amigos Elena, Claudia, Dani, Marina, Motis, Ruberte, Juan, Sara y Pablo. Todas sois buenísimas personas. Parece que fue ayer que estábamos todos juntos en los pasillos de la facultad. En especial gracias a Elena y Claudia. Aunque no nos vemos muy a menudo, el cariño que os tengo no desaparece, y me alegro de que nuestra amistad haya crecido tanto desde que nos conocimos por primera vez.

También quiero darles las gracias a mis padres. Gracias por apoyarme desde la carrera, por vuestro cariño y vuestra paciencia. Gracias por vuestros consejos y por buscar siempre lo mejor para mí. Gracias Lucía por el cariño a tu hermano de mente ausente, por aguantarme y por interesarte en mis cosas. Gracias Paz por tu cariño, consejos y comprensión. Gracias a mis abuelos Aquilino y Carmen por vuestro apoyo incondicional y todo el amor que me habéis dado desde pequeño. Gracias a mis tias, tios, primas y primos.

Y por supuesto gracias a Joaquín. Sin ti nada de esto tendría sentido. Trajiste la felicidad a mi vida, y me causas alegría cada día. Gracias por estar siempre presente, por ayudarme a seguir, por estar en los buenos y los malos momentos. Me enseñas a ser mejor persona cada día. Gracias por tu infinita paciencia, por tu perdón, por tu amabilidad, tu cariño, tu alegría y tu risa. Gracias por interesarte en mis obsesiones *reticulares* de *gluones* y *quarks*. Gracias por apoyarme en mi carrera, acompañarme en los momentos difíciles y de incertidumbre, y por recorrerlos a mi lado. Los momentos más felices de mi vida son contigo. Eres la persona más amable, graciosa, inteligente, altruista y especial que conozco. Me siento increíblemente afortunado de compartir mi vida contigo, y estoy profundamente enamorado de ti.

Por último, quiero agradecer a Marisa, José Antonio, Rocío, Víctor y Ñam-Ñam. No exagero si digo que sois como una segunda familia para mí. Desde el primer momento me acogisteis como uno más, y siempre me habéis hecho sentir a gusto, acogido y querido. Siempre habéis sido amables y buenos conmigo, gracias.

En definitiva, gracias a todas las personas que han pasado y que están en mi vida. Gracias por aguantarme con todas mis rarezas, que no son pocas.

Por último, me gustaría agradecer a todo el personal de manten-
imiento y administrativo del IFT. Este edificio no funcionaría sin
vosotras y vosotros.

CONTENTS

Part I

INTRODUCTION

INTRODUCTION

The Standard Model (SM) of particle physics is the theory that describes and unifies three of the four fundamental interactions in Nature: electromagnetism, the weak interaction, and the strong interaction. The theoretical framework in which the SM is formulated is that of Quantum Field Theory (QFT), and the particular theory that describes the strong interaction is Quantum Chromodynamics or QCD[1].

QUANTUM FIELD THEORY AND THE STANDARD MODEL

The 20th century witnessed two pivotal developments in modern physics and our comprehension of Nature: special relativity and quantum mechanics.

First, the theory of special relativity presents a reformulation of Galileo's principle, which afirms that the laws of physics must remain unchanged between two different inertial frames. This reformulation is consistent with the theory of electromagnetism developed by Maxwell in the 19th century and posits that the speed of light is a universal constant. This led to profound consequences, such as time and length dilation, according to which one observer experiences time and distances differently from another, depending on the relative speed of their inertial frames. Additionally, it implies the equivalence of mass and energy, and led to the formulation of the Universe as a 4-dimensional Lorentzian manifold, space-time, in which there is a non-trivial interplay between time and space.

The principle of a constant speed of light and the the upper bound that it induces on signal propagation speed rendered the old Newtonian view of interactions obsolete. According to the latter, the force acting on a particle at a given time depends on the position of all other particles at that moment. This implies an instantaneous transfer of force from one particle to another, which is at odds with the principles of special relativity. Field Theory is the framework that allows to supersede this difficulty. It is based on the concept of fields, which are dynamic objects that fill all of space-time. Mathematically, they are simply functions of space and time. The treatment of fields as the fundamental degrees of freedom is of great assistance in the formulation of theories that are Lorentz invariant and thus compatible with special relativity. One example is Maxwell's theory of electro-

---

1 The main discussion in this Introduction is based on the review [128], all other relevant references can be found in Chapter 1

magnetism, which describes the dynamics of the electric $\vec{E}(\vec{x}, t)$ and magnetic $\vec{B}(\vec{x}, t)$ fields.

On the other hand, quantum mechanics introduces the concept of probability into our description of Nature. The basic idea is that particles are described by wave functions that represent the probability density of finding one particle at a given position in space at some time. Position and momentum are promoted to conjugate operators rather than being considered degrees of freedom. These operators do not commute, which gives rise to Heisenberg's uncertainty principle, according to which it is not possible to know the position and momentum of a particle simultaneously

$$\Delta x \Delta p \geq \hbar.$$

Quantum Field Theory is the framework that unifies quantum mechanics and special relativity. It entails promoting classical fields to quantum operators in a manner analogous to the case of position and momentum in quantum mechanics. This results in a plethora of consequences, including that particles are seen as excitations of an underlying quantum field, the existence of antiparticles and the non-conservation of particle number. The latter is of special importance for any quantum description of a relativistic system, as high-energy collisions can result in the creation and annihilation of particles. Moreover, according to Heisenberg's uncertainty principle, if a particle is placed in a box of size L there will be an uncertainty in its momentum of

$$\Delta p \geq \hbar/L.$$

This gives rise to an uncertainty in the energy of the particle of order $\Delta E \geq \hbar c/L$. When the energy exceeds $2mc^2$ we have enough energy to create a particle-antiparticle pair from the vacuum. This happens at distances of order

$$L = \lambda = \frac{\hbar}{mc},$$

which is the Compton wavelength. At this and smaller distances (or equivalently higher energies) one expects to detect particle-antiparticle pairs in proximity to the original particle, breaking down the very concept of a point-like particle.

Generalizing the concept of fields such that all particles are excitations of some field solves another puzzle of Nature: how can e.g. two electrons separated by a space-like distance (causally disconnected) look exactly the same, like two perfect copies of one another? This is naturally explained if there is a universal field of the electron, since all electrons are simply excitations of this field filling all of space-time.

A key ingredient of QFTs are symmetries, which are described by the mathematical language of groups. Global symmetries are of paramount importance in physics, as they provide with conservation

laws through Noether's Theorem, such as the conservation of energy and momentum. In addition to global symmetries, local or gauge symmetries also play a crucial role. These can be regarded as a redundancy of the theory, so that performing some local transformation of the fundamental fields leaves physics unchanged. Although it may appear impractical to write our theories of Nature in a redundant manner, it is very useful since it allows us to write simple Lagrangians which may have unphysical degrees of freedom that can be eliminated by using gauge redundancy. This is exemplified by the polarization of the photon, which has only two polarizations but in the SM is described by a gauge field with 4 degrees of freedom. Thanks to gauge symmetry, one can eliminate the two remaining unphysical degrees of freedom. Another beautiful property of gauge symmetries is that they allow for a geometric interpretation of interactions: gauge fields can be regarded as the connection in a principal G-bundle, with G the gauge group, and the field strength tensor as the curvature. In this way, all fundamental interactions of Nature can be understood in the light of geometry, just as gravity is in General Relativity.

The gauge symmetry group of the SM is

$$SU(3)_c \times SU(2)_w \times U(1)_Y,$$

where $SU(3)_c$ is the gauge group of the strong interaction (whose charge is called color), $SU(2)_w$ is the gauge group of the weak interaction and $U(1)_Y$ is the gauge group of hypercharge. The Higgs mechanism provides a description of the spontaneous symmetry breaking of the electroweak sector $SU(2)_w \times U(1)_Y$ into that of electromagnetism $U(1)_{em}$, as well as a mechanism for the generation of masses for fundamental particles. The pure gauge interactions depend only on three free parameters, which are the three coupling constants. Matter fields do not introduce any further free parameter, while the addition of the Higgs field introduces 22 new free parameters into the theory, which govern the masses of the elementary particles, flavor mixing angles and CP-violating phases.

Over the decades, the SM has proven extremely successful in passing experimental tests. Notable examples include the discovery of neutral weak currents in 1973, the bottom quark in 1977, the Z and W bosons in 1983 and the agreement of the ratio of their masses between experiment and theory, the discovery of the top quark in 1995, and the Higgs boson in 2012.

Despite the remarkable success of the SM, we know that it cannot be the whole story. On the one hand, it does not explain one of the four fundamental interactions of Nature, gravity. On the other hand, there's no candidate particle in the SM for dark matter, which is estimated to comprise $\sim 85\%$ of the matter in the Universe. In addition, there are other theoretical puzzles, such as the hierarchy problem of the Higgs mass, triviality of the Higgs coupling, the flavor puzzle or the

strong CP problem, which we will briefly discuss below. This indicates that the SM is an effective theory that describes extremely well the Universe at the energy scales probed by modern day colliders, but that there must be some New Physics (NP) at work at high energies, the search of which is the holy grail of modern day particle physics.

One frontier of research for New Physics is the precision frontier. Modern particle physics experiments have achieved a remarkable precision, and in order to detect potential signals of NP, it is of the utmost importance to make theoretical predictions with the same degree of accuracy. One promising avenue for exploration is the study of semileptonic B meson decays. In recent years some anomalies have been observed in these processes, suggesting the potential violation of lepton flavor universality. The most prominent anomalies are observed in the $b \to c\tau\nu$ charged current and in the $b \to s\ell^+\ell^-$ neutral current [36]. Furthermore, neutral currents are suppressed in the SM by the GIM mechanism, making them excelent probes for NP effects. Semileptonic B decays are also important for the determination of the CKM matrix elements, and some tensions have been observed between the exclusive and inclusive determination of the elements V_{ub} and V_{cb} [116]. Another example that has gained particular relevance in recent years is the anomalous magnetic moment of the muon, which has been measured experimentally with an unprecedented precision [15]. However, theoretical consensus for this quantity is yet to be achieved: a data-driven dispersive approach leads to a 4.2σ tension with the experimental value [6], while ab-initio SM calculations lead to a 1.5σ difference [22]. In all these processes QCD plays a crucial role, and thus precise theoretical predictions in this sector of the SM are of the utmost importance. The framework of Lattice Field Theory provides with a very powerful tool for this purpose.

WHY LATTICE FIELD THEORY?

When computing physical observables in QFTs, divergences appear which must be removed in order for the theory to be predictive. This is achieved through the implementation of the renormalization program, which entails the subtraction of the divergences that emerge in physical quantities by means of the redefinition of the parameters of the theory that are not observables, such as field normalizations, masses and couplings. This renormalization program has been successfully applied to the three fundamental interactions described by the SM.

The concept of running coupling constants is introduced by renormalization. Coupling constants are taken to run with the energy in such a way that physical observables remain finite and independent of the energy scale at which divergences are subtracted in the renormalization program. In the case of electromagnetism, the coupling (the electric charge of the electron) decreases at low energies. However, in

the case of Yang-Mills theories such as QCD, the opposite is true, with the coupling becoming stronger at lower energies.

The technology usually employed to study Quantum Field Theory is perturbation theory. It consists of expanding field expectation values in powers of the coupling of the theory, which must be $\ll 1$ in order for the perturbative expansion to be a good approximation. Since as mentioned the QCD coupling constant grows at low energies, in contrast to the case of QED, it is possible to apply perturbation theory to the study of Quantum Electrodynamics at low energies, but not to the study of QCD at these energies. The only other known first-principles method for studying QFTs is Lattice Field Theory. It consists of discretizing space-time into a grid or lattice, with space-time points separated by a non-zero lattice spacing a, and Wick rotating to the Euclidean.

Lattice Field Theory permits a non-perturbative treatment of QFTs, treating the theory as a statistical physics system, computing integrals and expectation values numerically without the need to expand in powers of the coupling. In the case of the strong interaction this is relevant since the main distinguishing phenomena of QCD are caused by its strongly coupled nature. For instance, non-perturbative effects are responsible for confinement, whereby no color charged particles are observed in Nature at low energies. Spontaneous chiral symmetry breaking is also caused by non-perturbative effects, and is responsible for the light mass of pions. Additionally, the theory is expected to dynamically generate a mass gap due to its non-perturbative nature. This implies that the spectrum of QCD does not include any arbitrarily light particle. Even though this is experimentally confirmed and supported by numerical simulations using Lattice Field Theory, there is, at the moment, no conclusive theoretical proof of the QCD mass gap. Obtaining a rigorous theoretical proof for this problem constitutes on of the famous Millennium Prize Problems [101]. Another important aspect of QCD is its vacuum structure, the role of the θ-term and topology of the gauge group. In order to achieve a comprehensive theoretical understanding of all of these features of QCD, as well as to conduct high precision, reliable calculations needed for the search of NP in the precision frontier, it is essential to employ a non-perturbative approach to the theory.

Non-perturbative treatment of QFT is also of great importance for other theoretical reasons. In many popular Beyond the Standard Model (BSM) theories, non-perturbative effects play a central role: in supersymmetric theories (SUSY), non-perturbative effects are invoked to break supersymmetry at low energies. Nearly conformal field theories and technicolor models (which are up-scale versions of QCD) also require a non-perturbative treatment. Moreover, the SM version of the Higgs potential suffers from the triviality problem. This implies that the renormalized Higgs coupling vanishes after perturbative renormal-

ization, unless there is a finite energy cutoff in the theory, implying that the SM is nothing but an Effective Field Theory (EFT) valid up to some energy cutoff. In this scenario, the Higgs mass is expected to receive large contributions from the high-energy scales, rendering it naturally heavy, in contrast to the observed value at CERN. This is referred to as the hierarchy problem. Non-perturbative numerical approaches demonstrate triviality of scalar quartic theories (which is the case of the Higgs potential in the SM). Nevertheless, coupling the scalar to other particle content as in the SM could potentially alter the triviality behavior of the coupling. Once more, these issues can only be addressed by employing a non-perturbative approach. In this manner, Lattice Field Theory provides with a tool that can be used to investigate fundamental theoretical problems of the SM and of QFTs in general.

A MIXED ACTION LATTICE APPROACH TO LIGHT AND CHARM PHYSICS

Having already motivated the need for precision calculations of SM physics involving the strong interaction in order to constrain the search for NP in experiments, the objective of this thesis is to define and implement a mixed action approach for the study of light and charm physics with Lattice QCD. This mixed action employs the Wilson fermion regularization for quarks in the sea, with mass degenerate up/down flavors plus a strange quark, and the Wilson twisted mass regularization for quarks in the valence, with up/down, strange and charm quarks. When tuning the twisted mass quarks at maximal twist, systematic effects of order $\mathcal{O}(a)$ arising from the discretization of space-time are expected to cancel, improving the scaling of physical observables towards the continuum. This is pertinent to the study of charm physics, given that the discretization effects associated with the charm quark are of order $\mathcal{O}(am_c)$ and large due to the heavy mass of the charm quark m_c. Consequently, our mixed action is expected to significantly aid in the extraction of precise charm observables with a controlled continuum limit.

The utilization of this mixed action breaks unitarity of the theory, even in the continuum, due to the use of different lattice regularizations for the sea and valence sectors. In order to account for this effect, it is necessary to ensure that the physical quark masses in both sectors are matched. Since the sea contains only up/down and strange quarks, it is necessary to adjust the parameters of the mixed action in order to impose that the valence up/down and strange physical quark masses are identical to those in the sea. This requires precise calculations in the light and strange sectors of QCD, which is the focus of this thesis.

In conjunction to this, in Lattice Field Theory every physical quantity is computed in units of the lattice spacing a. Consequently, in order

to make predictions, one must first find the value of a in physical units in order to convert any prediction on the lattice to physical units. This task is called scale setting, and it is the main focus of this thesis. As calculations in Lattice Field Theory have become increasingly precise in recent years, entering the "precision era" with uncertainties falling below 1%, setting the scale with high accuracy has become a primary focus of the community. This is because the determination of the scale affects any prediction of the theory. For example, the determination of the anomalous magnetic moment of the muon with subpercent accuracy requires setting the scale with a precision of a few permil [22].

The thesis is structured as follows. In Chapter 1 we introduce the QCD action in the continuum and its gauge structure. We then consider how it can be formulated in a lattice with finite lattice spacing a. We elucidate the methodology for computing expectation values numerically, thereby bridging the gap between the path integral formalism in the Euclidean and statistical mechanics. We explain the procedure for taking the continuum limit and its relation to renormalizability. We review the Symanzik improvement program, which has the objective of reducing the discretization systematic effects and assisting in the task of taking the continuum limit. Furthermore, we elucidate the scale setting program. In Chapter 2 we define all the relevant physical observables that we will require in this thesis and how they are extracted on the lattice. We also explain how to extract the ground state signals of these observables, isolating them from excited states, using model variation techniques. In Chapter 3 we introduce our mixed action regularization. We explain the differences between the sea and valence sectors, and perform the matching between them to impose equal physical quark masses in both sectors. Simultaneously we tune the valence to maximal twist in order to obtain $\mathcal{O}(a)$ improvement. Furthermore, we introduce the line of constant physics followed and the mass shifting procedure needed to correct for small mistunings along it. In Chapter 4 we perform the scale setting of our mixed action by computing the gradient flow scale t_0 in physical units, using as external physical input the decay constants of the pion and kaon. We explore a number of different models to perform the chiral extrapolation to the physical pion mass and the continuum limit at vanishing lattice spacing $a \to 0$. We use model averaging techniques to compute a final average result of t_0 in physical units, taking into account the systematic uncertainty due to the model variation. Treating t_0 as an intermediate scale allows to extract the lattice spacing in fermi (fm). In Chapter 5 we stress the impact of our scale setting procedure in the computation of hadronic computations involving the charm quark: using our determination of the scale t_0 we find results for the renormalized charm quark mass and $f_{D_{(s)}}$ decay constants in

our mixed action setup, following our work in [34]. Finally, we present our conclusions in Section iv.

This thesis is accompanied by a number of appendices. In Appendix A we present some conventions regarding the Gamma matrices, quark bilinears and the twisted and physical basis used in the different lattice regularizations. In Appendix B we give the expressions for the Gell-Mann matrices and the $su(3)$ structure constants. In Appendix C we review the gauge ensembles used in this work. We quote results for the relevant lattice observables computed in these ensembles in Appendix D. In Appendix E we review some useful simulation details of Lattice Field Theories. In Appendix F we give details on the error propagation and treatment of (auto)correlations. In Appendix G we briefly discuss how the Dirac operator needed to compute n-point functions is inverted on the lattice. In Appendix H we give details on the fitting strategy we follow throughout this work. In Appendix J we give expressions for the correction of finite volume effects as given by Chiral Perturbation Theory. Finally, in Appendix K we summarize all the results for t_0 in physical units in the continuum and physical pion mass for each model explored for the chiral-continuum extrapolation.

INTRODUCCIÓN

Blabla

Part II

FOUNDATIONS

QCD ON THE LATTICE

1.1 INTRODUCTION

The theory that describes the strong interaction between quarks and gluons is called Quantum Chromodynamics or QCD.

The underlying symmetry of QCD is associated with the non-abelian $SU(N = 3)$ Lie group. The elements of this group are non-commuting, traceless unitary matrices Ω with unit determinant $\det \Omega = 1$. In order to have a gauge theory we must allow these elements to depend on space-time coordinates. The map

$$\Omega(x) = e^{i\alpha^{(a)}(x)T^{(a)}}, \tag{1.1}$$

provides a local parameterization of the group near the identity with coordinates $\alpha^{(a)}(x)$. Summation over $a = 1, ..., N^2 - 1 = 8$ is implicit and $T^{(a)}$ are the 8 generators of the $SU(3)$ Lie group. These live in the Lie algebra $su(3)$, which is the tangent space of the group $SU(3)$ at the identity $I \in SU(3)$. They satisfy the commutation relations

$$\left[T^{(a)}, T^{(b)}\right] = i f_{abc} T^{(c)}, \tag{1.2}$$

where f_{abc} are the structure constants of the group, given in Appendix B. Unitarity of the group elements means that

$$\Omega^\dagger \Omega = 1. \tag{1.3}$$

The group elements Ω must be in some representation which determines how they act on a vector space where the degrees of freedom of the theory live. In QCD these are quarks and gluons. The former are described by spinor fields $\psi_{\alpha,i}, \bar{\psi}_{\alpha,i}$. They carry a Dirac spinor index $\alpha = 1, 2, 3, 4$ and a flavor index $i = 1, ..., N_f$, to each flavor corresponding a different mass (in Nature $N_f = 6$). They transform under SU(3) in the fundamental representation,

$$\psi(x) \to \Omega(x)\psi(x), \quad \bar{\psi}(x) \to \bar{\psi}(x)\Omega(x)^\dagger. \tag{1.4}$$

In this representation the group generators $T^{(a)}$ are given by the Gell-Mann matrices (see Appendix B), and quark fields live in a 3-dimensional vector space, having an additional index $c = 1, 2, 3$ called color. As spinor fields, their dynamics is governed by the Dirac action, which in Euclidean metric $g_{\mu\nu} = \text{diag}(+1, +1, +1, +1)$ reads

$$S_F = \sum_{i=1}^{N_f} \int d^4x \, \bar{\psi}^i(x) \left(\gamma_\mu \partial_\mu + m_i\right) \psi^i(x). \tag{1.5}$$

Here we have implicitly summed over the repeated μ index and omitted the spinor and color indices. This action is invariant under global $SU(3)$ transformations (Ω independent of x). In order to promote this to a local or gauge symmetry, we must replace the derivative by a covariant one

$$\partial_\mu \psi(x) \rightarrow D_\mu \psi(x) = \partial_\mu \psi(x) + i A_\mu(x) \psi(x), \tag{1.6}$$

with A_μ a new gauge field which must transform under $SU(3)$ in the adjoint representation

$$A_\mu(x) \rightarrow \Omega(x) A_\mu(x) \Omega^\dagger(x) + i \Omega(x) \partial_\mu \Omega^\dagger(x), \tag{1.7}$$

in order to ensure gauge invariance of the Dirac action. This field A_μ lives in the $su(3)$ algebra, and thus it is a hermitian, traceless matrix which can be decomposed as a linear combination of the algebra generators $T^{(a)}$

$$A_\mu = A_\mu^{(a)} T^{(a)}, \tag{1.8}$$

where we again implicitly sum over the repeated index a. The gauge or gluon fields must have a kinetic piece in the action for them to be dynamical. This is given by the Yang-Mills action

$$\frac{1}{2g_0^2} \int d^4x \, \mathrm{tr}(F_{\mu\nu}(x) F_{\mu\nu}(x)), \tag{1.9}$$

which describes dynamical gauge fields in the absence of matter. The dimensionless parameter g_0 is the coupling constant and the energy strength tensor $F_{\mu\nu}$ is given by

$$F_{\mu\nu}(x) = \partial_\mu A_\nu(x) - \partial_\nu A_\mu(x) + i \left[A_\mu(x), A_\nu(x) \right]. \tag{1.10}$$

Again, this object lives in the $su(3)$ algebra and can be expressed as

$$F_{\mu\nu} = F_{\mu\nu}^{(a)} T^{(a)}. \tag{1.11}$$

From the transformation in eq. (1.7) we derive the transformation relations of $F_{\mu\nu}$

$$F_{\mu\nu}(x) \rightarrow \Omega(x) F_{\mu\nu}(x) \Omega^\dagger(x). \tag{1.12}$$

Finally, the QCD action in continuum space-time is given by

$$S_{\mathrm{QCD}} = \sum_{i=1}^{N_f} \int d^4x \, \bar{\psi}^i(x) \left(\gamma_\mu D_\mu + m_i \right) \psi^i(x) \tag{1.13}$$

$$+ \frac{1}{2g_0^2} \int d^4x \, \mathrm{tr} \left(F_{\mu\nu}(x) F_{\mu\nu}(x) \right). \tag{1.14}$$

The only parameters of this action are the quark masses m_i and the dimensionless coupling constant g_0.

As mentioned in the Introduction, QCD is strongly coupled at low energies or large distances. Consequently, one cannot rely on perturbation theory to compute physical observables, as an expansion on powers of the coupling does not converge. The only known first-principles method other than perturbation theory to perform theoretical predictions in Quantum Field Theory is Lattice Quantum Field Theory, Lattice QCD when applied to the study of Quantum Chromodynamics. This method is based on the discretization of space-time into a hypercubic box or lattice

$$\Lambda = \{n_0, n_1, n_2, n_3 | n_0 = 0, ..., T/a - 1; n_i = 0, ..., L/a - 1; i = 1, 2, 3\},$$

$$(1.15)$$

where a is the lattice spacing between two adjacent sites, and L, T are the spatial and temporal lattice extents (in physical units) respectively. The discretization of space-time and the introduction of a finite lattice spacing a provide a natural energy cutoff for momenta $\sim a^{-1}$, removing UV divergences. On the other hand, the finite volume lattice ensures the absence of IR divergences. This implies that the lattice formulation can be seen as a way to regularize any particular Quantum Field Theory. However, this also implies the presence of finite volume and discretization effects, which should be removed from any prediction. To do this, after computing some physical observable on the lattice setup, one must perform a continuum extrapolation to obtain results at $a \to 0$ and simulate large enough volumes in order to be able to neglect the effects associated with finite volume. If the theory is renormalizable, physical quantities will remain finite in the continuum limit.

After discretizing space-time, fields are placed at the lattice sites $n \in \Lambda$. Fermion fields are represented by

$$\psi(n), \bar{\psi}(n), \quad n \in \Lambda. \tag{1.16}$$

For the gauge fields, it will be helpful to use the definition of a parallel transporter for $SU(N)$. An N-component unit vector v is parallel transported along a curve in space-time parameterized by $z_\mu(t)$ from point $z_\mu(a) = x$ to $z_\mu(b) = y$ as

$$v(b) = P(y, x)v(a), \tag{1.17}$$

$$P(y, x) = \mathcal{P}e^{i \int_x^y A_\mu(z) dz_\mu}, \tag{1.18}$$

with A_μ the $SU(N)$ gauge field. This implies that a fermion in the fundamental representation acquires a phase factor of $P(y, x)$ when going from x to y. This parallel transporter is referred to as a gauge link and its discrete version will be used for the gauge degrees of freedom on the lattice. It is an element of the group and transforms as

$$P(x, y) \to \Omega(x) P(x, y) \Omega^\dagger(y). \tag{1.19}$$

Once the fields on the lattice have been defined, the next step is to discretize the QCD action. This is done by formulating it in a finite box Λ in terms of the aforementioned fields in such a way that in the continuum limit $a \to 0$ the continuum QCD action is recovered. We discuss this in the following sections.

The Chapter is organized as follows. In Sec. 1.2 we present the Wilson formulation of the gauge action on the lattice, expressed in terms of the link variables. In Sec. 1.3 we present various methods for discretizing the fermion action. In Sec. 1.3.1 we discuss the issue of fermion doublers that arise with a naive fermion discretization and its connection to the formulation of chiral symmetry on the lattice. We also provide some brief comments on Ginsparg-Wilson fermions. In Sec. 1.3.2 we present the solution to the doublers problem proposed by Wilson, which consists in adding a term that explicitly breaks chiral symmetry. This term gives an additional mass to the doublers that grows with the inverse of the lattice spacing a, which helps to distinguish them. In Sec. 1.3.3 we discuss a modification of Wilson fermions which adds a chirally rotated mass term. This regularization offers several advantages that will be crucial for our study. In Sec. 1.4 we review some of the fundamental concepts of the path integral formalism and how expectation values are computed numerically on the lattice. In Sec. 1.5 we review some concepts of renormalizability and the continuum limit on the lattice. In Sec. 1.6 we discuss the Symanzik improvement program, which allows to reduce cutoff effects associated with the lattice action and fields, thus facilitating the task of performing the continuum limit. Finally, in Sec. 1.7 the procedure for setting the scale on the lattice is discussed. This is necessary in order to extract lattice predictions in physical units.

1.2 PURE GAUGE SU(3) ON THE LATTICE

on the lattice, gluon fields can be defined by the link variables $U_\mu(x) \in SU(3)$ that act as a discrete version of the gauge transporters connecting points x and $x + \hat{\mu}$, with $\hat{\mu} = \{a\hat{x}_0, a\hat{x}_1, a\hat{x}_2, a\hat{x}_3\}$

$$U_\mu(x) = \exp\left(iaA_\mu(x)\right). \tag{1.20}$$

These fields transform as

$$U_\mu(x) \to \Omega(x)U_\mu(x)\Omega^\dagger(x + \hat{\mu}), \tag{1.21}$$

and they live on the links of the lattice that connect sites x and $x + \hat{\mu}$.

A common discretization of the gluonic action is the Wilson gauge action [129], which is expressed in terms of the link variables $U_\mu(x)$

$$S_G = \frac{1}{g_0^2} \sum_x \sum_{\mu,\nu} \mathrm{Re} \ \mathrm{tr}\left(1 - U_{\mu\nu}(x)\right), \tag{1.22}$$

where $U_{\mu\nu}(x)$ is the plaquette centered on the lattice site x

$$U_{\mu\nu}(x) = U_\mu(x)U_\nu(x+\hat\mu)U_\mu^\dagger(x+\hat\nu)U_\nu^\dagger(x), \tag{1.23}$$

and we have used

$$U_\mu^\dagger(x) = U_{-\mu}(x+\hat\mu). \tag{1.24}$$

Using the Baker-Campbell-Hausdorff formula iteratively

$$\exp(A)\exp(B) = \exp\left(A + B + \frac{1}{2}[A,B] + ...\right), \tag{1.25}$$

and using eq. (1.20) we get

$$S_G = a^4\frac{\beta}{6}\sum_x\sum_{\mu,\nu}\mathrm{tr}\left(F_{\mu\nu}^2(x)\right) + \mathcal{O}(a^2), \tag{1.26}$$

where we introduced the inverse coupling

$$\beta = \frac{6}{g_0^2}. \tag{1.27}$$

Taking the continuum limit $a^4\sum_x \to \int d^4x$ we recover the continuum Yang-Mills action.

Eq. (1.26) shows that the effects associated with the discretization of space-time are of order $\mathcal{O}(a^2)$ for the Wilson gauge action. The discretization of the SU(3) pure Yang-Mills action is not unique, and different choices result in different cutoff effects.

The $\mathcal{O}(a^2)$ cutoff effects present in the Wilson regularization of the gauge action can be further reduced by adding additional terms that respect the symmetries of the theory following the Symanzik improvement program. One such choice is the Lüscher-Weisz action [85], which we discuss in Sec. 1.6.

1.3 INTRODUCING FERMIONS ON THE LATTICE

After discretizing the SU(3) gauge action, we still need to find a suitable discrete version of the fermion action in eq. (1.13) to fully formulate QCD on the lattice. It will be shown that theoretical challenges arise with the naive fermion discretization and how these can be addressed with alternative formulations.

1.3.1 *Naive fermions*

To discretize the continuum fermion action in the absence of gauge fields, considering only one flavor with mass m,

$$S_F = \int d^4x\bar\psi(x)\left(\gamma_\mu\partial_\mu + m\right)\psi(x), \tag{1.28}$$

the derivative ∂_μ needs to take a discrete form, which can be done easily by

$$\partial_\mu \psi(x) \rightarrow \hat{\partial}_\mu \psi(x) = \frac{1}{2a}\left(\psi(x+\hat{\mu}) - \psi(x-\hat{\mu})\right). \tag{1.29}$$

To respect gauge symmetry in our action, we must promote the derivative $\hat{\partial}_\mu$ to a covariant one, as in the continuum case. To achieve this, we note that terms like

$$\bar{\psi}(x)\psi(x+\hat{\mu}), \tag{1.30}$$

which arise from $\bar{\psi}(x)\hat{\partial}_\mu \psi(x)$ are not gauge invariant

$$\bar{\psi}(x)\psi(x+\hat{\mu}) \rightarrow \bar{\psi}(x)\Omega^\dagger(x)\Omega(x+\hat{\mu})\psi(x+\hat{\mu}). \tag{1.31}$$

The solution is to introduce the link variable or parallel transporter $U_\mu(x)$ from site x to $x+\hat{\mu}$ defined in eq. (1.20) which transforms as in eq. (1.21). This way, the discretized fermion action reads

$$S_F = a^4 \sum_x \bar{\psi}(x)\left(\gamma_\mu \frac{U_\mu(x)\psi(x+\hat{\mu}) - U_\mu^\dagger(x-\hat{\mu})\psi(x-\hat{\mu})}{2a} + m\psi(x)\right). \tag{1.32}$$

However, this naive formulation of the fermion action exhibits the problem of doubling: despite the fact that we wrote our action to describe one fermion of mass m, for finite lattice spacing a additional poles with the same ground state energy appear, spoiling the dynamics of the theory. These unwanted additional poles are known as doublers. To see how they appear, we consider the massive Dirac operator $D(x,y)$ in the continuum, defined such that

$$S_F = \int d^4x \, d^4y \, \bar{\psi}(x)D(x,y)\psi(y). \tag{1.33}$$

on the lattice this takes the form

$$S_F = a^4 \sum_{n,m} \bar{\psi}(n)D(n,m)\psi(m), \tag{1.34}$$

with the Dirac operator for the naive fermion formulation given by

$$D(n,m) = \gamma_\mu \frac{U_\mu(n)\delta_{n+\hat{\mu},m} - U_\mu^\dagger(n-\hat{\mu})\delta_{n-\hat{\mu},m}}{2a} + m\delta_{n,m}. \tag{1.35}$$

Restricting to the free massless fermion case $U_\mu = 1$ for illustration, upon Fourier transform we get

$$\tilde{D}(p,q) = \frac{1}{V}\sum_{n,m} e^{-ip\times na}D(n,m)e^{iq\times ma} \tag{1.36}$$

$$= \frac{1}{V}\sum_{n,m} e^{-i(p-q)na}\left(\gamma_\mu \frac{e^{iq_\mu a} - e^{-iq_\mu a}}{2a}\right) \tag{1.37}$$

$$= \delta(p-q)\tilde{D}(p), \tag{1.38}$$

with V the 4-dimensional volume of the lattice and

$$\tilde{D}(p) = \sum_\mu \frac{i}{a} \gamma_\mu \sin(p_\mu a), \tag{1.39}$$

where we made explicit again the sum over μ. The inverse of this operator can be computed as

$$\tilde{D}^{-1}(p) = \frac{ia^{-1} \sum_\mu \gamma_\mu sin(p_\mu a)}{a^{-2} \sum_\mu sin(p_\mu a)^2}. \tag{1.40}$$

We can see that in the continuum $a \to 0$ we recover the correct form of the Dirac operator

$$\tilde{D}(p)^{-1}|_{m=0} \to_{a \to 0} \frac{-i\gamma_\mu p_\mu}{p^2} \tag{1.41}$$

with one single pole at $p^2 = 0$. However, at finite lattice spacing, the denominator in eq. (1.40) vanishes not only for $p = (0, 0, 0, 0)$ but also for

$$p = (\pi/a, 0, 0, 0),\ (0, \pi/a, 0, 0),\ ...,\ (\pi/a, \pi/a, \pi/a, \pi/a). \tag{1.42}$$

These are 15 unwanted poles, the doublers, that only disappear in the continuum, once they become infinitely heavy. These doublers have the same ground energy as the true pole at $p^2 = 0$ and they affect the dynamics of the theory.

The problem of doublers is related to chiral symmetry and its implementation on the lattice. Chiral symmetry in continuum QCD can be expressed as

$$\{D, \gamma_5\} = 0, \tag{1.43}$$

with D the Dirac operator. Th Nielsen-Ninomiya [110, 111] Theorem states that one cannot implement chiral symmetry in the way of eq. (1.43) on the lattice without the appearance of doublers. In this lattice formulation of chiral symmetry, there must be an equal number of right movers and left movers. In particular, this means having just one pole is not possible. Ginsparg and Wilson [65] proposed a suitable version of chiral symmetry for the lattice as

$$\{D, \gamma_5\} = aD\gamma_5 D, \tag{1.44}$$

such that in the continuum eq. (1.43) is recovered. With this definition of chiral symmetry on the lattice, it is possible to construct Dirac operators that satisfy eq. (1.44) and are free of doublers.

If one is not interested in studying physics related to chiral symmetry, another choice is to build a Dirac operator that explicitly breaks chiral symmetry but removes the doublers. Wilson fermions and Wilson twisted mass fermions are examples of such a choice, which we will now study.

1.3.2 *Wilson fermions*

Wilson proposed [129] adding an extra term to the naive fermion action in eq. (1.32) to distinguish the doublers from the true pole. The Wilson fermion action reads

$$S_{\mathrm{W}} = a^4 \sum_x \bar{\psi}(x) \frac{1}{2} \left(\gamma_\mu \left(\nabla_\mu + \nabla_\mu^* \right) + 2m - a \nabla_\mu \nabla_\mu^* \right) \psi(x), \quad (1.45)$$

where we have defined the forward and backward discrete covariant derivatives as

$$\nabla_\mu \psi(x) = \frac{U_\mu(x)\psi(x + \hat{\mu}) - \psi(x)}{a}, \quad (1.46)$$

$$\nabla_\mu^* \psi(x) = \frac{\psi(x) - U_\mu^\dagger(x - \hat{\mu})\psi(x - \hat{\mu})}{a}. \quad (1.47)$$

From the Wilson fermion action (1.45) the Wilson Dirac operator reads

$$D = D_{\mathrm{W}} + m = \frac{1}{2} \left(\gamma_\mu \left(\nabla_\mu + \nabla_\mu^* \right) - a \nabla_\mu \nabla_\mu^* \right) + m, \quad (1.48)$$

where we have introduced the massless Wilson Dirac operator D_{W}, and the action can be written as

$$S_{\mathrm{W}} = a^4 \sum_x \bar{\psi}(x) \left(D_{\mathrm{W}} + m \right) \psi(x). \quad (1.49)$$

For N_f flavors, an additional sum over a flavor index $i = 1, ..., N_f$ is required, and m is promoted to a diagonal matrix in flavor space, whose diagonal elements are m_i. The fermion mass m_i is commonly expressed in terms of the κ parameter

$$\kappa_i = \frac{1}{2am_i + 8}. \quad (1.50)$$

For the free case, the momentum space massless Dirac operator reads

$$\tilde{D}_{\mathrm{W}}(p) = \frac{i}{a} \sum_\mu \gamma_\mu \sin(p_\mu a) + \frac{1}{a} \sum_\mu \left(1 - \cos(p_\mu a) \right). \quad (1.51)$$

The second summand in the right-hand side comes from the Wilson extra term $a \nabla_\mu \nabla_\mu^*$ in the action, and it is responsible for giving an additional mass term to the doublers

$$\frac{2l}{a}, \quad (1.52)$$

where l is the number of momentum components with $p_\mu = \pi/a$ for the doubler. This additional mass distinguishes the doublers from the true pole and makes them decouple as we approach the continuum limit.

The Wilson term $a\nabla_\mu \nabla_\mu^*$ in the Wilson Dirac operator manifestly breaks chiral symmetry, even in the $m_i = 0$ limit, and this symmetry is only restored in the continuum limit. Consequently, the quark mass receives additive renormalization contributions,

$$m_i^R = Z_m \left(m_i - m_{\mathrm{cr}} \right), \tag{1.53}$$

since it is no longer protected against them by the axial symmetry.

The Wilson fermion action has $\mathcal{O}(a)$ cutoff effects, which can be systematically reduced by using the Symanzik improvement program detailed in Sec. 1.6.

1.3.3 Wilson twisted mass fermions

Wilson twisted mass (tm) fermions [58–61, 120] introduce an imaginary mass term to the Wilson Dirac operator in eq. (1.48) of the form

$$i\bar{\psi}(x)\boldsymbol{\mu}\gamma_5\psi(x), \tag{1.54}$$

with $\boldsymbol{\mu}$ the twisted quark mass matrix in flavor space. More generally, the Wilson tm Dirac operator reads

$$D = D_W + \boldsymbol{m} + i\boldsymbol{\mu}\gamma_5. \tag{1.55}$$

Our case of interest for this thesis will be

$$\boldsymbol{\mu} = \mathrm{diag}\left(\mu_u, -\mu_d, -\mu_s, \mu_c \right), \tag{1.56}$$

$$\boldsymbol{m} = \mathrm{diag}\left(m_u, m_d, m_s, m_c \right). \tag{1.57}$$

By rotating the fields

$$\psi \;\rightarrow\; \psi' = e^{-i\frac{\pi}{2}\gamma_5\frac{T}{2}}\psi, \quad \bar{\psi} \;\rightarrow\; \bar{\psi}' = \bar{\psi}e^{-i\frac{\pi}{2}\gamma_5\frac{T}{2}}, \tag{1.58}$$

$$T = \mathrm{diag}(\eta_u, \eta_d, \eta_s, \eta_c), \tag{1.59}$$

with $\alpha_i \equiv \frac{\pi}{2}\eta_i$ the so called twist angles, defined with the renormalized standard and twisted quark masses as

$$\cot \alpha_i = \frac{m_i^R}{\mu_i^R}, \tag{1.60}$$

one retrieves the usual physical (standard) formulation with real fermionic mass

$$M_i^2 = m_i^2 + \mu_i^2, \tag{1.61}$$

and a chirally rotated Wilson term. The rotated fields $\psi', \bar{\psi}'$ define the so called physical basis, while the unrotated ones $\psi, \bar{\psi}$ define the twisted basis.

In practice we will be working with Wilson tm fermions at maximal twist

$$\eta_u = \eta_c = -\eta_s = -\eta_d = 1, \tag{1.62}$$

which can be obtained by setting the renormalized standard masses m_i^R to zero. The procedure to achieve this is explained in Sec. 3.5.

Considering for simplicity the light sector of mass-degenerate up-/down (u and d) quarks, at maximal twist the symmetry group $SU(2)_V \times SU(2)_A$ is broken into

$$SU(2)_V \times SU(2)_A \rightarrow [U(1)_A]_1 \times [U(1)_A]_2 \times [U(1)_V]_3, \quad (1.63)$$

with

$$[U(1)_A]_a = \begin{cases} \psi(x) \rightarrow e^{i\alpha_A^a \gamma_5 \frac{\tau^a}{2}} \psi(x) & a = 1,2 \\ \bar{\psi}(x) \rightarrow \bar{\psi}(x) e^{i\alpha_A^a \gamma_5 \frac{\tau^a}{2}} & a = 1,2 \end{cases}, \quad (1.64)$$

and

$$[U(1)_V]_3 = \begin{cases} \psi(x) \rightarrow e^{i\alpha_A^3 \frac{\tau^3}{2}} \psi(x) \\ \bar{\psi}(x) \rightarrow \bar{\psi}(x) e^{-i\alpha_A^3 \frac{\tau^3}{2}} \end{cases}, \quad (1.65)$$

with τ^a the Pauli matrices. This means that at maximal twist axial symmetries are not completely broken, and thus the twisted mass is protected against additive renormalization,

$$\mu_i^R = Z_\mu(g_0^2, a\mu)\mu_i. \quad (1.66)$$

An important role in our setup is played by the Ward-Takahashi identities (WTI). They will be used to tune the Wilson twisted mass parameters to ensure maximal twist. Furthermore, they allow to identify the renormalization constant of the twisted masses Z_μ. For the non-singlet case ($i \neq j$) the WTI for the axial and vector currents, in the continuum limit and in the twisted basis, read (see eqs. (2.1-2.2) for the definition of the currents)

$$\partial_\mu V_\mu^{ij} = (m_i - m_j)S^{ij} + i(\eta_i \mu_i - \eta_j \mu_j)P^{ij}, \quad (1.67)$$

$$\partial_\mu A_\mu^{ij} = (m_i + m_j)P^{ij} + i(\eta_i \mu_i + \eta_j \mu_j)S^{ij}. \quad (1.68)$$

Note that at zero twist angle $\eta_u = \eta_d = \eta_s = \eta_c = 0$ the twisted and physical basis are the same, and the standard WTIs are recovered. However, at maximal twist the renormalized standard masses m_i^R vanish, which in turn means that the current masses m_i in eqs. (1.67-1.68) also vanish (up to cutoff effects). Moreover, the exact flavor symmetry of massless Wilson fermions implies the existence of a point-split vector current $\tilde{V}_\mu^{ij}$ on the lattice such that the vector WTI holds exactly on the lattice. In the twisted basis, this current takes the form

$$\tilde{V}_\mu^{ij} = \frac{1}{2}\left[\bar{\psi}^i(x)(\gamma_\mu - 1)U_\mu(x)\psi^j(x+\hat{\mu}) + \bar{\psi}^i(x+\hat{\mu})(\gamma_\mu + 1)U_\mu^\dagger(x)\psi^j(x) \right].$$

$$(1.69)$$

The conservation of this WTI on the lattice for $\tilde{V}_\mu^{ij}$ means that the point-split vector current renormalizes trivially with

$$Z_{\tilde{V}} = 1. \tag{1.70}$$

Looking at eq. (1.67) this means that for all flavors

$$Z_\mu = Z_P^{-1}. \tag{1.71}$$

1.4 PATH INTEGRAL REGULARIZATION

Having formulated the QCD action on the lattice, we need to see how physical quantities are computed. To do so, we review some aspects of the path integral formulation in Euclidean space-time. In this formalism, physical quantities are expressed as expectation values of operators

$$\langle O(x_1, ..., x_n) \rangle = \frac{1}{\mathcal{Z}} \int \mathcal{D}[\psi, \bar{\psi}, U] O(x_1, ..., x_n) e^{-S[\psi, \bar{\psi}, U]}, \tag{1.72}$$

$$\mathcal{Z} = \int \mathcal{D}[\psi, \bar{\psi}, U] e^{-S[\psi, \bar{\psi}, U]}. \tag{1.73}$$

This is equivalent to expectation values in statistical mechanics with a Boltzmann factor of $e^{-S[\psi, \bar{\psi}, U]}$. The action can be decomposed into its gluon and fermion components $S[\psi, \bar{\psi}, U] = S_G[U] + S_F[\psi, \bar{\psi}, U]$, and fermion degrees of freedom can be integrated out as

$$\langle O(x_1, ..., x_n) \rangle = \frac{1}{\mathcal{Z}} \int \mathcal{D}[U] e^{-S_G[U]} \mathcal{Z}_F$$
$$\times \left[\frac{1}{\mathcal{Z}_F} \int \mathcal{D}[\psi, \bar{\psi}] O(x_1, ..., x_n) e^{-S_F[\psi, \bar{\psi}]} \right] \tag{1.74}$$
$$= \frac{1}{\mathcal{Z}} \int \mathcal{D}[U] e^{-S_G[U]} \mathcal{Z}_F \langle O(x_1, ..., x_n) \rangle_F, \tag{1.75}$$

with

$$\mathcal{Z}_F = \int \mathcal{D}[\psi, \bar{\psi}] e^{-S_F[\psi, \bar{\psi}]} = \Pi_{i=1}^{N_f} \det(D). \tag{1.76}$$

This fermionic determinant can be expressed as an effective action as

$$\langle O(x_1, ..., x_n) \rangle = \frac{1}{\mathcal{Z}} \int \mathcal{D}[U] e^{-S_G[U] - S_{\text{eff}}[U]} \langle O(x_1, ..., x_n) \rangle_F, \tag{1.77}$$

$$\mathcal{Z} = \int \mathcal{D}[U] e^{-S_G[U] - S_{\text{eff}}[U]}, \tag{1.78}$$

$$S_{\text{eff}}[U] = -\sum_{i=1}^{N_f} \log \det(D). \tag{1.79}$$

In order to compute meson observables we will use meson interpolators, which are composite fermionic observables that share the

same quantum numbers as the desired meson state. A generic meson interpolator has the form

$$O_A^{ij}(x) = \bar{\psi}^i(x)\Gamma_A\psi^j(x),\tag{1.80}$$

with Γ_A a Gamma matrix or product of matrices. This way, a meson two-point function reads

$$\begin{aligned}\left\langle O_A^{ij}(x_1)O_B^{ji}(x_2)\right\rangle &= \frac{1}{\mathcal{Z}}\int \mathcal{D}[U]e^{-S_G[U]-S_{\text{eff}}[U]}\\ &\quad\times\left\langle \bar{\psi}^i(x_1)\Gamma_A\psi^j(x_1)\psi^i(x_2)\Gamma_B\bar{\psi}^j(x_2)\right\rangle_{\text{F}}\tag{1.81}\\ &= -\frac{1}{\mathcal{Z}}\int \mathcal{D}[U]e^{-S_G[U]-S_{\text{eff}}[U]}\\ &\quad\times\operatorname{tr}\left(\Gamma_A D_i^{-1}(x_1,x_2)\Gamma_B D_j^{-1}(x_2,x_1)\right),\tag{1.82}\end{aligned}$$

where the trace is over spin indices and D_i the massive Dirac operator for flavor i. In order to perform this integral numerically, using the connection with statistical mechanics, a finite set of N_{cnfg} gauge configurations is generated with Boltzmann distribution $e^{-S_G[U]-S_{\text{eff}}[U]}$ following a Markov process (see Appendices E, F). Then, measurements of the quantity

$$P = -\operatorname{tr}\left(\Gamma D_i^{-1}(x_1,x_2)\Gamma D_j^{-1}(x_2,x_1)\right),\tag{1.83}$$

are taken in each of these configurations, and the expectation value is computed as

$$\langle P\rangle = \frac{1}{N_{\text{cnfg}}}\sum_i^{N_{\text{cnfg}}} P_i + \mathcal{O}\left(\frac{1}{\sqrt{N_{\text{cnfg}}}}\right).\tag{1.84}$$

1.5   CONTINUUM LIMIT

For the discussion in this subsection we follow [73]. The lattice regularization provides with a natural energy cutoff a^{-1}, ensuring that any loop integral is finite in perturbation theory. In perturbative renormalization, it is necessary to take the cutoff to infinity, which on the lattice means taking the lattice spacing to $a \to 0$. If the theory is renormalizable, any physical quantity (e.g. a mass m_{phys}) in units of the lattice spacing must vanish in the continuum limit

$$m_{\text{phys}}a \to 0,\tag{1.85}$$

since this means that m_{phys} remains finite in this limit.

Physical quantities are dependent on the couplings of the theory, $m_{\text{phys}}(g_0)$, and accordingly change with them. In turn, one can study

how the couplings of the theory change on the lattice as one approaches the continuum limit by decreasing a. To do so and for simplicity, we assume a single coupling g_0, and write the most general local effective action at lattice spacing a_1

$$S(a_1) = g_0(a_1) \sum_i O_i, \tag{1.86}$$

where O_i are all possible local operators respecting the lattice symmetries. At a finer lattice spacing $a_2 < a_1$ all the short-range extra degrees of freedom can be integrated out and reabsorbed into a redefinition of the coupling, obtaining an effective action at the original scale a_1, $S^{(2)}(a_1)$, that has the same generic form but with different couplings

$$S^{(2)}(a_1) = g_0^{(2)}(a_1) \sum_i O_i, \tag{1.87}$$

$$g_0^{(2)}(a_1) = R(g_0(a_1)). \tag{1.88}$$

R here stands for the renormalization group (RG) transformation that defines the change in the couplings when varying the lattice spacing. It can be observed then that renormalizability corresponds to fixed points g_0^* of the RG transformation

$$R(g_0^*) = g_0^*. \tag{1.89}$$

In the context of $SU(N)$ Yang-Mills theory, perturbation theory shows that at a fixed value of the renormalized coupling g_R the bare coupling runs with the lattice spacing as

$$a \frac{\partial g_0}{\partial a} \equiv \beta(g_0) = -\beta_0 g_0^3 - \beta_1 g_0^5 + ..., \tag{1.90}$$

where $\beta_{0,1}$ are universal coefficients (do not depend on the renormalization scheme) and positive for $N = 3$ colors and $N_f = 6$ flavors, as in the case of QCD. This shows that $g_0 = 0$ is a fixed point of the RG transformations and thus corresponds to the continuum limit. As the fixed point is in the weak coupling regime, this perturbative argument is expected to be valid. Therefore, the continuum limit corresponds to

$$g_0 \to 0, \tag{1.91}$$

or in terms of the inverse coupling β

$$\beta \to \infty. \tag{1.92}$$

In practice, one cannot numerically simulate at infinite inverse coupling β. Therefore, physical observables are computed at several finite values of β. This introduces $\mathcal{O}(a^n)$ cutoff effects in the results, with some power n. To obtain results in the continuum, one parameterizes these cutoff effects with some function of the lattice spacing and extrapolates to $a \to 0$. However, this task is far from trivial, and it has

been shown that spectral quantities receive logarithmic corrections on the lattice spacing [77] which could significantly complicate this task. To help in the continuum limit extrapolation, one can systematically reduce lattice artifacts, e.g. from $\mathcal{O}(a)$ to $\mathcal{O}(a^2)$ following the Symanzik improvement program.

1.6 SYMANZIK IMPROVEMENT PROGRAM

Symanzik improvement requires improving both the action of the theory and the lattice interpolators that enter the different correlators.

In order to improve a lattice action, one can describe the target continuum theory in terms of an effective action in powers of the lattice spacing a

$$S_{\text{eff}} = \int d^4 x \sum_k c_k \mathcal{L}_k(x) a^{k-4}. \tag{1.93}$$

Here $\mathcal{L}_0(x)$ is the discretized lattice Lagrangian unimproved, the higher-dimension terms $\mathcal{L}_k(x)$ are all possible Lagrangians built from fermion and gluon field operators that preserve the symmetries of the regularized theory, i.e. the lattice theory, with mass dimension $4 + k$, and c_k are numerical coefficients.

In the case of Lattice QCD, we saw that in the Wilson gauge action in eq. (1.26) lattice artifacts appear at $\mathcal{O}(a^2)$, and therefore no $\mathcal{O}(a)$ improvement is required. However, these $\mathcal{O}(a^2)$ effects can be further reduced by adding all possible dimension $4 + k = 6$ operators that preserve the underlying symmetries of the gauge action. These dimension-6 operators are all three possible ways of writing a closed path in a rectangular lattice with 6 gauge links: planar, twisted and L-shaped rectangles. The action then reads

$$S_G = \frac{\beta}{3} \sum_{\mu\nu} \left[c_0 \sum_p \text{Re} \left(\text{tr} \left(1 - U_{\mu\nu}(p) \right) \right) + \sum_{i=1}^{3} c_i \sum_r \text{Re} \left(\text{tr} \left(1 - U^{(i)}(r) \right) \right) \right], \tag{1.94}$$

with $U^{(i)}$ said dimension-6 operators. Tuning the coefficients c_i properly leads to $\mathcal{O}(a^2)$ improvement. The CLS ensembles that we employ in this thesis (see Sec. 3.2) use the so called Lüscher-Weisz gauge action [84, 85], with these coefficients computed at tree-level

$$c_0 = \frac{5}{3}, \quad c_1 = -\frac{1}{12}, \quad c_2 = c_3 = 0. \tag{1.95}$$

Thus, in the Lüscher-Weisz gauge action the only dimension-6 operators that survive are planar rectangles $U^{(1)}$.

We also need to improve the fermion action. Wilson fermions have $\mathcal{O}(a)$ cutoff effects. In order to improve the Wilson fermion action

to $\mathcal{O}(a^2)$ we need to look for all possible operators with dimension $4 + k = 5$ that preserve the lattice symmetries. These are

$$\mathcal{L}_{k=1}^{(1)} = i\bar{\psi}(x)\sigma_{\mu\nu}\hat{F}_{\mu\nu}(x)\psi(x), \tag{1.96}$$

$$\mathcal{L}_{k=1}^{(2)} = m\text{tr}\left(\hat{F}_{\mu\nu}(x)\hat{F}_{\mu\nu}(x)\right), \tag{1.97}$$

$$\mathcal{L}_{k=1}^{(3)} = m^2\bar{\psi}(x)\psi(x), \tag{1.98}$$

with

$$\sigma_{\mu\nu} = \frac{[\gamma_\mu, \gamma_\nu]}{2i}, \tag{1.99}$$

$$\hat{F}_{\mu\nu}(x) = \frac{-i}{8a^2}\left(Q_{\mu\nu}(x) - Q_{\nu\mu}(x)\right), \tag{1.100}$$

$$Q_{\mu\nu} = U_{\mu\nu}(x) + U_{\nu,-\mu}(x) + U_{-\mu,-\nu}(x) + U_{-\nu,\mu}(x). \tag{1.101}$$

$\mathcal{L}_{k=1}^{(2),(3)}$ are already present (up to numerical factors) in the original Wilson fermion action and can therefore be reabsorbed in those terms. The $\mathcal{O}(a)$ improved Wilson Dirac operator appearing in the improved fermion action reads

$$D_{\text{W}} + m + c_{\text{sw}}a\frac{1}{2}\sum_{\mu<\nu}\sigma_{\mu\nu}\hat{F}_{\mu\nu}, \tag{1.102}$$

with c_{sw} the Sheikholeslami-Wohlert coefficient determined non perturbatively in [119].

Improving the lattice action ensures improvement of on-shell quantities such as meson masses. However, if one is interested in matrix elements mediated by some current $\mathcal{J}_\mu$, it is also necessary to improve the lattice interpolators that enter into the definition of those currents. In analogy with the improvement of the action, a local operator O is expressed in the Symanzik effective theory as

$$O_{\text{eff}}(x) = \sum_k c_k O_k(x)a^k. \tag{1.103}$$

Again, O_k are gauge invariant local operators with the right mass dimensions and c_k some parameter properly tuned to cancel a^k cutoff effects. Following this, a generic n-point function reads

$$\langle\Phi\rangle = \langle\Phi_0\rangle - a\int d^4y\,\langle\Phi_0\mathcal{L}_1(y)\rangle + a\,\langle\Phi_1\rangle + ..., \tag{1.104}$$

with

$$\langle\Phi_0\rangle = \langle O_0(x_1)...O_0(x_n)\rangle, \tag{1.105}$$

$$\langle\Phi_1\rangle = \sum_{i=1}^{n}\langle O_0(x_1)...O_1(x_i)...O_0(x_n)\rangle, \tag{1.106}$$

and vacuum expectation values taken in the continuum. In Sec 2 we discuss the details of operator improvement for the observables of interest.

The $\mathcal{O}(a)$ improved Wilson tm fermion action is analogous to the Wilson case, with the improved Dirac operator given by

$$D_{\mathrm{W}} + m + i\gamma_5\mu + c_{\mathrm{sw}}a\frac{1}{2}\sum_{\mu<\nu}\sigma_{\mu\nu}\hat{F}_{\mu\nu}. \tag{1.107}$$

The advantage of Wilson tm fermions is that at maximal twist (vanishing renormalized standard quark mass) one achieves automatic $\mathcal{O}(a)$ improvement [58, 120]. This means that physical quantities are automatically improved without the need of any improvement coefficients for lattice operators. The following argument is based on the original work [58] to which we refer for a complete proof.

At maximal twist, the Wilson tm Dirac operator reads

$$D_{\mathrm{W}} + i\mu\gamma_5. \tag{1.108}$$

Working in the twisted basis, this action in the continuum is invariant under a discrete chiral symmetry

$$\mathcal{R}_5^{1,2} = \begin{cases} \psi(x) \to i\gamma_5\tau^{1,2}\psi(x) \\ \bar{\psi}(x) \to \bar{\psi}(x)i\gamma_5\tau^{1,2} \end{cases}, \tag{1.109}$$

while $\mathcal{L}_{k=1}^{(1)}$ in eq. (1.96) is not

$$\mathcal{L}_{k=1}^{(1)} \to -\mathcal{L}_{k=1}^{(1)}. \tag{1.110}$$

This is key for automatic $\mathcal{O}(a)$ improvement. For correlation functions like eq. (1.104), we have that operators may be even or odd under $\mathcal{R}_5$, $\langle\Phi_0\rangle$ and $\langle\Phi_1\rangle$ having opposite $\mathcal{R}_5$-chirality

$$\langle\Phi_0\rangle \to \pm\langle\Phi_0\rangle, \quad \langle\Phi_1\rangle \to \mp\langle\Phi_1\rangle. \tag{1.111}$$

This means that for even $\langle\Phi_0\rangle$

$$\langle\Phi_0\rangle = \langle\Phi_0\rangle, \quad \left\langle\Phi_0\mathcal{L}_{k=1}^{(1)}\right\rangle = -\left\langle\Phi_0\mathcal{L}_{k=1}^{(1)}\right\rangle = 0, \tag{1.112}$$

$$\langle\Phi_1\rangle = -\langle\Phi_1\rangle = 0, \tag{1.113}$$

and thus even operators are automatically $\mathcal{O}(a)$ improved. On the other hand, for odd operators what we have is

$$\langle\Phi_0\rangle = -\langle\Phi_0\rangle = 0, \quad \left\langle\Phi_0\mathcal{L}_{k=1}^{(1)}\right\rangle = \left\langle\Phi_0\mathcal{L}_{k=1}^{(1)}\right\rangle, \tag{1.114}$$

$$\langle\Phi_1\rangle = \langle\Phi_1\rangle, \tag{1.115}$$

and thus they vanish in the continuum. Summing up, the only tuning required for Wilson tm fermions to achieve $\mathcal{O}(a)$ improvement is to set the bare quark mass m to its critical value m_{cr} in order to obtain maximal twist.

In our particular case, we will be working with a mixed action setup employing standard Wilson quarks in the sea and fully twisted Wilson

tm quarks in the valence (see Sec 3). This means valence observables still get residual $\mathcal{O}(a)$ cutoff effects from the sea sector, and thus improvement is still needed. However, these effects are expected to be $\mathcal{O}(g_0^4)$ in perturbation theory.

Finally, we also need to improve the bare gauge coupling, which at $\mathcal{O}(a)$ reads

$$\tilde{g}_0^2 = g_0^2 \left(1 + a b_g \text{tr} \left(M_q^{(\text{s})} \right) \right), \tag{1.116}$$

with $M_q^{(\text{s})}$ the sea quark mass matrix (see Sec. 3), and b_g the improvement coefficient, whose value at one-loop is given in [91].

1.7 SCALE SETTING

on the lattice, all physical observables are computed in units of the lattice spacing a. Consequently, in order to make any prediction, it is necessary to determine a in physical units. This task is called scale setting. It involves the precise determination of a reference observable, called the scale, in physical units, to which any other observable is compared to in order to extract the value of the latter in physical units. As mentioned in the introduction, in "precision era" lattice calculations, high precision scale setting is of the utmost importance in order to extract predictions whose uncertainty is not dominated by the scale.

As an example of the scale setting procedure, we could use the proton mass m_{proton} as a reference scale, and calculate the ratio of it to a given mass m_i

$$R_i = \frac{m_i}{m_{\text{proton}}}. \tag{1.117}$$

After computing the continuum limit of R_i, we can extract the physical mass m_i as

$$m_i^{\text{ph}} = R_i(a = 0) \times m_{\text{proton}}^{\text{exp}}. \tag{1.118}$$

Here, the proton mass is used as a reference scale, and comparing any lattice observable to it allows to extract the latter in physical units, once the continuum limit is performed. This procedure is equivalent to finding the value of the lattice spacing in physical units, since it can be extracted as

$$a = \frac{(a m_{\text{proton}})^{\text{latt}}}{m_{\text{proton}}^{\text{exp}}}. \tag{1.119}$$

From eq. (1.118) it is clear that when aiming for precise lattice calculations of any physical observable like m_i, a reliable and precise scale setting is of the utmost importance. In this example this means being able to determine m_{proton} with high accuracy on the lattice in order

to compute the ratios R_i, controlling the continuum limit of R_i and having a high precision determination of $m_{\text{proton}}^{\text{exp}}$.

In this context, baryon masses like the proton or the Ω baryon mass are popular choices to set the scale [10]. The former is determined with high accuracy experimentally [133] but suffers from the signal-to-noise problem [82, 86] on the lattice determination. This problem is also present in the Ω baryon mass, but the statistical precision is better there [10]. Furthermore, the Ω baryon mass has a weak dependence on the light quark masses and a strong one in the strange quark mass. This makes it an interesting scale for trajectories with constant strange quark mass. Another choice is using meson masses. The pion and kaon meson masses are used to define the line of constant physics along which the continuum limit is taken, and therefore are not available to set the scale. In the past, the ρ meson mass was used to set the scale of quenched simulations [20, 78, 98], but it is not suited for dynamical quarks simulations. The Y meson mass is also used [55, 68] thanks to its precise experimental determination. However, large discretization effects due to the b quark are expected.

Instead of using a phenomenological scale like the ones listed above, another choice is to use intermediate scales, like the gradient flow scale t_0 [87, 94] this thesis is based on and that we introduce in Sec. 2.6. This quantity is a popular choice [10, 13, 29, 76, 81, 123] since it can be computed to a very high precision on the lattice, though it is not a physical quantity and as such cannot be measured experimentally. To obtain its value in the continuum and physical quark masses, one builds a dimensionless quantity $(\sqrt{t_0}\Lambda)^{\text{latt}}$ with some phenomenological quantity Λ on the lattice. After performing the continuum limit, the physical value of t_0 can be extracted as

$$\sqrt{t_0^{\text{ph}}} = \frac{\left(\sqrt{t_0}\Lambda\right)^{\text{latt}}\Big|_{a=0}}{\Lambda^{\text{exp}}}. \tag{1.120}$$

In addition to the continuum limit, on the lattice often unphysical quark masses are simulated since they are computationally cheaper. This means one needs to perform chiral extrapolations/interpolations of lattice observables to reach physical quark masses. Both chiral and continuum limits are discussed in Sec. 4 for the scale setting we perform in this thesis.

Once the physical value of t_0 is found, it can be used as an intermediate scale against which any other quantity Λ' on the lattice can be compared in order to extract the latter in physical units. For this purpose, one performs a continuum extrapolation of $\sqrt{t_0}\Lambda'$ and obtains the physical value of Λ' as

$$\Lambda'^{\text{ph}} = \frac{\left(\sqrt{t_0}\Lambda'\right)^{\text{latt}}\Big|_{a=0}}{\sqrt{t_0^{\text{ph}}}}. \tag{1.121}$$

This quantity is already a prediction of the lattice.

A popular choice [23, 27, 29, 123] for Λ in eq. (1.120) and the one used in this work is a linear combination of the pion and kaon decay constants. These exhibit large plateaux on the lattice, indicating that excited states contributions decay fast and therefore they can be determined to a high precision on the lattice. On the other hand, their experimental values are extracted from the weak processes $\pi/K \to l\nu$, which leads to the measurement of $V_{ud(us)}f_{\pi(K)}$, with $V_{ud,us}$ CKM matrix elements. This leads to an increase in the uncertainty of the experimental values of $f_{\pi,K}$ coming from the determination of said CKM matrix elements [5].

Finally, other popular intermediate scales to t_0 are ω_0 [13, 23, 81] which is closely related to t_0, and the force scale r_0 [16, 107, 121] which is derived from the static quark-antiquark potential extracted from the evaluation of Wilson loops. This potential shows early plateaux [122] which again indicates that excited states contributions are small.

ON THE EXTRACTION OF PHYSICAL OBSERVABLES

2.1 INTRODUCTION

In this Chapter we discuss the technical details on the extraction of physical observables from the lattice. In Sec. 2.2 we define the two-point functions required for extracting the physical observables needed in the analysis of the scale setting. In Sec. 2.3 we discuss how to extract meson masses while Sec. 2.4 covers the extraction of decay constants, their improvement and renormalization. In Sec. 2.5 we define the PCAC quark masses which will be used to tune Wilson tm quarks at maximal twist. In Sec. 2.6 we discuss the gradient flow scale t_0 which we will use as the reference scale for the scale setting. Finally, in Sec. 2.7 we discuss the model averaging technology which we employ in order to find the ground state signals from all these lattice observables.

2.2 CORRELATION FUNCTIONS

For the extraction of the physical observables of interest for this work we need two-point functions involving the pseudoscalar and axial currents, defined as

$$P^{ij}(x) = \bar{\psi}^i(x)\gamma_5\psi^j(x), \tag{2.1}$$

$$A_\mu^{ij}(x) = \bar{\psi}^i(x)\gamma_\mu\gamma_5\psi^j(x), \tag{2.2}$$

where i, j are flavor indices. The Wilson term in the Wilson and Wilson tm fermion action breaks chiral symmetry explicitly, and as a result the Noether currents of the theory are no longer protected against renormalization. This means that both the pseudoscalar and axial currents get renormalized as

$$P^{ij,R} = Z_P(g_0^2, a\mu) \left(1 + a\tilde{b}_P m_{ij} + a\bar{b}_P \text{tr}\left(M_q\right)\right) P^{ij}, \tag{2.3}$$

$$A_\mu^{ij,R} = Z_A(g_0^2) \left(1 + a\tilde{b}_A m_{ij} + a\bar{b}_A \text{tr}\left(M_q\right)\right) A_\mu^{ij}, \tag{2.4}$$

where the b-counterterms are improvement coefficients for the renormalization constants. The renormalization constants are shown in Table 2.1, while the improvement coefficients are in Table 2.2. For our purposes, we will only need the differences $\tilde{b}_A - \tilde{b}_P$, $\bar{b}_A - \bar{b}_P$ and $\tilde{b}_A$, the latter given in perturbation theory by [125]

$$\tilde{b}_A = 1 + 0.0472 g_0^2 + \mathcal{O}(g_0^4). \tag{2.5}$$

β	Z_A	Z_P
3.40	0.75642(72)	0.35121(56)
3.46	0.76169(93)	0.34941(44)
3.55	0.76979(43)	0.34767(55)
3.70	0.78378(47)	0.34732(63)
3.85	0.79667(47)	0.35014(73)

Table 2.1: Renormalization constants Z_A and Z_P for different values of β. Z_A, which does not depend on the energy scale but only on the bare coupling g_0^2, is calculated non-perturbatively in [49] using the chirally rotated Schrödinger functional. Z_P is calculated non-perturbatively at the scale $\mu_{\text{had}} = 233(8)$ MeV in [35].

β	$\tilde{b}_A - \tilde{b}_P$	$\bar{b}_A - \bar{b}_P$	$\tilde{b}_A$
3.40	-0.324(17)	$\mathcal{O}(g_0^4)$	1.2684
3.46	-0.265(14)	$\mathcal{O}(g_0^4)$	1.2638
3.55	-0.196(14)	$\mathcal{O}(g_0^4)$	1.2571
3.70	-0.119(14)	$\mathcal{O}(g_0^4)$	1.2467
3.85	-0.073(12)	$\mathcal{O}(g_0^4)$	1.2371

Table 2.2: Summary of improvement coefficients at CLS β values. $\tilde{b}_A - \tilde{b}_P$ is taken from LCP-1 results in [53], while $\bar{b}_A - \bar{b}_P$ are computed in perturbation theory. $\tilde{b}_A$ is computed in perturbation theory in [125] and given by eq. (2.5)

To achieve $\mathcal{O}(a)$ improvement in the Wilson regularization, we need to improve the axial current as part of the Symanzik improvement program as follows

$$A_\mu^{ij}(x) \rightarrow A_\mu^{ij}(x) + a c_A \tilde{\partial}_{x_0} P^{ij}(x), \tag{2.6}$$

where we defined the symmetric discrete time derivative

$$\tilde{\partial}_{x_0} = \frac{\hat{\partial}_{x_0} - \hat{\partial}_{x_0}^*}{2}, \tag{2.7}$$

$$\hat{\partial}_x f(x) = \frac{f(x+a) - f(x)}{a}, \tag{2.8}$$

$$\hat{\partial}_x^* f(x) = \frac{f(x) - f(x-a)}{a}. \tag{2.9}$$

The improvement coefficient c_A is given non-perturbatively by [32]

$$c_A(g_0^2) = -0.006033 g_0^2 \left[1 + \exp\left(9.2056 - \frac{13.9847}{g_0^2} \right) \right]. \tag{2.10}$$

The two-point functions that we will focus on, projected to zero-momentum are given by

$$C_P^{ij}(x_0, y_0) = \frac{a^6}{L^3} \sum_{\vec{x}, \vec{y}} \left\langle P^{ij}(x) P^{ji}(y) \right\rangle,$$ (2.11)

$$C_A^{ij}(x_0, y_0) = \frac{a^6}{L^3} \sum_{\vec{x}, \vec{y}} \left\langle A_0^{ij}(x) P^{ji}(y) \right\rangle.$$ (2.12)

When only light and strange flavors are involved, the measurements of the two-point functions (see Appendix G) are taken at fixed source times y_0, $T - y_0$, with $y_0 = a$, and evaluated at all sink times x_0. In order to increase statistics the average

$$C_X(x_0, y_0) \rightarrow \frac{C_X(x_0, y_0) \pm C_X(T - x_0, T - y_0)}{2},$$ (2.13)

is taken, with the $+$ sign for the $X = P$ case and $-$ sign for the $X = A$ case. On the other hand, when heavy flavors are involved (see Sec. 5), the source position is fixed at $y_0 = T/2$ in order to maximise the distance from the boundaries: when dealing with heavy-light and heavy-heavy flavor contents in the correlators, we observe that the region in which the signal for the considered two-point function is accessible lies entirely within the lattice bulk, and that the boundary effects are strongly suppressed[1].

The spectral decomposition of the two-point functions C_X allows to extract relevant hadronic observables such as the meson masses and decay constants. In what follows we restrict to the case of the pion, but the same applies to any other flavor content. Using the Transfer Matrix formalism and imposing as boundary conditions that the initial and final states are given by

$$|\phi(0, \vec{x})\rangle = |\phi_i\rangle, \quad |\phi(T, \vec{x})\rangle = |\phi_f\rangle,$$ (2.14)

we can express a generic two-point function by

$$\langle O(x) O(y) \rangle = \mathcal{Z}^{-1} \left\langle \phi_f \middle| e^{-(T-x_0)\hat{H}} \hat{O}(\vec{x}) e^{-(x_0-y_0)\hat{H}} \hat{O}(\vec{y}) e^{-y_0 \hat{H}} \middle| \phi_i \right\rangle,$$ (2.15)

$$\mathcal{Z} = \left\langle \phi_f \middle| e^{-T\hat{H}} \middle| \phi_i \right\rangle.$$ (2.16)

Inserting a complete set of states $|\vec{p}, n\rangle$

$$1 = \frac{1}{2E_n(\vec{p})L^3} \sum_{\vec{p}, n} |\vec{p}, n\rangle \langle \vec{p}, n|,$$ (2.17)

---

1 The numerical inversion of the quark propagator in the charm region is performed using distance preconditioning techniques [42, 52] in order to reduce signal deterioration and enhance accuracy at large Euclidean times.

this becomes

$$\langle O(x)O(y)\rangle = \mathcal{Z}^{-1}\frac{1}{L^9}\sum_{n,m,l}\sum_{\vec{p},\vec{q},\vec{s}}\frac{1}{2^3 E_n(\vec{p})E_m(\vec{q})E_l(\vec{s})}$$
$$\times\langle\phi_f|\vec{q},m\rangle\,e^{-(T-x_0)E_m(\vec{q})}$$
$$\times\langle\vec{q},m|\,\hat{O}(\vec{x})\,|\vec{p},n\rangle\,e^{-(x_0-y_0)E_n(\vec{p})}$$
$$\times\langle\vec{p},n|\,\hat{O}(\vec{y})\,|\vec{s},l\rangle\,e^{-y_0 E_s(\vec{l})}\,\langle\vec{s},l|\phi_i\rangle. \tag{2.18}$$

The partition function reads

$$\mathcal{Z} = \langle\phi_f|\,e^{-T\hat{H}}\,|\phi_i\rangle = \frac{1}{L^3}\sum_{\vec{p},n}\frac{1}{2E_n(\vec{p})}\,\langle\phi_f|\vec{p},n\rangle\,e^{-TE_n(\vec{p})}\,\langle\vec{p},n|\phi_i\rangle$$
$$\rightarrow\langle\phi_f|0\rangle\,e^{-TE_0}\,\langle 0|\phi_i\rangle, \tag{2.19}$$

with the notation

$$|0\rangle\langle 0| \equiv \frac{1}{2E_0 L^3}\,\big|\vec{0},0\big\rangle\big\langle\vec{0},0\big|. \tag{2.20}$$

We assume that the boundary states $|\phi_{i,f}\rangle$ are the same and denoted by $|\Omega\rangle$, and share the same quantum numbers of the vacuum $|0\rangle$. This is true when using open boundary conditions (OBC) in time, which will be the case for most of the ensembles under study (see Table C.1).

We will label the quantum states as $\big|\vec{0},\alpha,n\big\rangle$, with n labeling the energy level and α the other quantum numbers, and using the fact that we are projecting to zero momentum $\vec{p}=\vec{0}$ we employ the shorthand notation

$$|\alpha,n\rangle\langle\alpha,n| \equiv \frac{1}{2E_n^\alpha L^3}\,\big|\vec{0},\alpha,n\big\rangle\big\langle\vec{0},\alpha,n\big|. \tag{2.21}$$

With all this, the two-point function can be written as

$$\langle O(x)O(y)\rangle = \sum_{\alpha,\beta,\gamma}\sum_{n,m,l}\frac{\langle\Omega|\beta,m\rangle}{\langle\Omega|0,0\rangle}e^{-(T-x_0)E_m^\beta}$$
$$\times\langle\beta,m|\,\hat{O}(\vec{x})\,|\alpha,n\rangle\,e^{-(x_0-y_0)E_n^\alpha}$$
$$\times\langle\alpha,n|\,\hat{O}(\vec{y})\,|\gamma,l\rangle\,e^{-y_0 E_s^\gamma}\frac{\langle\gamma,l|\Omega\rangle}{\langle 0,0|\Omega\rangle}, \tag{2.22}$$

where we absorbed the e^{-TE_0} term coming from the partition function into the energy levels

$$E_n^\alpha \rightarrow E_n^\alpha - E_0, \tag{2.23}$$

such that $E_0^0 = 0$.

For sufficiently large source-sink separation $x_0 - y_0 \rightarrow \infty$, only the pion state $|\pi,0\rangle$ propagates between $O(x)$ and $O(y)$. On the other

hand, we made the assumption that the boundary states only overlap with the vacuum, so we are left with

$$\langle O(x)O(y)\rangle = \sum_{m,l} \frac{\langle \Omega|0,m\rangle}{\langle \Omega|0,0\rangle} e^{-(T-x_0)E_m^0} \langle 0,m| \hat{O}(\vec{x}) |\pi,0\rangle$$

$$\times e^{-(x_0-y_0)m_\pi} \langle \pi,0| \hat{O}(\vec{y}) |0,l\rangle e^{-y_0 E_l^0} \frac{\langle 0,l|\Omega\rangle}{\langle 0,0|\Omega\rangle}. \quad (2.24)$$

Finally, far away from the boundaries $T - x_0, y_0 \to \infty$ the first relevant contribution from them is the one with energy E_1^0

$$\langle O(x)O(y)\rangle = \langle 0,0| \hat{O}(\vec{x}) |\pi,0\rangle e^{-(x_0-y_0)m_\pi} \langle \pi,0| \hat{O}(\vec{y}) |0,0\rangle$$

$$\times \left[1 + \eta_x e^{-(T-x_0)E_1^0} + \eta_y e^{-y_0 E_1^0} + ... \right], \quad (2.25)$$

with

$$\eta_x = \frac{\langle \Omega|0,1\rangle \langle 0,1| O(x) |\pi,0\rangle}{\langle \Omega|0,0\rangle \langle 0,0| O(x) |\pi,0\rangle}, \quad (2.26)$$

$$\eta_y = \frac{\langle \Omega|0,1\rangle \langle \pi,0| O(y) |0,1\rangle}{\langle \Omega|0,0\rangle \langle \pi,0| O(y) |0,0\rangle}. \quad (2.27)$$

So far we have assumed OBC in time. In the case with periodic boundary conditions (PBC), the pseudoscalar and axial correlators are periodic in time and identical (up to a relative minus sign for the axial) in x_0 and $T - x_0$. Considering the first excited state we can write them as

$$C_X(x_0, y_0) = a_X \left(e^{-m_\pi(x_0-y_0)} \pm e^{-m_\pi(T-x_0+y_0)} \right)$$

$$+ b_X \left(e^{-m'(x_0-y_0)} \pm e^{-m'(T-x_0+y_0)} \right), \quad (2.28)$$

where the $+$ sign corresponds to the pseudoscalar correlator $X = P$ and the $-$ sign for the axial $X = A$, $a_P = |\langle 0,0| P^{ud} |\pi,0\rangle|^2$ and $a_A = \langle 0,0| A_0^{ud} |\pi,0\rangle \langle 0,0| P^{ud} |\pi,0\rangle$, b_X the same matrix elements for the first excited state.

2.3 MESON MASSES

Meson masses involving the light and strange quarks can be extracted from the pseudoscalar two-point function $C_P(x_0, y_0)$ in eq. (2.11) with the effective mass, defined as

$$am_{\text{eff}}(x_0) = \log \left(\frac{C_P(x_0, y_0)}{C_P(x_0 + a, y_0)} \right). \quad (2.29)$$

For sufficiently large source-sink separation $x_0 \gg 1$ this effective mass $m_{\text{eff}}(x_0)$ tends to a plateau as can be seen from the spectral decomposition of the two-point function eq. (2.25).

In the case of PBC, to extract the pion mass one can alternatively build the quantity

$$\frac{C_P(x_0, y_0)}{C_P(x_0 + a, y_0)} = \frac{\cosh(am_\pi(x_0/a - y_0/a - T/2a))}{\cosh(am_\pi(x_0/a - y_0/a + a - T/2a))}, \quad (2.30)$$

and fit am_π.

The pion mass for one of the ensembles under study is shown in Fig. 2.1.

For the study of mesons involving heavy flavors (see Sec. 5), we will employ a generalised eigenvalue problem (GEVP) variational method, the details of which we give in Appendix I.

2.4 DECAY CONSTANTS

Meson decay constants are given by the vacuum-to-meson matrix elements. The matrix element we are interested in is the vacuum-to-pion mediated by the axial current

$$\langle 0, 0 | A_0^{ud} | \pi, 0 \rangle = f_\pi \sqrt{\frac{m_\pi}{2L^3}}, \quad (2.31)$$

where f_π is the bare pion decay constant. To extract this matrix element, we must remove the matrix element $\langle 0, 0 | P^{ud} | \pi, 0 \rangle$ from the axial two-point function $C_A(x_0, y_0)$ in eq. (2.11). To achieve this, when only light and strange flavors are involved, we compute the ratio

$$R(x_0) = \sqrt{\frac{|C_A(x_0, y_0) C_A(x_0, T - y_0)|}{C_P(x_0 = T - a, y_0)}}, \quad (2.32)$$

from which we extract the decay constant as

$$f_\pi(x_0) = \sqrt{\frac{2}{L^3 m_\pi}} R(x_0). \quad (2.33)$$

In the PBC case, in order to isolate the matrix element $\langle 0, 0 | A_0^{ud} | \pi, 0 \rangle$ we fit the axial and pseudoscalar correlators in eq. (2.28) to extract the fit parameters $a_{P,A}$. This allows to compute the decay constant as

$$f_\pi = \frac{2}{L^3 m_\pi} \frac{a_A}{\sqrt{a_P}}. \quad (2.34)$$

Following eq. (2.3), the pion decay constant in the Wilson regularization renormalizes as

$$f_\pi^R = Z_A(g_0^2) \left[1 + a\bar{b}_A \text{tr}\left(M_q\right) + a\tilde{b}_A m_{ud} \right] f_\pi. \quad (2.35)$$

We assumed improvement of the axial current according to eq. (2.6).

In the Wilson tm regularization at maximal twist, the chiral rotation in eq. (1.58) rotates the axial to the vector current when going from the physical to the twisted basis

$$A_\mu^{ij} \to i V_\mu^{ij}, \quad (2.36)$$

which allows to compute the decay constant from the vector current in the twisted basis following

$$\langle 0,0| V_0^{ud} |\pi,0\rangle = -if_\pi \sqrt{\frac{m_\pi}{2L^3}}. \tag{2.37}$$

The advantage of this is that the vector current is protected against renormalization (see eq. (1.70)) and thus so is f_π. Furthermore, in the twisted basis we can use the PCVC Ward-Takahashi identity in eq. (1.67)

$$\left\langle \left(\partial_0^* V_0^{ij}(x)\right) O^{ji}(y) \right\rangle = i \left(\eta_i \mu_i - \eta_j \mu_j\right) \left\langle P^{ij}(x)O^{ji}(y) \right\rangle, \tag{2.38}$$

where O is any interpolator chosen such that $\langle P^{ij}(x)O^{ji}(y)\rangle$ does not vanish and η_i are given by the maximal twist condition in eq. (1.62), in order to write the decay constant as

$$f_\pi = \sqrt{\frac{2L^3}{m_\pi^3}} \left(|\mu_u| + |\mu_d|\right) \left|\langle 0,0| P^{ud} |\pi,0\rangle\right|. \tag{2.39}$$

Different choices of the interpolator O will lead to different values of the decay constants due to cutoff effects. We choose to use the pseudoscalar density P^{ij} since it enhances the signal. To extract the matrix element $\langle 0,0| P^{ud} |\pi,0\rangle$, analogously to the Wilson case, when only light and strange flavors are involved we can estimate it by the plateau value of the ratio

$$R(x_0) = \sqrt{\frac{C_P(x_0, y_0)C_P(x_0, T - y_0)}{C_P(x_0 = T - a, y_0)}}. \tag{2.40}$$

For PBC, using again the PCVC relation, the decay constant reads

$$f_\pi = \sqrt{\frac{2L^3}{m_\pi^3}} \sqrt{a_P}. \tag{2.41}$$

Since working at maximal twist, no improvement is needed in the computation of eqs. (2.39-2.41).

The ratios defined in this section for the extraction of decay constants are shown for the case of one of the ensembles under study in Fig. 2.3.

In the case of meson decay constants involving heavy quarks (see Sec. 5), we employ again the GEVP method to extract the ground state signal of the relevant matrix elements (see Appendix I).

2.5 QUARK MASSES

For the quark masses we use the Partially Conserved Axial Current (PCAC) Ward-Takahashi identity

$$\left\langle \left(\partial_\mu A_\mu^{ij}(x)\right) O^{ji}(y) \right\rangle = 2m_{ij} \left\langle P^{ij}(x)O^{ji}(y) \right\rangle, \tag{2.42}$$

where O is any interpolator chosen such that $\langle P^{ij}(x)O^{ji}(y)\rangle$ does not vanish, and m_{ij} is the so called PCAC quark mass, where the flavor indices indicate combinations of the individual quark masses

$$m_{ij} = \frac{m_i + m_j}{2}. \tag{2.43}$$

The subtracted quark mass $m_i - m_{\text{cr}}$ must agree, up to cutoff effects, with the corresponding PCAC quark mass for flavor i after renormalization, so by using the latter we do not need to know a priori the additive mass renormalization. As in the decay constants case, we take $O^{ij} = P^{ij}$ since we find the signal to be enhanced. Thus, the PCAC quark masses read

$$m_{ij}(x_0) = \frac{\tilde{\partial}_{x_0} C_A^{ij}(x_0, y_0)}{2C_P(x_0, y_0)}. \tag{2.44}$$

As seen above, the axial current needs to be improved, and the numerator in eq. (2.44) becomes

$$\tilde{\partial}_{x_0} C_A^{ij}(x_0, y_0) + ac_A \hat{\partial}_{x_0} \hat{\partial}_{x_0}^* C_P^{ij}(x_0, y_0) \tag{2.45}$$

with the discrete second derivative given by

$$\hat{\partial}_x \hat{\partial}_x^* f(x) = \frac{f(x+a) + f(x-a) - 2f(x)}{a^2} + \mathcal{O}(a^2). \tag{2.46}$$

Finally, from eq. (2.3) we see that the PCAC quark mass renormalizes as

$$m_{ij}^{\text{R}} = \frac{Z_A}{Z_P} \left[1 + a \left(\bar{b}_A - \bar{b}_P \right) \text{tr} \left(M_q \right) + a \left(\tilde{b}_A - \tilde{b}_P \right) m_{ij} \right] m_{ij}. \tag{2.47}$$

In the Wilson regularization, physical quark masses are determined from the PCAC masses, while in the Wilson tm regularization at maximal twist, the latter vanish and the former are given by the renormalized twisted masses in eq. (1.66).

In Fig. 2.2 we show the dependence of the PCAC quark mass for one of the ensembles under study.

2.6   GRADIENT FLOW

For the scale setting, we will use the gradient flow scale t_0 as an intermediate scale. The gradient flow is defined by the partial differential equation [87, 94]

$$\frac{dB_\mu(x, t)}{dt} = D_\nu G_{\mu\nu}(x, t), \quad B_\mu(x, t = 0) = A_\mu(x), \tag{2.48}$$

with A_μ the usual algebra-valued gauge fields. In this equation t is a new fictitious dimension called flow time. The associated field strength tensor $G_{\mu\nu}$ is defined by

$$G_{\mu\nu}(x, t) = \partial_\mu B_\nu(x, t) - \partial_\nu B_\mu(x, t) + i \left[B_\mu(x, t), B_\nu(x, t) \right], \tag{2.49}$$

with the covariant derivative acting on it in the adjoint representation

$$D_\nu G_{\mu\nu} = \partial_\nu G_{\mu\nu} + i \left[B_\mu, G_{\mu\nu} \right].$$

(2.50)

The flow equation can be rewritten as

$$\frac{dB_\mu(x,t)}{dt} = \frac{\delta S_{\text{YM}}[B]}{\delta B_\mu(x,t)}, \quad B_\mu(x,t=0) = A_\mu(x),$$

(2.51)

with S_{YM} the continuum Yang-Mills action in eq. (1.9) in terms of the flow fields B_μ. From this we can see that the effect of integrating this equation of motion is to flow the gauge fields towards the local minima of the Yang-Mills action. By solving the flow equation to leading order in the bare coupling g_0

$$B_\mu(x,t) = \frac{g_0}{4\pi t^2} \int d^4y \, e^{-(x-y)^2/4t} A_\mu(y).$$

(2.52)

The flow field B_μ is thus smoothed over space-time with smearing radius $r_{\text{smear}} = 2\sigma = \sqrt{8t}$, σ being the variance of the distribution in eq. (2.52), $\sigma^2 = 2t$.

on the lattice, eq. (2.48) can be expressed as

$$a^2 \frac{dV_\mu(x,t)}{dt} = -g_0^2 \frac{\delta S_G[V]}{\delta V_\mu(x,t)} V_\mu(x,t),$$

(2.53)

$$V_\mu(x,t=0) = U_\mu(x),$$

(2.54)

with U_μ the gauge links in eq. (1.20) and S_G the Wilson gauge action in eq. (1.22).

After integrating the flow equation eq. (2.48), the action density at flow time t can be defined as

$$E(x,t) = \frac{1}{2} \text{tr} \left(G_{\mu\nu}(x,t) G_{\mu\nu}(x,t) \right).$$

(2.55)

on the lattice, this can be computed by

$$E(x,t) = \sum_{\mu,\nu} \text{Re tr} \left(1 - V_{\mu\nu}(x,t) \right),$$

(2.56)

which is just eq. (1.22) but with the plaquette $U_{\mu\nu}(x)$ of gauge links $U_\mu(x)$ replaced by the plaquette $V_{\mu\nu}(x,t)$ of flow fields $V_\mu(x,t)$. After averaging over the 4-dimensional volume

$$E(t) = \langle E(x,t) \rangle_x,$$

(2.57)

we are left with an average energy density that depends only on the flow time. This average is computed using the model averaging technique detailed in Sec. 2.7. The quantity $t^2 E(t)$ can be precisely calculated on the lattice, making it a suitable choice for setting the scale (see Sec. 4). To this end, the scale t_0 is defined as the flow time which satisfies

$$t^2 E(t)|_{t=t_0} \equiv 0.3.$$

(2.58)

It will be this gradient flow scale t_0 which we will use as an intermediate scale to convert lattice results to physical units. Fig. 2.4 shows the extraction of t_0/a^2 for one of the ensembles under study.

2.7 GROUND STATE SIGNALS AND MODEL AVERAGE

So far, we have expressed all physical observables under study as functions of the Euclidean time x_0. As discussed in Sec. 2.2, these quantities are affected by boundary effects and excited states. In order to extract the ground state contribution of each observable, it is necessary to go to large source-sink separations and ensure sufficient distance from the boundaries. However, it is not clear how to decide when these conditions are met, and on the lattice community there are different approaches to address this issue, see e.g. [10, 29, 123]. Our choice is to employ model averaging techniques as proposed in [62, 108, 109].

The idea is to investigate multiple fit functions and/or several fit ranges and assign an Information Criterion IC to each choice, which allows to compute a weight

$$W_i \propto \exp\left(-\frac{1}{2}\text{IC}_i\right), \tag{2.59}$$

for each choice i of the "model", which refers to a specific fit function and fit range. Then one can compute a weighted average for a fit parameter p that is common to all models as

$$\langle p \rangle_{\text{MA}} = \sum_i p_i W_i, \tag{2.60}$$

where p_i is the fit parameter result for model i, and add a systematic uncertainty related to the model variation as

$$\sigma_{\text{syst}}^2[p] = \langle p^2 \rangle_{\text{MA}} - \langle p \rangle_{\text{MA}}^2. \tag{2.61}$$

For fitting we use a least-squares method that seeks to minimize a χ^2 function by finding the best values of the fit parameters (for details see Appendix H). As proposed in [62] we use the Takeuchi's Information Criterion (TIC)

$$\text{TIC} = \chi^2 - 2\langle \chi^2 \rangle, \tag{2.62}$$

where $\langle \chi^2 \rangle$ is a measure of the expected value of the χ^2 [30]. This IC is well-behaved for cases where fully correlated fits cannot be performed (see Appendix H for details), which is our case when fitting observables along the Euclidean time direction. For a fully correlated fit, $\langle \chi^2 \rangle = \text{dof}$, and thus the TIC reduces to the proposal in [109]

$$\text{TIC} = \chi^2 + 2n_{\text{param}} + 2n_{\text{cut}}, \tag{2.63}$$

with n_{param} the number of parameters of the fit and n_{cut} the number of points left out of the fit. We see that this Information Criterion penalizes models with large number of parameters and big cuts in data, provided the minimization of the χ^2 succeeds.

In practice, for the extraction of the ground state signals of lattice observables, the data is fitted to a constant plus two exponential signals for the OBC ensembles

$$f(x_0) = A + Be^{-Cx_0} + De^{-E(T-x_0)}, \qquad (2.64)$$

or for PBC ensembles

$$f(x_0) = A + Be^{-Cx_0} + Be^{-C(T-x_0)}, \qquad (2.65)$$

and we investigate the effects of varying the fit range. The result for the fit parameter A corresponds to the ground state signal. An illustration of the method for the extraction of the ground state signal in the pion effective mass in Fig. 2.1 is shown in Fig. 2.5, where we selected only a subset of the fit ranges explored for visualization purposes.

This model averaging technique will also be used for the chiral and continuum extrapolations needed to set the scale, but there we will also consider the variation of the fit functions and not only cutting data (variation of the fit range), see Sec. 4.
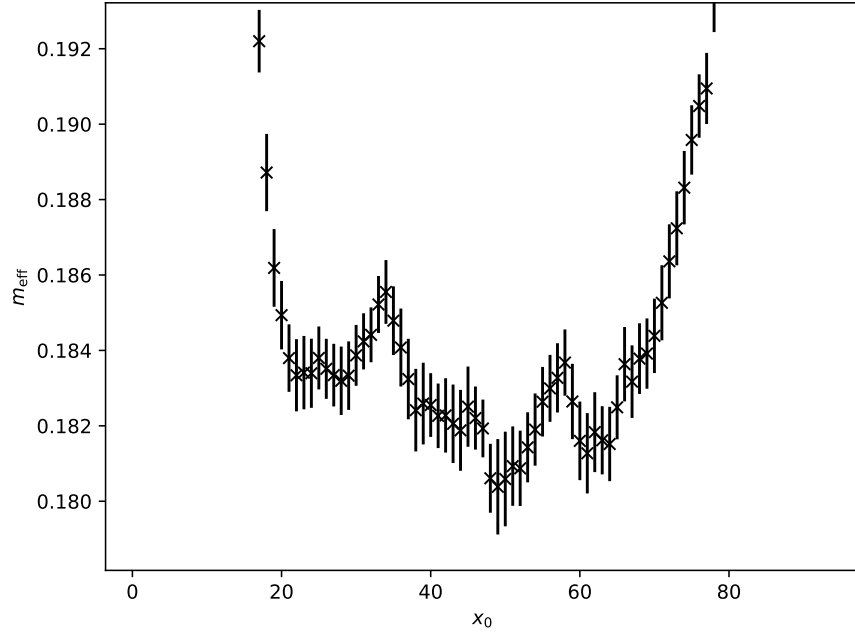
(a)
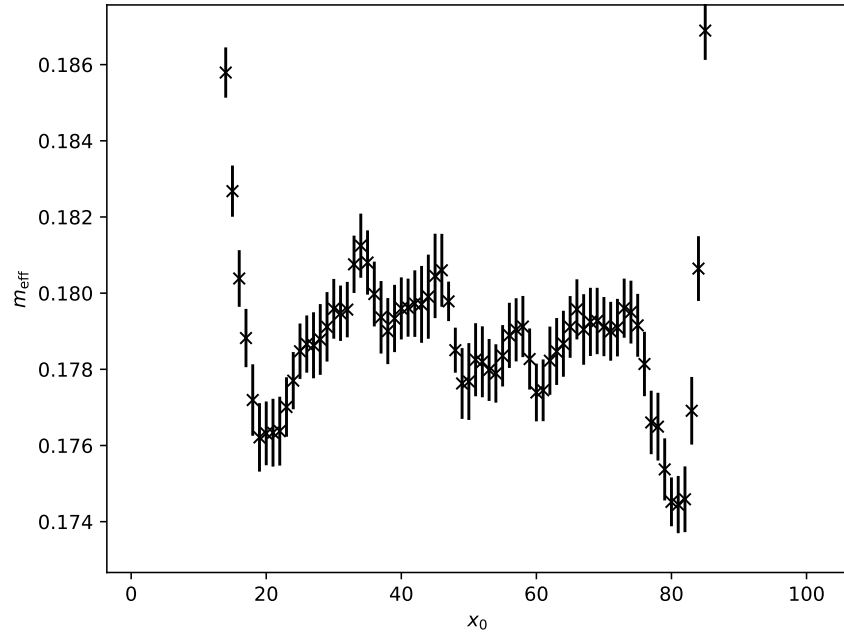
(b)

Figure 2.1: (a): pion effective mass m_{eff} in eq. (2.29) for ensemble H101 in the Wilson regularization. (b): the same but for the mixed action regularization for one point in our valence parameters grid, see Sec. 3.
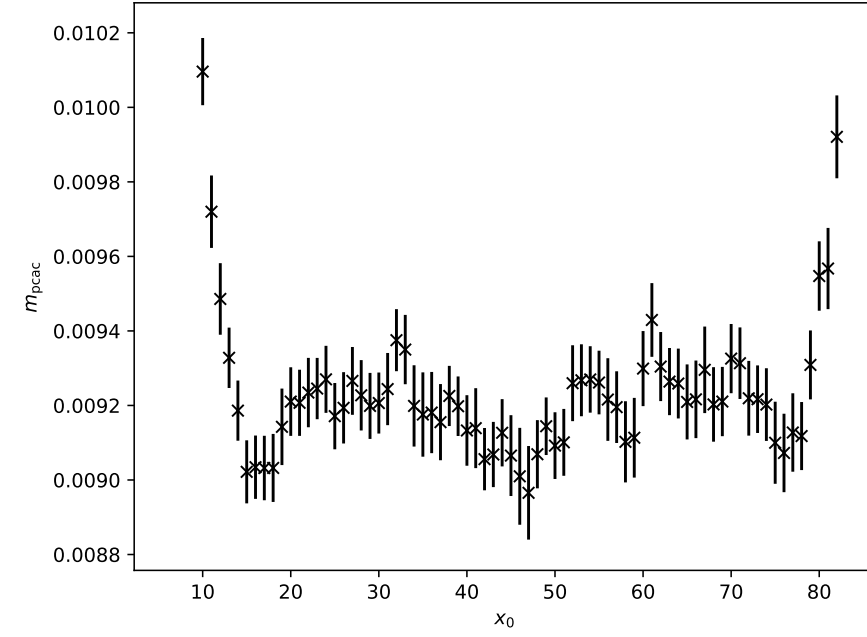
(a)
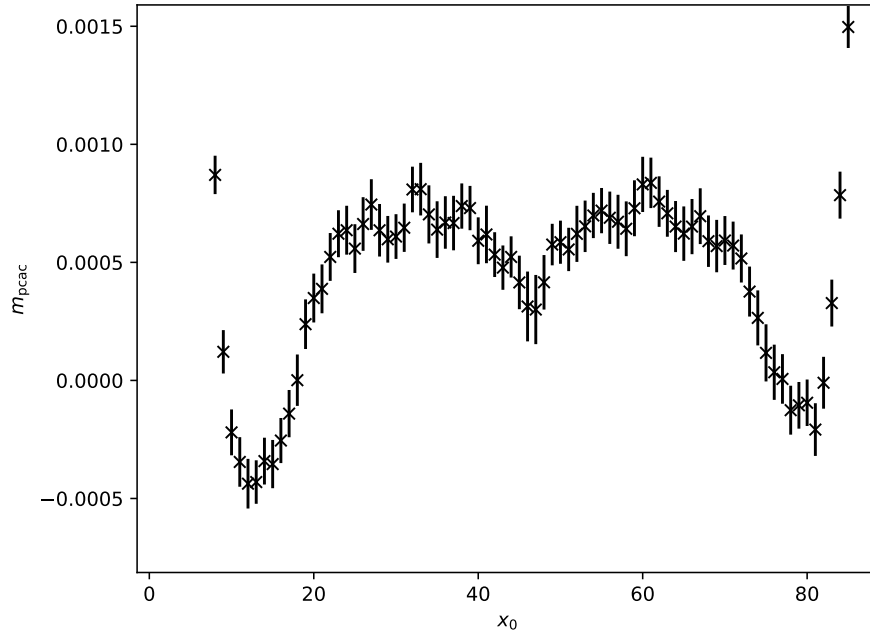
(b)

Figure 2.2: (a): up/down PCAC quark mass in eq. (2.42) for ensemble H101 in the Wilson regularization. (b): the same but for the mixed action regularization for one point in our valence parameters grid, see Sec. 3. At maximal twist this quantity must vanish.
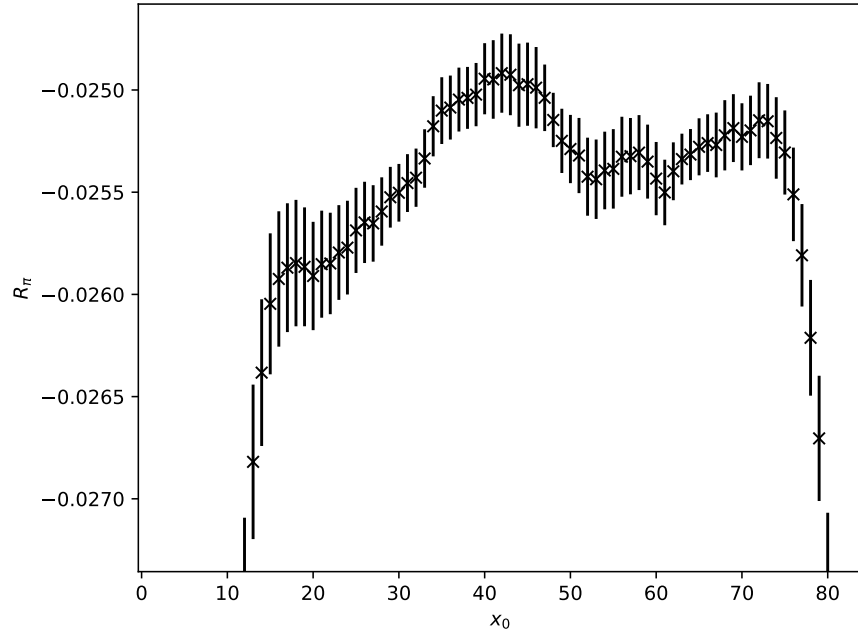
(a)
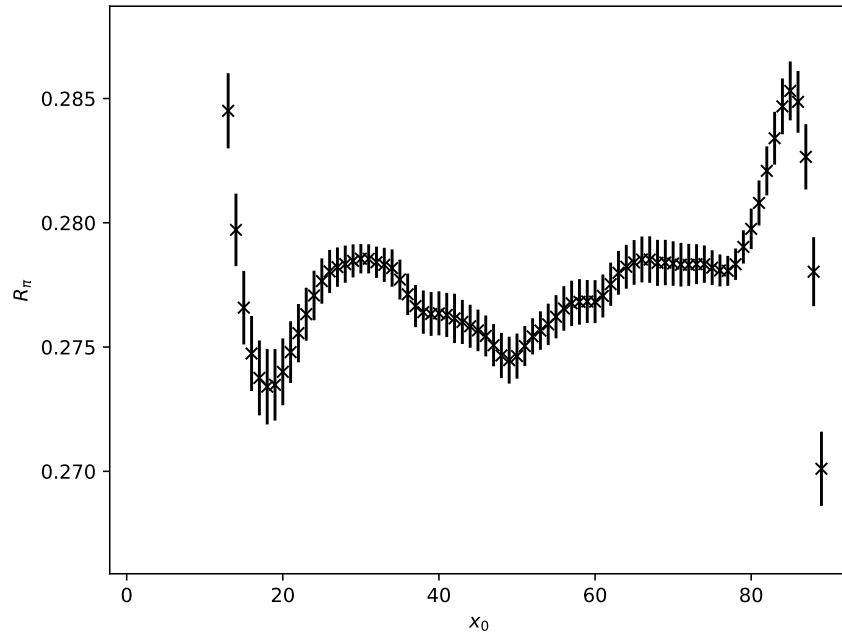
(b)

Figure 2.3: (a): vacuum-to-pion axial matrix element R_π from eq. (2.32) for ensemble H101 in the Wilson regularization. (b): vacuum-to-pion pseudoscalar matrix element R_π from eq. (2.40) in the mixed action regularization for one point in our valence parameters grid, see Sec. 3.
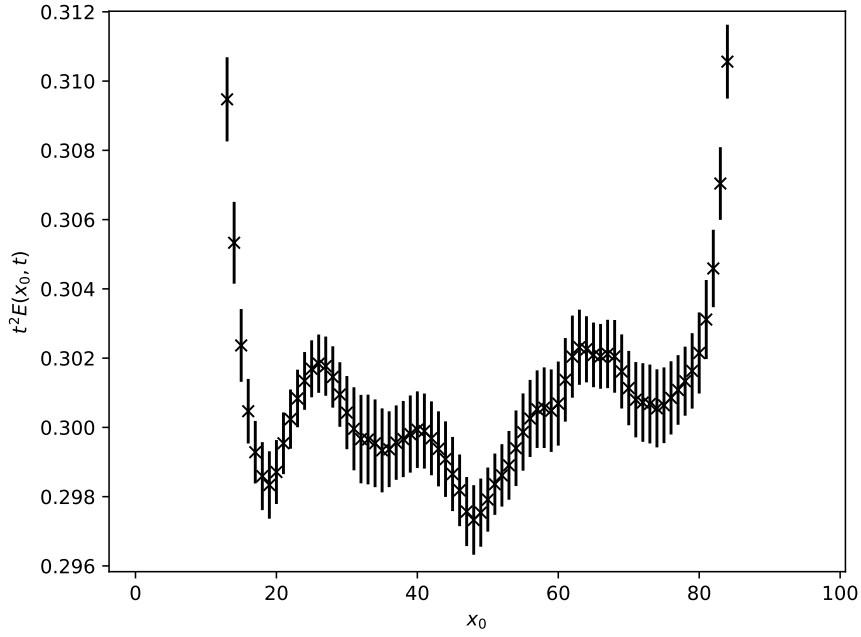
(a)
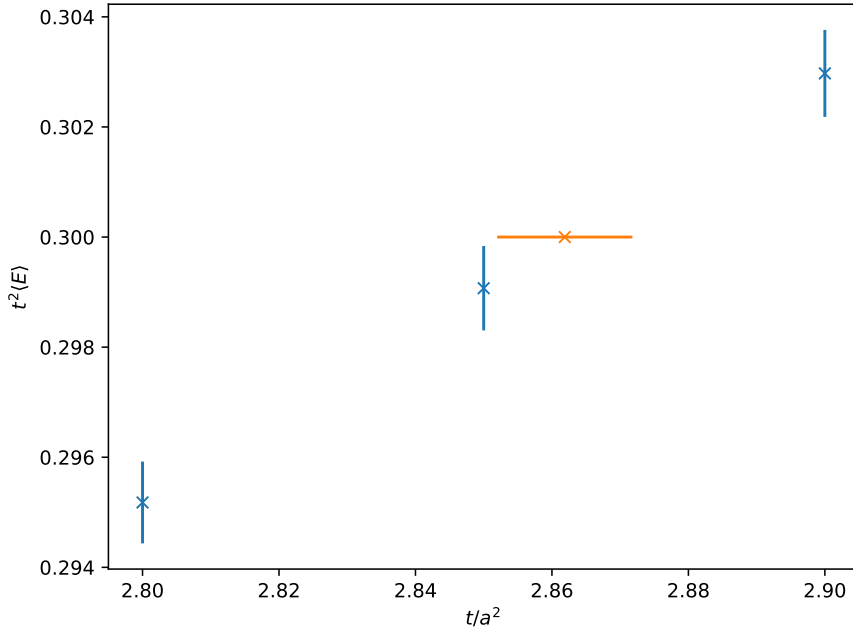
(b)

Figure 2.4: (a): $t^2 E(x_0, t)$ for one value of the flow time t/a^2 near t_0/a^2 as a function of the Euclidean time x_0/a, with $E(x_0, t)$ the space volume averaged energy density. The latter is defined in eq. (2.56). (b): Euclidean-time averaged values of $t^2 \langle E(x_0, t) \rangle_{x_0}$ for several flow times t/a^2 (blue points) near t_0/a^2 (defined in eq. (2.58)) and the interpolated result for t_0/a^2 (orange point). Results for ensemble H101.
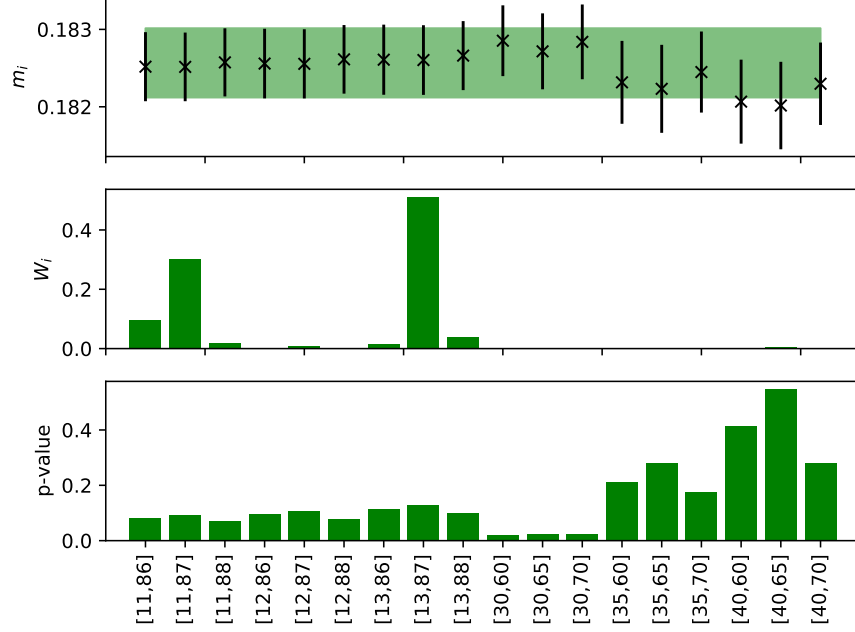
Figure 2.5: Model variation for the extraction of the ground state signal of the pion effective mass of ensemble H101 in the Wilson regularization, shown in Fig. 2.1. From top to bottom we show the ground state signal result from a fit to eq. (2.64) for each fit interval choice, the weight associated to each choice according to eq. (2.59), and the goodness of fit measured through the p-values defined in [30]. We see that the highest weights are associated to a compromise between good fits (in terms of p-values) and fits with large number of points. The right-most models in the plot are heavily penalized even though they have the best p-values, since they cut a large number of points and models with not so severe cuts get also good p-values. The band in the top figure indicates the final weighted average result with the systematic uncertainty in eq. (2.61) included.

Part III

PRECISION PHYSICS FROM A LATTICE QCD
MIXED ACTION

MIXED ACTION SETUP

3.1 MOTIVATION

The lattice setup used in this thesis is based on a mixed action with Wilson $\mathcal{O}(a)$ improved quarks (see Sec. 1.3.2) in the sea and fully twisted Wilson tm quarks (see Sec. 1.3.3) in the valence, whose goal is to control cutoff effects in the context of studies of flavor physics in the charm sector. These effects are of order $\mathcal{O}(am_c)$ with m_c the mass of the charm quark. The use of Wilson tm fermions at maximal twist allows to remove such $\mathcal{O}(am_c)$ lattice artifacts without the need of computing specific improvement coefficients proportional to the charm quark mass, thus providing an alternative way to control the continuum limit extrapolations. Furthermore, the mixed action is yet another valid lattice regularization which provides an independent way of measuring physical observables on the lattice. In this respect, it will allow us to quote independent results for the gradient flow scale t_0 (see Sec. 4), the charm quark mass and the $D_{(s)}$ mesons decay constants [34] (see Sec. 5). In the future, we also plan to extend this setup to the determination of the light and strange quark masses.

For the definition of the mixed action approach, we recall eq. (1.81)

$$\left\langle O^{ij}(x_1) O^{ji}(x_2) \right\rangle = -\frac{1}{\mathcal{Z}} \int \mathcal{D}[U] e^{-S_G[U] - S_{\text{eff}}[U]}$$
$$\times \text{tr} \left(\Gamma D_i^{-1}(x_1, x_2) \Gamma D_j^{-1}(x_2, x_1) \right), \tag{3.1}$$

$$S_{\text{eff}}[U] = -\sum_i^{N_f} \log \det(D_i). \tag{3.2}$$

We see that the Dirac operator D appears first in the Boltzmann factor $e^{-S_G[U] - S_{\text{eff}}[U]}$, which characterizes the fields of the sea sector, with which the set of gauge ensembles is generated (see Appendix E), and then in the fermionic observable whose expectation value we are interested in, depending on fields of the valence sector. The calculation is thus divided in two separate stages of the analysis: the first one corresponds to the generation of gauge ensembles, and the other to the inversion of the Dirac operator on those gauge configurations (see Appendix G). This procedure in principle allows for the use of different regularizations of the Dirac operator in these two steps or sectors of the theory. In general, a mixed action approach can introduce unitarity violations even once the continuum limit is taken, unless the physical quark masses in both sea and valence coincide. This means that our setup will require a tuning procedure in which the

values of the Wilson twisted mass parameters are chosen such that the physical values of quark masses in the valence sector are matched to the corresponding ones in the sea sector.

The flavor content of our setup is as follows: on the one hand, the sea sector has $N_f = 2+1$ flavors, i.e. two mass-degenerate light quarks (corresponding to the *u* and *d* flavors) with mass m_l and one strange quark with mass m_s. On the other hand, the valence sector consists of $N_f = 2+1+1$ flavors, thus adding a charm quark. Since we have $N_f = 2+1$ in the sea and $N_f = 2+1+1$ in the valence, the flavors we need to match are those of the light and strange quarks, treating the charm quark in the valence as a partially quenched flavor.

In order to perform the matching of the theory, we need to know beforehand the value of the quark masses in the sea sector. This means that we need lattice measurements in the fully unitary Wilson fermions setup (using the Wilson regularization in the sea and valence) in addition to the mixed action regularization. We therefore consider two sets of data: those coming from the Wilson unitary setup, which we refer to as sea or Wilson results, and those coming from the mixed action itself. The use of these two sets of data will further improve the control of the scale setting analysis, as we will see in Sec. 4. In addition to the matching of the sea and valence sectors, we also need to tune the valence action parameters to enforce full twist and automatic $\mathcal{O}(a)$ improvement.

The Chapter is structured as follows. In Sec. 3.2 we discuss the sea sector details: ensembles under study, lattice actions and boundary conditions. In Sec. 3.3 we discuss the valence sector, which employs Wilson tm quarks. In Sec. 3.4 we discuss the line of constant physics along which the ensembles under study were generated. They follow a chiral trajectory towards the physical point that suffers small mistunings and that must be corrected by performing small mass corrections. We discuss the details of a mass shifting procedure to account for these effects. Finally, in Sec. 3.5 we deal with the matching of sea and valence sectors though pseudoscalar masses in order to impose equal physical quark masses in both sectors and to recover unitarity in the continuum. We also explain the procedure to tune Wilson tm valence quarks to maximal twist.

3.2 SEA SECTOR

The gauge ensembles that we employ are CLS ensembles [31, 103] with $N_f = 2+1$ non-perturbatively $\mathcal{O}(a)$ improved Wilson fermions (see eq. (1.102)). They use the Lüscher-Weisz gauge action [84] defined in eqs. (1.94-1.95) which, following the Symanzik improvement program, is tree-level improved at $\mathcal{O}(a^2)$.

For most of the ensembles, open boundary conditions (OBC) in time are used for the gauge fields, since it has been observed that the use of

periodic boundary conditions (PBC) leads to a steep dependence in the scaling of the autocorrelation times as one approaches the continuum limit, a problem known as critical slowing down. This is related to the existence of topologically disconnected sectors in gauge field space, which prevents the algorithm to sample correctly different topological sectors. In contrast to this, OBC let the topological charge flow through the boundaries and thus improves the sampling of topological sectors. All ensembles use PBC in the spatial directions.

The ensembles we consider have 5 different values of the lattice spacing, and for each of them there is one ensemble at the symmetric point, which is defined as $m_l = m_s$, or equivalently for the hopping parameter κ (see eq. (1.50)) as $\kappa_l = \kappa_s$. As we will see, all the ensembles, reported in Table C.1, follow the chiral trajectory defined in eq. (3.6) below.

3.3 VALENCE SECTOR

In the valence sector, we employ an $N_f = 2 + 1 + 1$ fully-twisted Wilson tm fermion action (see Sec. 1.3.3), whose Dirac operator reads

$$D_W + m^{(v)} + i\mu^{(v)}\gamma_5, \tag{3.3}$$

with

$$\mu^{(v)} = \text{diag}(\mu_l, -\mu_l, -\mu_s, \mu_c)^{(v)}, \quad m^{(v)} = \text{diag}(m_l, m_l, m_s, m_c)^{(v)}. \tag{3.4}$$

In particular, we use the same standard quark mass for all flavors $m_l^{(v)} = m_s^{(v)} = m_c^{(v)} \equiv m^{(v)}$.

As discussed in Sec. 1.3.3, imposing full twist means that the twist angles α_i fulfill

$$\cot \alpha_i = \frac{m_i^R}{\mu_i^R} = 0. \tag{3.5}$$

To do so, it is enough to impose that the PCAC quark masses in eq. (2.42) vanish. When this is the case, automatic $\mathcal{O}(a)$ improvement of valence observables is obtained, up to $\mathcal{O}(a\text{tr}(M_q))$ cutoff effects due to the sea quark masses. However, these effects are expected to appear at $\mathcal{O}(g_0^4)$ in perturbation theory.

In order to set the valence parameters for which sea and valence physical quark masses are matched while simultaneously ensuring that the maximal twist condition is met, we employ a grid of valence parameter values $(\kappa, \mu_l, \mu_s)^{(v)}$ around an estimate of the target point in order to perform small interpolations that allow us to reach the target point $(\kappa, \mu_l, \mu_s)^{(v)^*}$.

3.4 CHIRAL TRAJECTORY

The set of CLS ensembles that we use are generated along the trajectory in the quark mass plane defined by a constant trace of the bare sea "(s)" quark mass matrix

$$\text{tr}\left(M_q^{(s)}\right) = 2m_l^{(s)} + m_s^{(s)} = \text{cnst.} \tag{3.6}$$

This trajectory ensures that at a given value of the lattice spacing, the improved bare coupling

$$\tilde{g}_0^2 = g_0^2 \left(1 + ab_g \text{tr}\left(M_q^{(s)}\right)\right), \tag{3.7}$$

remains constant as we vary the sea quark masses to approach the physical point. Note that for the Wilson unitary setup, sea and valence quark masses are the same, but not for the mixed action setup. To ensure that this trajectory crosses the physical point, we define the dimensionless quantities

$$\phi_2 = 8t_0 m_\pi^2, \tag{3.8}$$

$$\phi_4 = 8t_0 \left(m_K^2 + \frac{1}{2}m_\pi^2\right), \tag{3.9}$$

which at leading order (LO) ChPT are proportional to the renormalized quark masses

$$\phi_2 \propto m_l^{R}, \tag{3.10}$$

$$\phi_4 \propto 2m_l^{R} + m_s^{R} = \text{tr}\left(M_q^{R}\right). \tag{3.11}$$

The trace of the renormalized quark mass matrix $\text{tr}\left(M_q^{R}\right)$ is in turn proportional to the bare quark mass matrix up to $\mathcal{O}(a)$ cutoff effects

$$\text{tr}\left(M_q^{R}\right) = Z_m r_m \left[\left(1 + a\bar{d}_m \text{tr}\left(M_q\right)\right) \text{tr}\left(M_q\right) + a d_m \text{tr}\left(M_q^2\right)\right]. \tag{3.12}$$

Thus, setting the sea value of ϕ_4 to its physical value for all ensembles ensures that eq. (3.6) holds and goes through the physical point, up to small mistunings due to higher terms in the chiral expansion and to cutoff effects.

To correct for these mistunings, we perform small mass shifts [29] in the bare sea quark masses by Taylor expanding lattice observables at first order as follows

$$O\left(m_l^{(s)'}, m_s^{(s)'}\right) = O\left(m_l^{(s)}, m_s^{(s)}\right) + \sum_q \left(m_q^{(s)'} - m_q^{(s)}\right) \frac{dO}{dm_q^{(s)}}, \tag{3.13}$$

with the total derivative given by

$$\frac{dO}{dm_q^{(s)}} = \sum_i \frac{\partial O}{\partial \langle P_i \rangle} \left[\left\langle \frac{\partial P_i}{\partial m_q^{(s)}} \right\rangle - \left\langle P_i \frac{\partial S}{\partial m_q^{(s)}} \right\rangle + \langle P_i \rangle \left\langle \frac{\partial S}{\partial m_q^{(s)}} \right\rangle\right]. \tag{3.14}$$

Here $O = O(\{P_i\})$ is an arbitrary lattice observable and $\{P_i\}_{i=1,2,...}$ is the set of primary observables on which it depends, in our case the corresponding mesonic two-point functions and the flow action density. The first term within the square brackets in the right-hand side of this equation corresponds to the valence contribution to the derivative, while the two subsequent terms involving the action S correspond to the sea contributions. Note that for the Wilson unitary setup, all terms contribute in fermionic observables, while for the mixed action setup, since the two-point functions $\{P_i\}$ do not depend explicitly on $m_q^{(s)}$, the first term in the right-hand side of eq. (3.14) vanishes in fermionic observables. For the gradient flow scale t_0, only the terms involving the action S in eq. (3.14) contribute.

In particular, the sum over q in eq. (3.13) can be done in any direction of the quark mass plane, and following [124] we choose to mass shift only the strange quark. For practical purposes, since for each ensemble we mass shift all relevant observables to the physical value of ϕ_4 in the sea sector $\phi_4^{(s)} = \phi_4^{ph} = $ const., following [123] we rewrite the Taylor expansion at first order as

$$O\left(\phi_4^{(s)'} = \phi_4^{ph}\right) = O\left(\phi_4^{(s)}\right) + \left(\phi_4^{ph} - \phi_4^{(s)}\right)\frac{dO}{d\phi_4^{(s)}}, \tag{3.15}$$

with

$$\frac{dO}{d\phi_4^{(s)}} = \frac{dO/dm_s^{(s)}}{d\phi_4^{(s)}/dm_s^{(s)}}. \tag{3.16}$$

Note that the sea value $\phi_4^{(s)}$ is given by ϕ_4 computed in the Wilson unitary setup, and its derivative has both sea and valence contributions. On the other hand, as previously commented, $dO/dm_s^{(s)}$ receives valence and sea contributions when O is a fermionic observable computed in the Wilson unitary setup, and only sea contributions when computed in the mixed action regularization. The mass shift to ϕ_4^{ph} can be carried out simultaneously in the sea and valence sectors by imposing $\phi_4^{(s)} = \phi_4^{ph}$ and simply selecting the same values for the sea and valence hopping parameters κ, which is the case of the fully unitary Wilson setup. On the other hand, the mass shift in the mixed action requires to first mass shift the sea quark masses to impose $\phi_4^{(s)} = \phi_4^{ph}$ and then tune the valence value of ϕ_4 to its physical value, which is done through the matching between sea and valence sectors (see Sec. 3.5). This furthermore implies the equality of the values of ϕ_4 in the unitary and mixed action setups.

The observables we will be interested in for the scale setting (see Sec. 4) are $\sqrt{t_0}f_\pi$, $\sqrt{t_0}f_K$ and $\sqrt{t_0}f_{\pi K}$, the latter defined in eq. (4.1). All these quantities are physical and so are their derivatives with respect to $\phi_4^{(s)}$. Thus, one can measure these derivatives for each ensemble and then fit them as a function of ϕ_2 and the lattice spacing. The

resulting parametrization can then be used to perform the mass shifts as an alternative to using the dedicated measurements of $dO/d\phi_4^{(s)}$ on each ensemble. This has the advantage of improving the precision for observables whose mass derivatives are noisy or missing, which is particularly relevant for the finest lattice spacing and the most chiral ensembles under study. We also include the derivatives of $\sqrt{t_0}m_{12}^R$ with respect to $\phi_4^{(s)}$ in the mixed action setup since we will need to mass shift this quantity in order to tune to full twist (see Sec. 3.5).

The dependence on the light-quark mass and lattice spacing of the derivatives can be described by the following fit form

$$F = A + B\phi_2 + D\frac{a^2}{t_0}, \tag{3.17}$$

for all choices of O except for the light PCAC quark mass in the mixed action setup, for which we require additional parameters to properly describe the lattice data

$$F = A + B\phi_2 + C\phi_2^2 + (D + E\phi_2)\frac{a^2}{t_0}. \tag{3.18}$$

In the case of $d\phi_2/d\phi_4^{(s)}$ in the Wilson unitary setup, we exclude the symmetric point ensembles from the fit to eq. (3.17) since in this setup $\phi_2^{\text{sym}} = \frac{2}{3}\phi_4$ by construction. Thus, in this case we will use this relation directly to mass shift ϕ_2.

Results for the fit parameters of eqs. (3.17-3.18) are presented in Table 3.1, while plots are shown in Figs. 3.1-3.6.

The mass shifts have to be performed to the physical value of ϕ_4 in eq. (3.9). However, in order to determine it we first need to input the physical value of the intermediate scale t_0, which is the target of the analysis. Thus, we start the process with an educated guess of t_0^{ph}, which provides an initial guess for ϕ_4^{ph}. Once the scale setting procedure is carried out and a new determination of t_0 is thus obtained, the analysis is iterated by updating the value of ϕ_4 to which the ensembles are mass shifted, until convergence in the determination of t_0 is observed. The initial guess used for $t_0^{\text{ph, guess}}$ can be selected as a value without error. After a few iterative steps of the analysis, we obtain the new estimate

$$\sqrt{t_0^{\text{ph, guess}}} = 0.1445(6) \text{ fm}, \tag{3.19}$$

where the uncertainty keeps all the correlations with the lattice data entering the analysis. Eq. (3.19) determines the value of ϕ_4^{ph} to which we perform the mass shifts in the subsequent sections, the input values for physical m_π and m_K given in eq. (4.3).

O	A	B	C	D	E

Figure 3.1: Derivative $d\left(\sqrt{t_0}f_{\pi K}\right)/d\phi_4^{(s)}$ for the Wilson unitary setup. For the fit eq. (3.17) was used. Results for the fit parameters are presented in Table 3.1.

$\sqrt{t_0}f_{\pi K}^{W}$	0.017(8)	-0.007(10)	-	0.024(26)	-
$\sqrt{t_0}f_{\pi}^{W}$	0.006(8)	0.008(9)	-	0.020(26)	-
$\sqrt{t_0}f_K^{W}$	0.024(10)	-0.016(11)	-	0.022(27)	-
ϕ_2^{W}	0.004(36)	0.131(92)	-	0.874(129)	-
t_0/a^2	-0.437(84)	0.214(101)	-	-0.264(274)	-
$\sqrt{t_0}f_{\pi K}^{tm}$	-0.009(7)	0.011(8)	-	-0.014(18)	-
$\sqrt{t_0}f_{\pi}^{tm}$	-0.007(6)	0.013(8)	-	-0.028(18)	-
$\sqrt{t_0}f_K^{tm}$	-0.009(8)	0.010(10)	-	-0.006(18)	-
$\sqrt{t_0}m_{12}^{tm,\,R}$	-0.004(3)	0.035(10)	-0.041(9)	0.020(16)	0.026(24)
ϕ_2^{tm}	0.031(17)	-0.032(23)	-	-0.102(73)	-
ϕ_4^{tm}	0.006(37)	0.050(47)	-	-0.298(126)	-

Table 3.1: Results for the fit parameters in eqs. (3.17-3.18) for derivatives in eq. (3.16) of the lattice observables that will be used in the analysis. The superscript "W" refers to the observable being computed in the Wilson unitary setup, while "tm" refers to the mixed action setup.
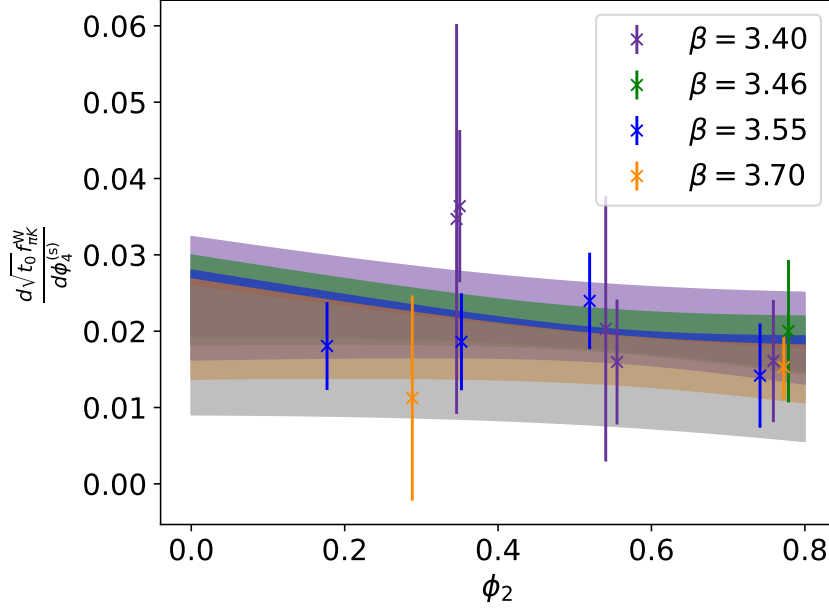
Figure 3.2: Derivative $d\phi_2/d\phi_4^{(s)}$ for the Wilson unitary setup. For the fit eq. (3.17) was used. Results for the fit parameters are presented in Table 3.1. The points around $\phi\sim0.7$ correspond to the symmetric point at which by construction $\phi_2 = \frac{2}{3}\phi_4$.

Figure 3.3: Derivative $d\left(\sqrt{t_0}f_{\pi K}\right)/d\phi_4^{(s)}$ for the mixed action setup. For the fit eq. (3.17) was used. Results for the fit parameters are presented in Table 3.1.

Figure 3.4: Derivative $d\left(\sqrt{t_0}m_{12}^{\mathrm{R}}\right)/d\phi_4^{(s)}$ for the mixed action setup. For the fit eq. (3.18) was used. Results for the fit parameters are presented in Table 3.1.

Figure 3.5: Derivative $d\phi_2/d\phi_4^{(s)}$ for the mixed action setup. For the fit eq. (3.17) was used. Results for the fit parameters are presented in Table 3.1.
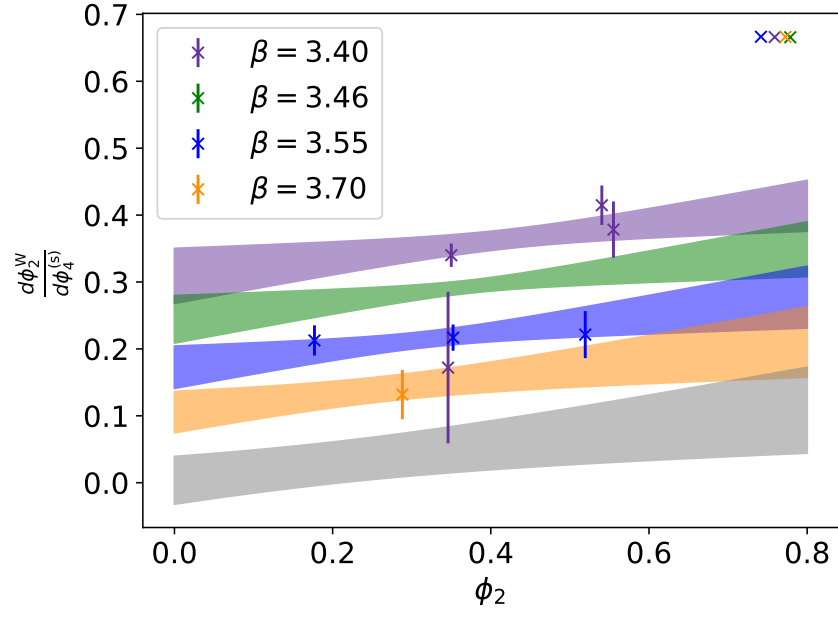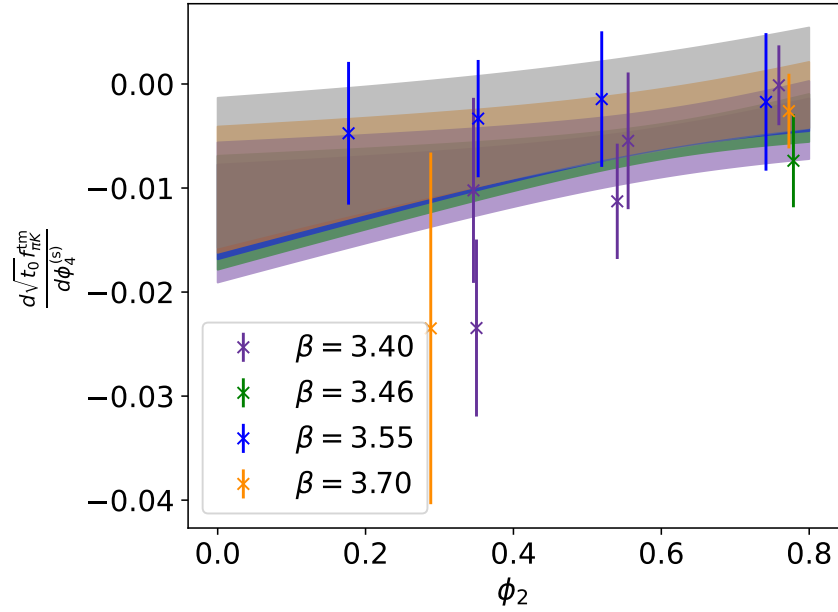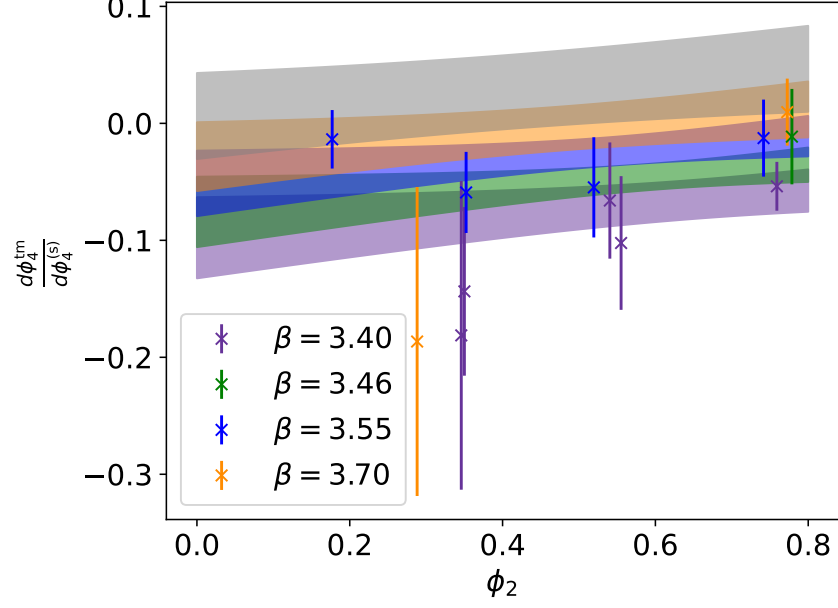
Figure 3.6: Derivative $d\phi_4/d\phi_4^{(s)}$ for the mixed action setup. For the fit eq. (3.17) was used. Results for the fit parameters are presented in Table 3.1.
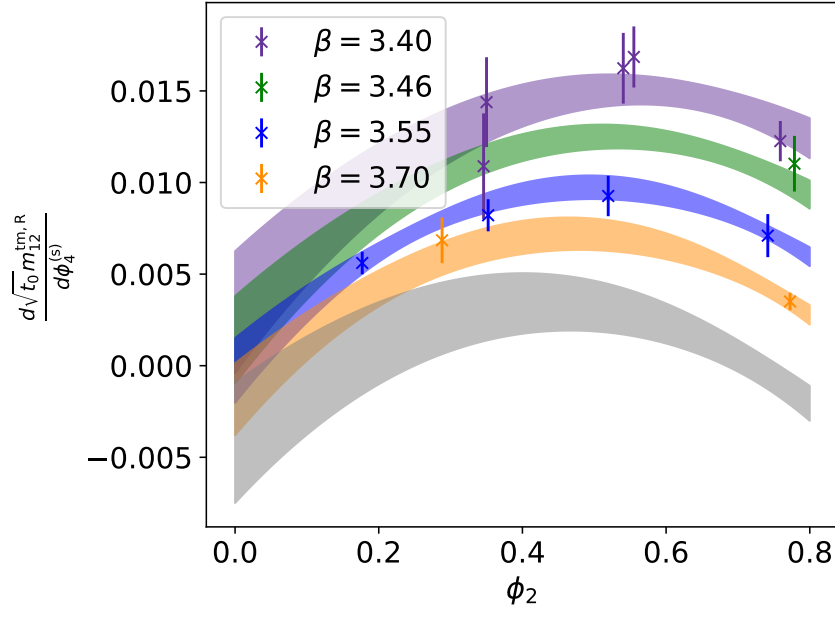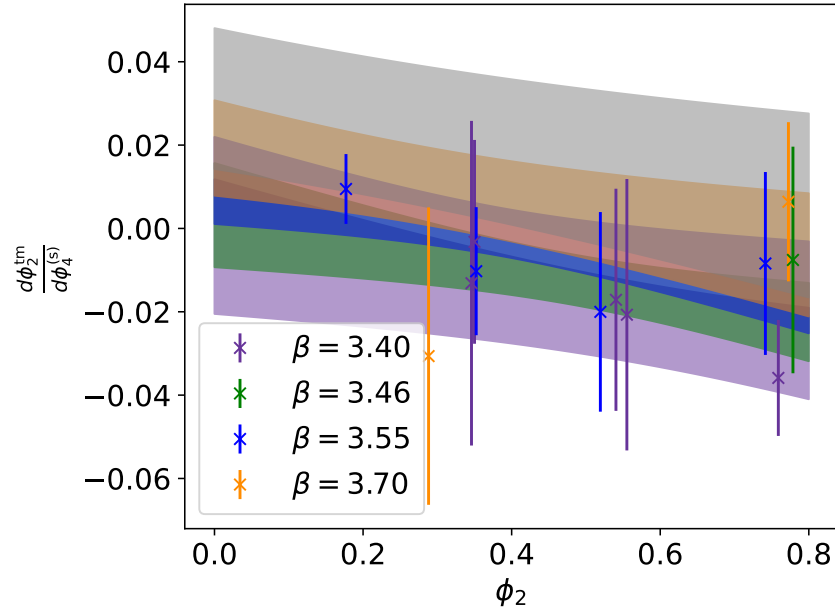
3.5   MATCHING AND TUNING TO FULL TWIST

As explained in Sec. 3.3, when working with a mixed action, after performing the mass shifts in Sec. 3.4, we need to match the physical quark masses of the sea and valence sectors. To do this, we use a grid of valence parameter values to find the target point through small interpolations. In order to know the values of the relevant observables in the sea, we use measurements in the fully Wilson unitary setup. In practice, to compute the physical values (renormalized and improved) of quark masses we need the relevant improvement coefficients. In order not to rely on these for the matching procedure, instead of matching the physical quark masses we choose to use the pion and kaon masses in units of the gradient flow scale t_0

$$\phi_2^{(s)} = \phi_2^{(v)}, \tag{3.20}$$

$$\phi_4^{(s)} = \phi_4^{(v)}. \tag{3.21}$$

since these quantities are proportional to the physical quark masses at LO ChPT (see eqs. (3.8-3.9)).

Furthermore, we need to tune the Wilson tm action to full twist, which means setting the valence light PCAC quark mass to zero

$$m_{ud}^{(v)} \equiv m_{ll'}^{(v)} \equiv m_{12}^{(v)} = 0. \tag{3.22}$$

Setting the maximal twist condition through a vanishing value of the light valence PCAC quark mass, as in eq (3.22), is sufficient to guaran-

tee the absence of lattice artifacts of $\mathcal{O}(a)$ in physical observables [24, 58].

To impose eqs. (3.20-3.22), we perform interpolations of the valence observables $m_{12}^{(v)}, \phi_2^{(v)}, \phi_4^{(v)}$ in the $(\kappa, \mu_l, \mu_s)^{(v)}$ hyperplane, using as fit functions the following expressions motivated by ChPT

$$m_{12}^{(v)} = p_1 \left(\frac{1}{\kappa^{(v)}} - \frac{1}{\kappa^{(v)*}} \right) + p_2 \left(\mu_l^{(v)} - \mu_l^{(v)*} \right), \tag{3.23}$$

$$\phi_2^{(v)} = \frac{p_3}{\mu_l^{(v)}} \left(\frac{1}{\kappa^{(v)}} - \frac{1}{\kappa^{(v)*}} \right)^2 + p_4 \left(\mu_l^{(v)} - \mu_l^{(v)*} \right) + \phi_2^{(s)}, \tag{3.24}$$

$$\phi_4^{(v)} = \frac{p_5}{\mu_l^{(v)}} \left(\frac{1}{\kappa^{(v)}} - \frac{1}{\kappa^{(v)*}} \right)^2 + \frac{p_6}{\mu_s^{(v)}} \left(\frac{1}{\kappa^{(v)}} - \frac{1}{\kappa^{(v)*}} \right)^2$$
$$+ p_7 \left(\mu_l^{(v)} - \mu_l^{(v)*} \right) + p_8 \left(\mu_s^{(v)} - \mu_s^{(v)*} \right) + \phi_4^{(s)}. \tag{3.25}$$

In this way, the target point values $(\kappa, \mu_l, \mu_s)^{(v)*}$ are found as fit parameters of a simultaneous fit of these three quantities. The interpolation is shown in Fig. 3.7.

The mixed action results for the quark masses are given by the target twist mass parameters $\mu_{l,s}^{(v)*}$, while the extraction of the pion and kaon decay constants in the mixed action setup requires an additional interpolation along the valence grid to the target point. The fit functions for this interpolation are

$$f_\pi^{(v)} = q_1 \left(\frac{1}{\kappa^{(v)}} - \frac{1}{\kappa^{(v)*}} \right)^2 + q_2 \left(\frac{1}{\kappa^{(v)}} - \frac{1}{\kappa^{(v)*}} \right) + q_3 \mu_l^{(v)}, \tag{3.26}$$

$$f_K^{(v)} = r_1 \left(\frac{1}{\kappa^{(v)}} - \frac{1}{\kappa^{(v)*}} \right)^2 + r_2 \left(\frac{1}{\kappa^{(v)}} - \frac{1}{\kappa^{(v)*}} \right) + r_3 \mu_l^{(v)} + r_4 \mu_s^{(v)}. \tag{3.27}$$

The interpolation for the decay constants combination $f_{\pi K}$ defined in eq. (4.1) is shown in Fig. 3.8.
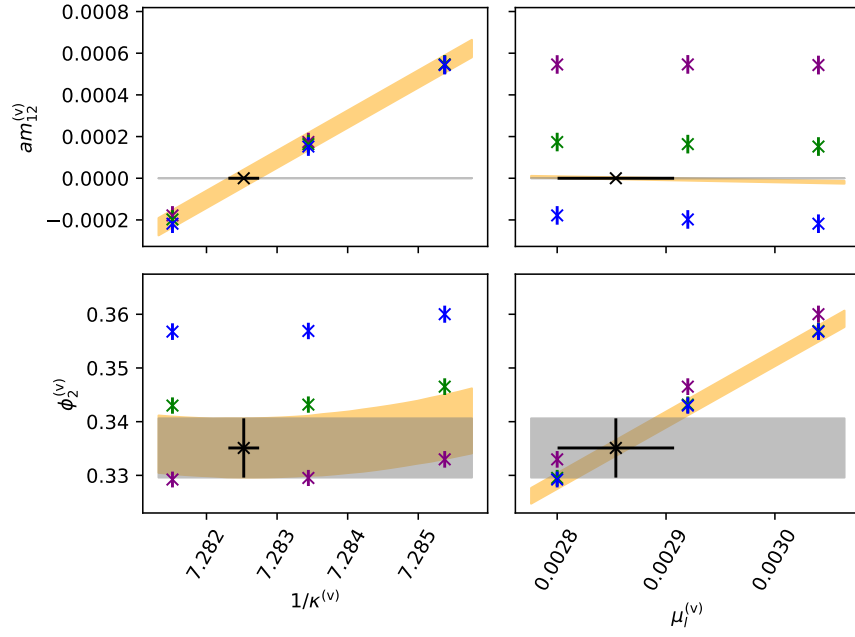
Figure 3.7: Matching of sea (gray horizontal band) and valence values of ϕ_2 (lower panels) and tuning to full twist $am_{12}^{(v)} = 0$ (upper panels) along the grid of valence parameters values for the ensemble H105. Each point represents a different measurement in the valence along the grid, and the orange band represents the interpolation. The black point is the target result $(\kappa, \mu_l, \mu_s)^{(v)*}$. Here we only show the matching of $\phi_2^{(v)}$ and $am_{12}^{(v)}$, though the matching of $\phi_4^{(v)}$ is done simultaneously.
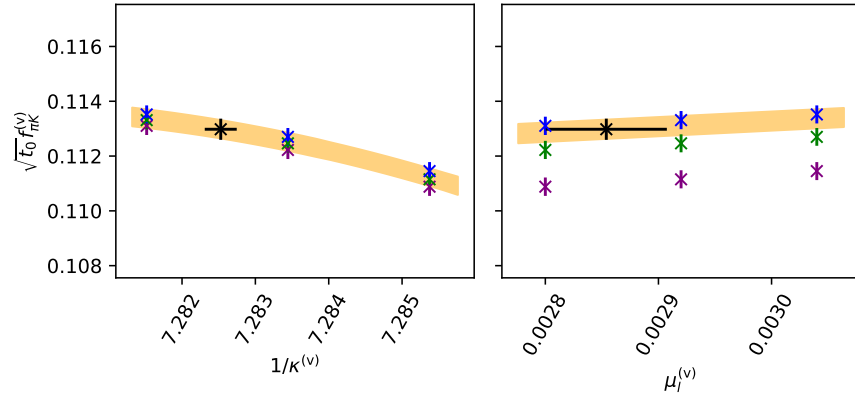
Figure 3.8: Interpolation of $\sqrt{t_0}f_{\pi K}$ (see eq. (4.1)) along the valence grid to the target point $(\kappa, \mu_l, \mu_s)^{(v)*}$ for the ensemble H105. The points with different colors represent measurements at different values of the valence parameters.

SCALE SETTING

4.1 MOTIVATION

The scale setting involves the precise determination of one reference observable, the scale, in physical units, to which any other observable is compared in order to extract the value of the latter in physical units.

We will use the gradient flow scale t_0 introduced in Sec. 2.6 as an intermediate reference scale since it can be computed on the lattice with high precision. Following the discussion in Sec. 1.7, we choose for the phenomenological input the linear combination of the decay constants of the pion and kaon [29]

$$\Lambda \equiv f_{\pi K} = \frac{2}{3}\left(f_K + \frac{1}{2}f_\pi\right).\tag{4.1}$$

After measuring $\sqrt{t_0}f_{\pi K}$ for each ensemble, one must perform a chiral-continuum extrapolation in order to extract its value at physical values of the quark masses and in the continuum. To define the physical point we use the pion and kaon physical masses, or equivalently the dimensionless quantities ϕ_2 and ϕ_4 in eqs. (3.8-3.9). Thanks to the mass shifting procedure in Sec. 3.4, the value of ϕ_4 is kept fixed to its physical value along our trajectory in the quark mass plane, and as a result the chiral extrapolation needs to be done in ϕ_2 only. For the determination of the physical value of the latter we use the initial guess in eq. (3.19) and the physical input in eq. (4.3). As commented in Sec. 3.4, once a new determination of t_0 at the physical point is obtained, the analysis is iterated updating the value in eq. (3.19) until convergence is observed. Thus, with each iterative step both the values of ϕ_2 to which we perform the chiral extrapolation and the value of ϕ_4 to which we shift our observables are updated.

We employ an $\mathcal{O}(a)$ improved lattice action. Furthermore, in the calculation of $\sqrt{8t_0}f_{\pi K}$ we employ the relevant improvement coefficients to remove $\mathcal{O}(a)$ lattice artifacts for the Wilson unitary setup. On the other hand, in the mixed action setup, we employ all known improvement coefficients in addition to relying on the $\mathcal{O}(a)$ improvement mechanism at maximal twist. Therefore, we expect lattice artifacts to start at $\mathcal{O}(a^2)$ for $\sqrt{t_0}f_{\pi K}$.

In order to perform the chiral-continuum limit, we explore different ways of parameterizing the dependence on ϕ_2 (ϕ_4 is constant thanks to the mass shifting procedure of Sec. 3.4) and on the lattice spacing a, and employ the model averaging techniques introduced in Sec. 2.7.

After performing the chiral-continuum limit, using as external physical input the values of the pion and kaon decay constants we can determine the value of the scale t_0 as

$$\sqrt{t_0^{\text{ph}}} = \frac{\left(\sqrt{t_0}f_{\pi K}\right)^{\text{latt}}\Big|_{\phi_2^{\text{ph}},\, a=0}}{f_{\pi K}^{\text{exp}}}. \tag{4.2}$$

Specifically, we consider ensembles with $N_f = 2+1$ dynamical quarks, and thus assume isospin symmetry for the up and down flavors. Since we work in the limit of isosymmetric QCD (isoQCD), in which electromagnetic and strong isospin corrections are not explicitly included, we need to use a prescription to define the physical inputs in this limit. We opt for the values proposed in [5]

$$m_\pi^{\text{isoQCD}} = 134.9768(5) \text{ MeV}, \quad m_K^{\text{isoQCD}} = 497.611(13) \text{ MeV}, \tag{4.3}$$

$$f_\pi^{\text{isoQCD}} = 130.56(2)_{\text{exp}}(13)_{\text{QED}}(2)_{|V_{ud}|} \text{ MeV}, \tag{4.4}$$

$$f_K^{\text{isoQCD}} = 157.2(2)_{\text{exp}}(2)_{\text{QED}}(4)_{|V_{us}|} \text{ MeV}. \tag{4.5}$$

The kaon decay constant receives a large contribution to its uncertainty from the determination of the $|V_{us}|$ CKM matrix element. QED corrections are also more significant in the kaon decay constant as compared to the pion case. Although not relying on the kaon decay constant seems a desirable option, controlling the systematic uncertainties of the chiral-continuum extrapolation of f_π is at present more challenging than that of f_K.

4.2 DETERMINATION OF $\sqrt{t_0}$ AT THE PHYSICAL POINT

The choice of the combination of decay constants $f_{\pi K}$ in eq. (4.1) to set the scale is motivated by its chiral behavior, since at fixed value of ϕ_4 its next-to-leading order (NLO) $SU(3)$ ChPT expression only depends on ϕ_2 through chiral logarithms. To this order we have, using $m_u = m_d \equiv m_l$ [4, 11]

$$t_0 = t_{0,\text{ch}}\left(1 + k_1 \frac{2m_K^2 + m_\pi^2}{(4\pi f)^2}\right), \tag{4.6}$$

$$f_\pi = f\left[1 + \frac{16B_0 L_5}{f^2}m_l + \frac{16B_0 L_4}{f^2}(2m_l + m_s) - 2L(m_\pi^2)\right. \left. - L(m_K^2)\right], \tag{4.7}$$

$$f_K = f\left[1 + \frac{8B_0 L_5}{f^2}(m_l + m_s) + \frac{16B_0 L_4}{f^2}(2m_l + m_s)\right. \left. - \frac{3}{4}L(m_\pi^2) - \frac{3}{2}L(m_K^2) - \frac{3}{4}L(m_\eta^2)\right], \tag{4.8}$$

where $L(x)$ are chiral logarithms, defined as

$$L(x) = \frac{x}{(4\pi f)^2}\log\frac{x}{(4\pi f)^2}, \tag{4.9}$$

and $f, t_{0,\mathrm{ch}}, k_1, B_0, L_i$ are low energy constants (LECs). The quark masses can be related to meson masses using the LO expressions

$$m_\pi^2 = 2B_0 m_l, \tag{4.10}$$

$$m_K^2 = B_0(m_l + m_s), \tag{4.11}$$

$$m_\eta^2 = \frac{4}{3}m_K^2 - \frac{1}{3}m_\pi^2. \tag{4.12}$$

This way, the combination $\sqrt{8t_0}f_{\pi K}$ reads

$$
\begin{aligned}
F_{\chi SU(3),\pi K}^{\mathrm{cont}}(\phi_2) &\equiv \left(\sqrt{8t_0}f_{\pi K}\right)^{\mathrm{cont}} = \\
&= \frac{A}{4\pi}\left[1 - \frac{7}{6}\tilde{L}\left(\frac{\phi_2}{A^2}\right) - \frac{4}{3}\tilde{L}\left(\frac{\phi_4 - \frac{1}{2}\phi_2}{A^2}\right)\right. \\
&\quad \left. - \frac{1}{2}\tilde{L}\left(\frac{\frac{4}{3}\phi_4 - \phi_2}{A^2}\right) + \frac{B}{A^2}\phi_4\right],
\end{aligned}
\tag{4.13}
$$

with modified chiral logarithms given by

$$\tilde{L}(x) = x\log(x), \tag{4.14}$$

and where we absorbed the LECs into the definition of the parameters A, B as

$$A = 4\pi\sqrt{8t_{0,\mathrm{ch}}}f, \tag{4.15}$$

$$B = \frac{(16\pi)^2}{3}(L_5 + 3L_4) + k_1. \tag{4.16}$$

We use the expression in eq. (4.13) to perform the chiral-continuum extrapolation of $\sqrt{8t_0}f_{\pi K}$. We will use the label $[SU(3)\chi PT]$ for this continuum mass-dependence.

To probe the systematic effects associated with chiral extrapolation, in addition to the $SU(3)$ ChPT expressions, we also consider $SU(2)$ formulae in which the mass dependence of the strange quark is absorbed in the corresponding LECs. The expressions at NLO reads [3]

$$f_\pi = f\left[1 + \frac{8(2L_4 + L_5)}{f^2}m_\pi^2 - 2L(m_\pi^2)\right], \tag{4.17}$$

$$f_K = f^{(K)}(m_s)\left[1 + \frac{c(m_s)}{f^2}m_\pi^2 - \frac{3}{4}L(m_\pi^2)\right]. \tag{4.18}$$

More specifically, we either consider the case in which $f^{(K)}(m_s)$ and $c(m_s)$ follow a linear dependence on m_s or in which they remain constant. Since in the expression of f_π in eq. (4.17), the dependence on m_s appears only through sea quark loop effects, we assume that the LECs f and $L_{4,5}$ are independent of m_s. After some algebra, we arrive at

$$F_{\chi SU(2),}^{\mathrm{cont}}(\phi_2) = B + C\phi_2 + D\phi_4 - E\tilde{L}\left(\frac{\phi_2}{A^2}\right), \tag{4.19}$$

With the fit parameters A, B, C, D, E combinations of the LECs appearing in eqs. (4.17-4.18). Since we mass shifted to a constant value of ϕ_4, the fit cannot distinguish between B and $D\phi_4$, and we may group these two terms into a single term in order to reduce the number of fit parameters. A term of type $D\phi_4$ may arise from the chiral expansion of t_0 in eq. (4.6) even when $f^{(K)}(m_s)$ and $c(m_s)$ are considered to be independent of m_s.

Another possibility for the extrapolation to the physical point is to use Taylor expansions in ϕ_2 around the symmetric point. We have considered Taylor expansions to the second and fourth order as follows

$$F_{\text{Tay},\pi K}^{\text{cont}}(\phi_2) \equiv \sqrt{8t_0} f_{\pi K}^{\text{cont}} = A + B \left(\phi_2 - \phi_2^{\text{sym}}\right)^2, \tag{4.20}$$

or

$$F_{\text{Tay},\pi K}^{\text{cont}}(\phi_2) = A + B \left(\phi_2 - \phi_2^{\text{sym}}\right)^2 + C \left(\phi_2 - \phi_2^{\text{sym}}\right)^4, \tag{4.21}$$

labeling these models as $[Tay]$ and $[Tay4]$. Due to symmetry reasons [17], there are no terms with odd powers of $\phi_2 - \phi_2^{\text{sym}}$.

In addition to the extrapolation in the pion mass, we need to supplement these fit functions with cutoff effects in order to describe our lattice data. To this end, we will explore three possibilities

$$F^{\text{latt}}(\phi_2) = F^{\text{cont}}(\phi_2) + W \frac{a^2}{8t_0}, \tag{4.22}$$

$$F^{\text{latt}}(\phi_2) = F^{\text{cont}}(\phi_2) + W \frac{a^2}{8t_0} \alpha_S^{\Gamma}(a), \tag{4.23}$$

$$F^{\text{latt}}(\phi_2) = F^{\text{cont}}(\phi_2) + (W + Z\phi_2) \frac{a^2}{8t_0}. \tag{4.24}$$

We assign the labels $[a^2]$, $[a^2 \alpha_S^{\Gamma}]$ and $[a^2 + a^2 \phi_2]$ to characterize the lattice artifacts of these models, respectively. The lattice artifact in eq. (4.23) is motivated by [77] where logarithmic corrections in the lattice spacing a are analyzed. In particular, a set of possible powers Γ_i are found to contribute.

Since it is not feasible to include several independent fitting parameters to characterize these logarithmic corrections, we chose to include a single such term. We vary the choice of Γ_i by monitoring its impact on the extracted value of t_0^{phys} after averaging over the set of models. As t_0^{phys} is observed to be independent of the choice of Γ_i, we restrict ourselves to the smallest value, $\Gamma_i = -0.111$, in the model average.

The systematic uncertainty in the extraction of $\sqrt{t_0^{\text{ph}}}$ is assessed by the model variation using the TIC introduced in Sec. 2.7. We vary over the different ways of performing the chiral-continuum limits introduced above, as well as over the possibility of performing data

cuts. In particular, we consider the following cuts (in addition to the "no cut" choice)

$$\beta > 3.40, \tag{4.25}$$

$$\beta > 3.46, \tag{4.26}$$

$$m_\pi < 420 \text{ MeV}, \tag{4.27}$$

$$m_\pi < 350 \text{ MeV}, \tag{4.28}$$

$$\beta > 3.40 \ \& \ \phi_2 < 0.6, \tag{4.29}$$

$$m_\pi L > 4.1, \tag{4.30}$$

meaning that for each cut we keep only ensembles satisfying the corresponding condition above. With these cut choices, we explore the systematic uncertainty associated with performing lattice simulations at coarse lattice spacings, pion masses significantly heavier than in Nature, and small volumes that may introduce finite volume effects.

In general, the models included in the model average correspond to good fits in terms of their p-values (see Tables K.2-K.4). This means that the TIC will tend to heavily penalize any cut in the data, since the lattice data can be well described by the fit functions explored without any performing cuts. As a result, we observe that data points with the coarsest value of lattice spacing and/or with heavier pion masses – which tend to have smaller uncertainties than those closer to the continuum and the physical point – strongly constrain the model selection based on the TIC. In addition, the TIC introduces a strong penalization to models involving cuts in the data and, as a result, the systematic effects associated with, for instance, the removal of the coarsest lattice spacing or of heaviest pion mass data are not always satisfactorily explored in such a model averaging framework. We therefore wish to extend the model averaging approach to introduce information on the regime of parameters in which the effective theories involved in the chiral-continuum extrapolations are known to perform best. For the case of the Symanzik expansion, this corresponds to the regime of smaller values of the lattice spacing, while for chiral perturbation theory it corresponds to the smaller values of the pion mass. The idea [47] is to supplement the weight matrix $\mathcal{W}$ appearing in the definition of the χ^2 of the fit (see Appendix H) with a systematic error penalization for small values of the inverse coupling β and heavy pions, according to

$$\mathcal{W}_{ij}^{-1} = C_{ij} \times \sqrt{1 + c_i^2/C_{ii}} \sqrt{1 + c_j^2/C_{jj}}, \tag{4.31}$$

where C_{ij} is the elemt of the covariance matrix of the lattice data of $\sqrt{8t_0}f_{\pi K}$ for the ensembles i and j, and c_i is a penalization factor given by

$$c_i^2 = c_\beta^2 \left(\frac{a^2}{8t_0} \right)^4 + c_{\phi_2}^2 \phi_2^4, \tag{4.32}$$

which is motivated by the fact that at coarse lattice spacings we expect $\mathcal{O}(a^4)$ cutoff effects to be relevant, and for heavy pions we expect that higher order effects of $\mathcal{O}(m_\pi^4)$ in the chiral expansion could play a role. More specifically, the penalization in β will only be applied in $\beta = 3.40$ ensembles, while the penalization in ϕ_2 acts only on symmetric point ensembles $\phi_2 \sim 0.73$. The coefficients c_{β,ϕ_2} in eq. (4.32) are chosen such that the elements of the weight matrix $\mathcal{W}$ appearing in the χ^2 function (see Appendix H) for ensembles at the symmetric point or at the coarsest lattice spacing, are no longer significantly enhanced with respect to those lying closer to the continuum or at the physical pion mass. We remark that the determination of the expectation value of the χ^2 allows to determine the p-value of a fit based on a generic weight matrix $\mathcal{W}$ [30] such as that in eq. (4.31). As expected, in the presence of an additional term in the χ^2 that suppresses the relative weights of the coarsest lattice spacing and the heaviest pion masses, we observe that the p-values of the fits without cuts are similar to those of the fits implementing the cuts $\beta > 3.40$ and $m_\pi < 420$ MeV. Moreover, the weights in the model average are more evenly distributed compared to the case in which we do not include systematic effects in the χ^2 function. Setting any of the c_{β,ϕ_2} coefficients to infinity is equivalent to performing the cut $\beta > 3.40$ or $m_\pi < 420$ MeV, while setting them to zero corresponds to the absence of cut.

As anticipated, we will carry out the chiral-continuum extrapolations using two sets of lattice data: the Wilson unitary setup and the mixed action. Universality arguments imply that the two regularizations should approach a common continuum limit value with different lattice artifacts. We can thus perform the continuum-chiral extrapolations for the Wilson data, for the mixed action, or for a combined data set, parameterizing the data with the same continuum limit mass-dependence $F^{\text{cont}}(\phi_2)$ but different cutoff effects (parameterized by different W, Z fit parameters for Wilson and mixed action data). We observe that by combining the Wilson and mixed action calculations, an increase in statistical precision and in the control of the continuum limit extrapolation of $\sqrt{8t_0}f_{\pi K}$ can be achieved. As a universality check, we performed the continuum limit extrapolation of the Wilson and mixed action determinations of $\sqrt{8t_0}f_{\pi K}$ using only symmetric point ensembles, without imposing a common value in the continuum. Since all these points have the same value of ϕ_2, they follow a line of constant physics as we approach towards the continuum limit. The extrapolation shown in Fig. 4.1 shows that both data sets agree perfectly well in the continuum. For this quantity, the mixed action data appears to receive milder discretization effects

Once the various models to extrapolate to the continuum and physical point have been explored, we use the model averaging technique introduced in Sec. 2.7 to assign a normalized weight to each model

$$W \propto \exp\left(-\frac{1}{2}\left(\chi^2 - 2\langle \chi^2 \rangle\right)\right), \tag{4.33}$$

that allows us to compute a weighted average for $\sqrt{t_0^{\mathrm{ph}}}$, as well as the associated systematic uncertainty

$$\left\langle \sqrt{t_0^{\mathrm{ph}}} \right\rangle = \sum_i \sqrt{t_0^{\mathrm{ph},(i)}} W^{(i)}, \tag{4.34}$$

$$\sigma_{\mathrm{syst}}^2 = \left\langle \sqrt{t_0^{\mathrm{ph}2}} \right\rangle - \left\langle \sqrt{t_0^{\mathrm{ph}}} \right\rangle^2. \tag{4.35}$$

In Figs. 4.3-4.5 we show the model average results for the Wilson unitary setup, for the mixed action and for the combined analysis. In Appendix K we show the numerical results of $\sqrt{t_0^{\mathrm{ph}}}$ for each model considered, together with their weights and p-values, for the Wilson, mixed action and combined analysis. In Fig. 4.2 we show the pion mass dependence of the continuum-chiral extrapolation for model $[SU(3)\chi PT][a^2]$ and the combined data set (no cuts), together with the lattice spacing dependence for the same model, projecting all points to the physical pion mass ϕ_2^{ph} using the fit result for the continuum dependence $F^{\mathrm{cont}}(\phi_2)$.

The results for $\sqrt{t_0^{\mathrm{ph}}}$ in physical units as computed from the model average for the different data sets, using $f_{\pi K}^{\mathrm{isoQCD}}$ as physical input, are

$$\sqrt{t_0^{\mathrm{ph}}} = 0.1433(9)_{\mathrm{stat}}(4)_{\mathrm{syst}} \text{ fm, Wilson,} \tag{4.36}$$

$$\sqrt{t_0^{\mathrm{ph}}} = 0.1442(10)_{\mathrm{stat}}(4)_{\mathrm{syst}} \text{ fm, Mixed action,} \tag{4.37}$$

$$\sqrt{t_0^{\mathrm{ph}}} = 0.1438(7)_{\mathrm{stat}}(4)_{\mathrm{syst}} \text{ fm, Combined.} \tag{4.38}$$

We show a comparison of these results with other determinations in the literature using $N_f = 2 + 1$ flavors of dynamical quarks in Fig. 4.7.

We tested the impact of varying over the choice of the coefficients c_β and c_{ϕ_2} in eq. (4.32) and found that the central values of the physical value of $\sqrt{t_0}$ in eqs. (4.36-4.38) move always well within 1σ, and not a big impact in the final uncertainty is found. More specifically, for the Combined analysis case if one removes altogether the $\beta = 3.40$ and $m_\pi = 420$ MeV ensembles from the analysis, the statistical and systematic uncertainties found are the same as in eq. (4.38). Additionally, one finds a statistical uncertainty of 0.0006 fm and a systematic uncertainty of 0.0003 fm for the Combined analysis result by setting $c_\beta = c_{\phi_2} = 0$ and including the $\beta = 3.40$ and $m_\pi = 420$ MeV ensembles into the analysis. Finally, we tested the impact of using [4] for the physical

input of m_π, m_K, f_π, f_K instead of using the input in [5] quoted in eqs. (4.3-4.5). This comparison is shown in Fig. 4.6.

The statistical uncertainty in eqs. (4.36-4.38) stems from the gauge noise of the CLS configurations, the uncertainties in the renormalization constants and improvement coefficients in Tables 2.1-2.2, and the physical inputs in eqs. (4.3-4.5). We show the splitting of these contributions for the combined analysis case in Table 4.1.

Contributions to total error squared of $\sqrt{t_0}$ [Combined]	
Model variation (systematic)	25.42%
Gauge ensembles	55.72%
Renormalization and improvement	0.82%
$\|V_{ud}\|$	0.01%
$\|V_{us}\|$	11.7%
QED corrections to f_π	0.32%
QED corrections to f_K	3%
Experimental input for f_π	0.01%
Experimental input for f_K	3%
IsoQCD pion and kaon meson masses	$< 0.01\%$

Table 4.1: Different contributions to total uncertainty for $\sqrt{t_0}$ for the combined analysis of both Wilson and mixed action lattice data in eq. (4.38).

4.3   DETERMINATION OF $\sqrt{t_0}$ AT THE SYMMETRIC POINT

The symmetric point is defined as the point in the quark mass plane at which the symmetric line defined by

$$m_{ud} \equiv m_l = m_s, \tag{4.39}$$

and the chiral trajectory in eq. (3.6) intersect. In terms of our usual quantities ϕ_2, ϕ_4, the symmetric point satisfies

$$\phi_2 = \frac{2}{3}\phi_4, \tag{4.40}$$

where ϕ_4 is given by its physical value after the iterative procedure to find t_0^{ph} and after mass shifting (see Sec. 3.4). In order to extract $t_0^{\text{sym}} = t_0(\phi_2^{\text{sym}}, \phi_4^{\text{ph}})$, following [123] we build the ratio

$$\frac{\sqrt{t_0/a^2}}{\sqrt{t_0^{\text{sym}}/a^2}}, \tag{4.41}$$

where $\sqrt{t_0/a^2}$ is the measurement of the gradient flow scale in each ensemble while $\sqrt{t_0^{\text{sym}}/a^2}$ is the corresponding lattice determination,
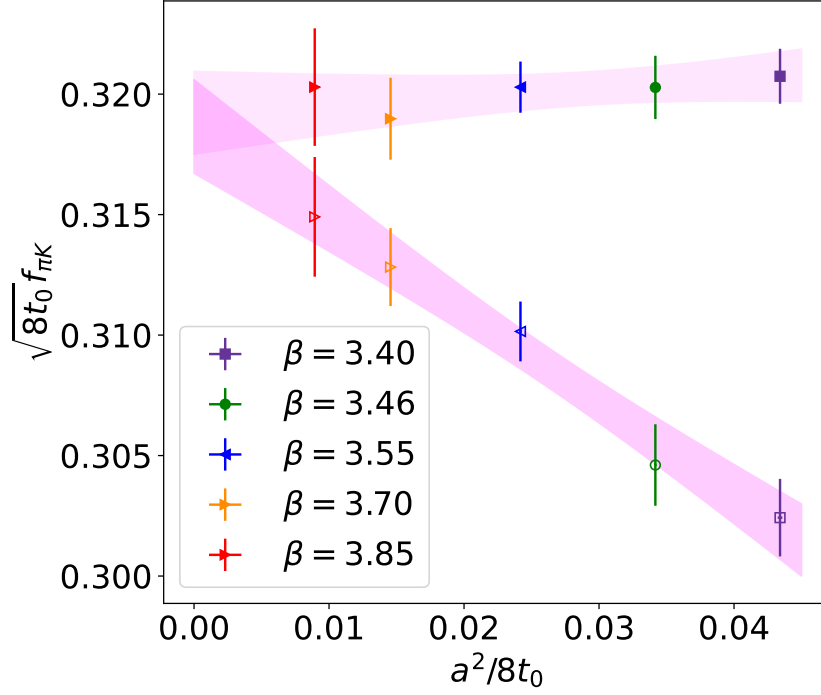
Figure 4.1: Continuum limit extrapolation of symmetric point ensembles for the Wilson unitary results (empty points) and for the mixed action results (filled points). In order to perform a universality check and verify that both regularizations share the same continuum limit, a common result at vanishing lattice spacing is not imposed. Cutoff effects are parameterized as pure $\mathcal{O}(a^2)$ artifacts independent for each regularization.
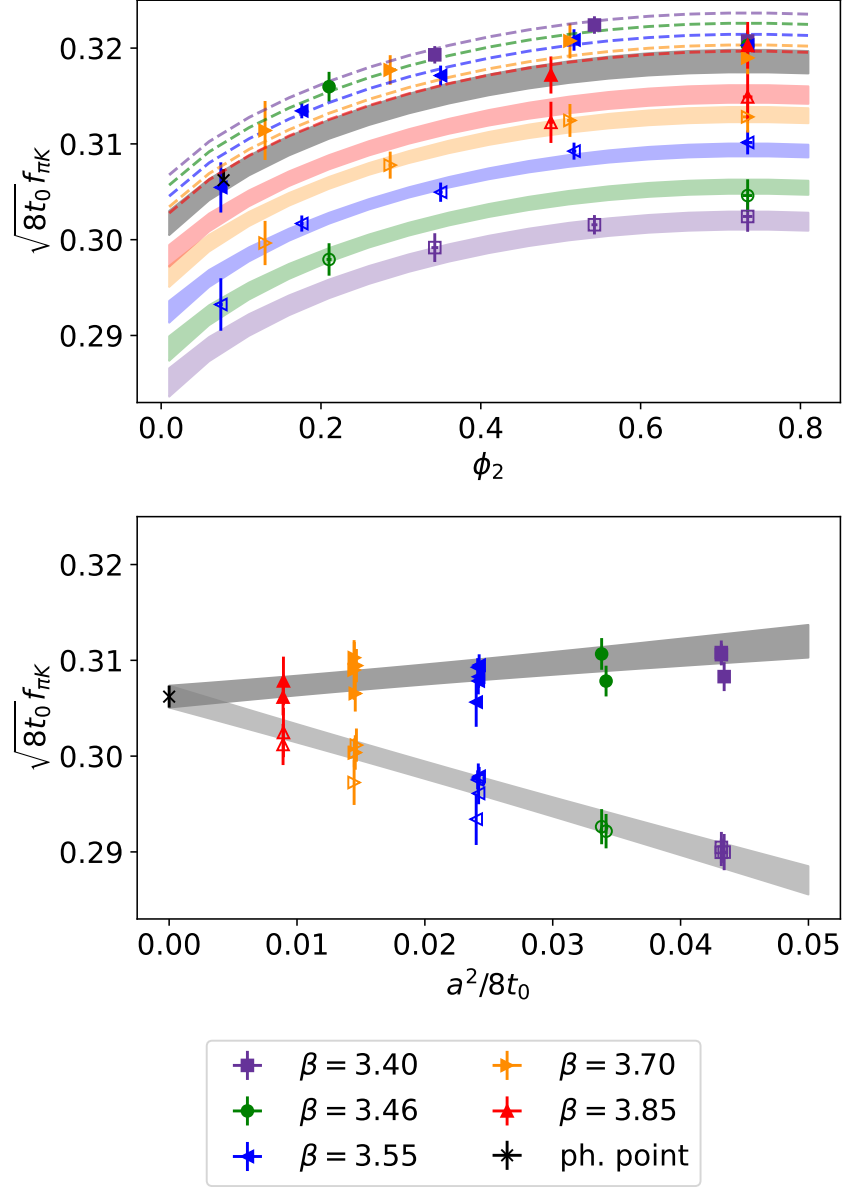
Figure 4.2: *Top*: Light quark mass-dependence of $\sqrt{8t_0}f_{\pi K}$ for the $SU(3)$ ChPT model with pure $\mathcal{O}(a^2)$ cutoff effects and absence of cuts in data, corresponding to the label: $[SU(3)\chi PT][a^2][-]$. We show the result of the combined fit of both Wilson (empty) and mixed action (filled) results. The colored bands represent the pion mass dependence for each lattice spacing for the Wilson results, while the dashed lines represent the dependence for the mixed action results. In the latter case we only plot the central value of the corresponding bands for visualization purposes. *Bottom*: the same model, with points projected to the physical pion mass ϕ_2^{ph} using the fit result for the continuum mass dependence $F(\phi_2)^{\mathrm{cont}}$. In this plot we show the lattice spacing dependence of our ensembles. The additional systematic effect terms in the χ^2 (see eq. (4.32)) were included. The p-value of this fit is 0.5532.

Figure 4.3: Model average results for the determination of $\sqrt{t_0}$ at the physical point based only on Wilson lattic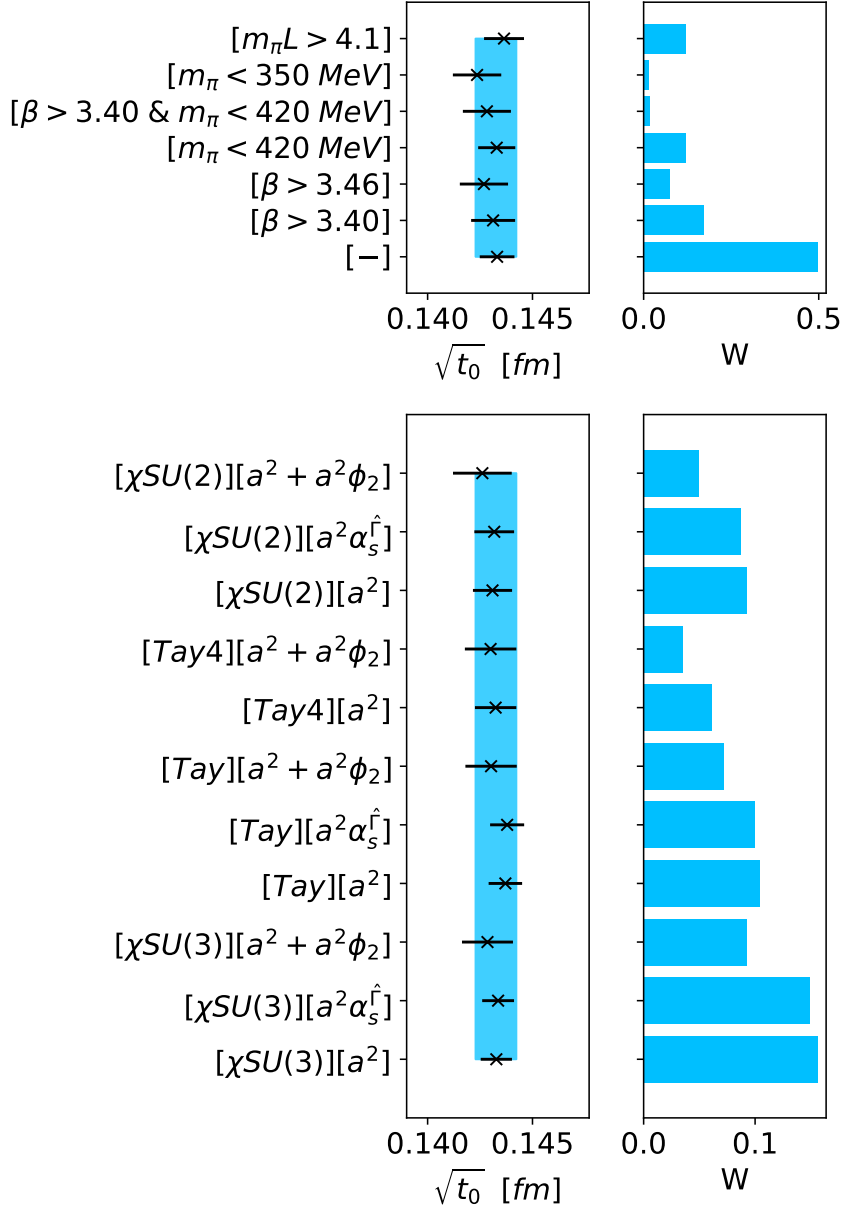e data and $f_{\pi K}$ as physical input. *Top*: model average over cuts in the data, the model weight defined in eq. (4.33). For each label of the cut performed to the data displayed in the panel, an average according to the model weights was taken over the various fit forms employed to perform the chiral-continuum extrapolation. The label "[-]" refers to the case in which no cuts are applied to the data. In all models the penalization of eq. (4.32) was included, so even in the "[-]" models points at $\beta = 3.40$ and $m_\pi = 420$ MeV are penalized in the fit. *Bottom*: model average over different fit forms employed in the chiral-continuum extrapolation. For each label of the fit form displayed in the panel, an average was taken over the various data cuts according to the model weights. The blue vertical band shows the result of the model average over the full set of considered models with systematic and statistical uncertainties added in quadrature. We provide Tables connecting each label to the corresponding fit models in Appendix K, as well as results of $\sqrt{t_0}$, model weight and p-value for each individual model.

Figure 4.4: Model average results for the determination of $\sqrt{t_0}$ at the physical point based only on mixed action lattice data and $f_{\pi K}$ as physical input. *Top*: model average over cuts in the data, the model weight defined in eq. (4.33). For each label of the cut performed to the data displayed in the panel, an average according to the model weights was taken over the various fit forms employed to perform the chiral-continuum extrapolation. The label "[-]" refers to the case in which no cuts are applied to the data. In all models the penalization of eq. (4.32) was included, so even in the "[-]" models points at $\beta = 3.40$ and $m_\pi = 420$ MeV are penalized in the fit. *Bottom*: model average over different fit forms employed in the chiral-continuum extrapolation. For each label of the fit form displayed in the panel, an average was taken over the various data cuts according to the model weights. The blue vertical band shows the result of the model average over the full set of considered models with systematic and statistical uncertainties added in quadrature. We provide Tables connecting each label to the corresponding fit models in Appendix K, as well as results of $\sqrt{t_0}$, model weight and p-value for each individual model.
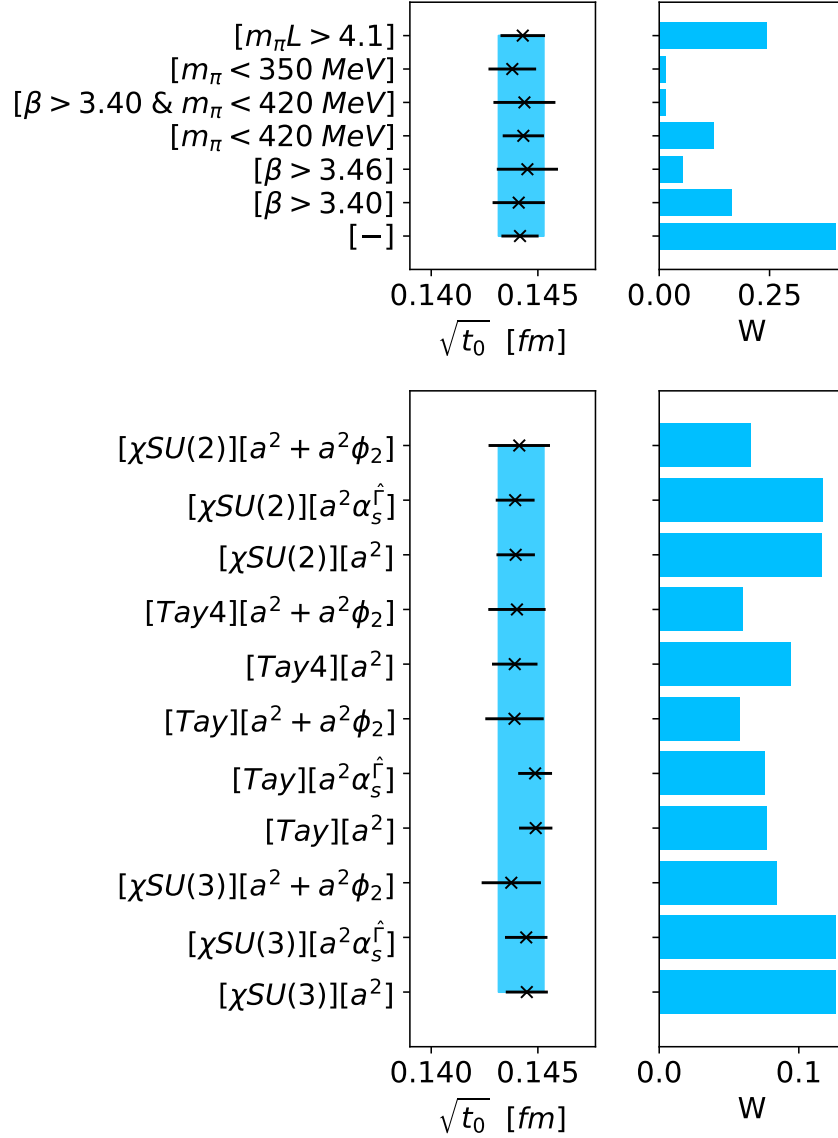
Figure 4.5: Model average results for the determination of $\sqrt{t_0}$ at the physical point based on the combination of Wilson and mixed action lattice data and $f_{\pi K}$ as physical input. *Top*: model average over cuts in the data, the model weight defined in eq. (4.33). For each label of the cut performed to the data displayed in the panel, an average according to the model weights was taken over the various fit forms employed to perform the chiral-continuum extrapolation. The label "[-]" refers to the case in which no cuts are applied to the data. In all models the penalization of eq. (4.32) was included, so even in the "[-]" models points at $\beta = 3.40$ and $m_\pi = 420$ MeV are penalized in the fit. *Bottom*: model average over different fit forms employed in the chiral-continuum extrapolation. For each label of the fit form displayed in the panel, an average was taken over the various data cuts according to the model weights. The blue vertical band shows the result of the model average over the full set of considered models with systematic and statistical uncertainties added in quadrature. We provide Tables connecting each label to the corresponding fit models in Appendix K, as well as results of $\sqrt{t_0}$, model weight and p-value for each individual model.
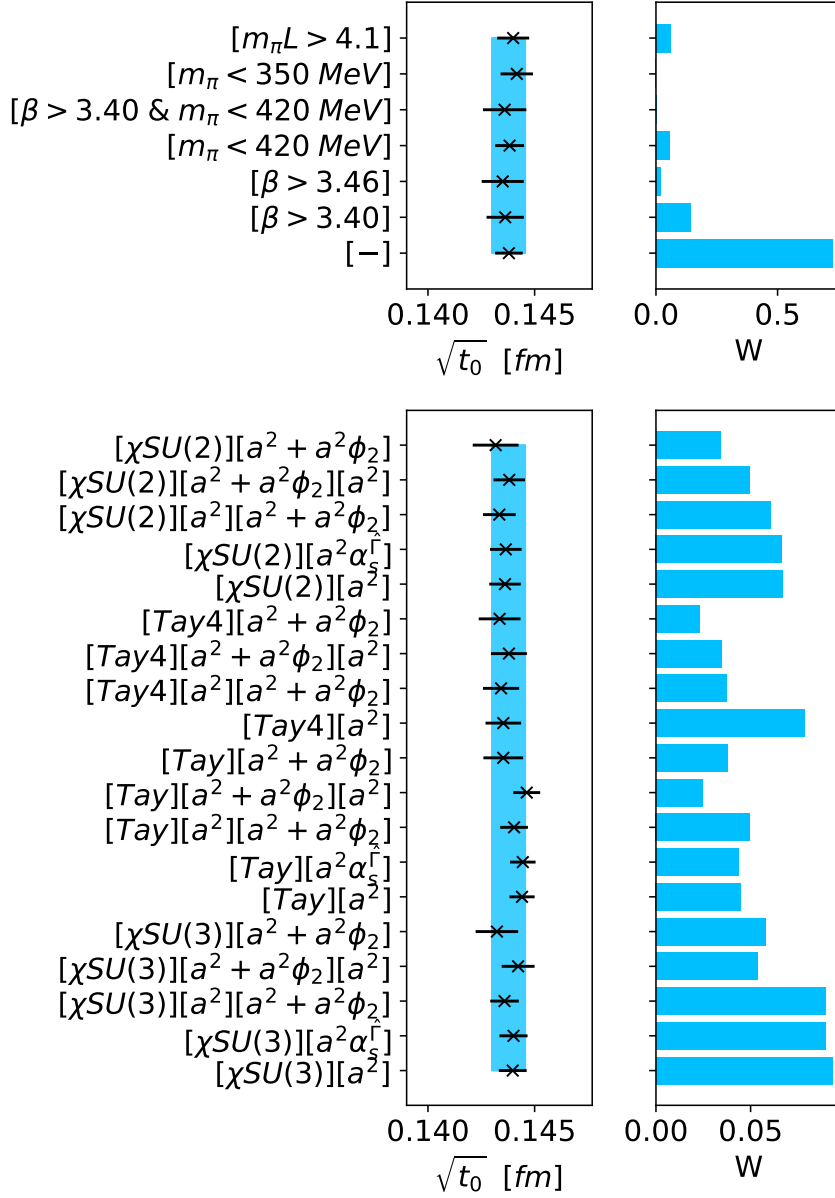
Figure 4.6: Comparison of our determination of $\sqrt{t_0}$ at the physical point with Bruno et al. '16 [29]. For our determination, in each label of the panel we show three variations, from top to bottom: using the complete set of ensembles listed in Table C.1 with physical input from [5] quoted in eqs. (4.3-4.5) and the systematic term in eq. (4.31) added when doing the model average (results quoted in eqs. (4.36)-4.38); using the complete set of ensembles but removing the systematic term in eq. (4.31) from the analysis and using physical input from [4]; and using the reduced set of ensembles listed in Table **??** without the systematic term in eq. (4.31) from the analysis and using physical input from [4]. The latest variation corresponds to an analysis following what was done in Bruno et al. [29], and we observe an upwards drift of the central values in $\sqrt{t_0}$ in our results, approaching the determination of $\sqrt{t_0}$ in [29]. The remaining difference between our determination and that of [29] might be explained by our use of the model average technique and by the higher amount of statistics available for ensembles D200 and J303 with respect to [29].
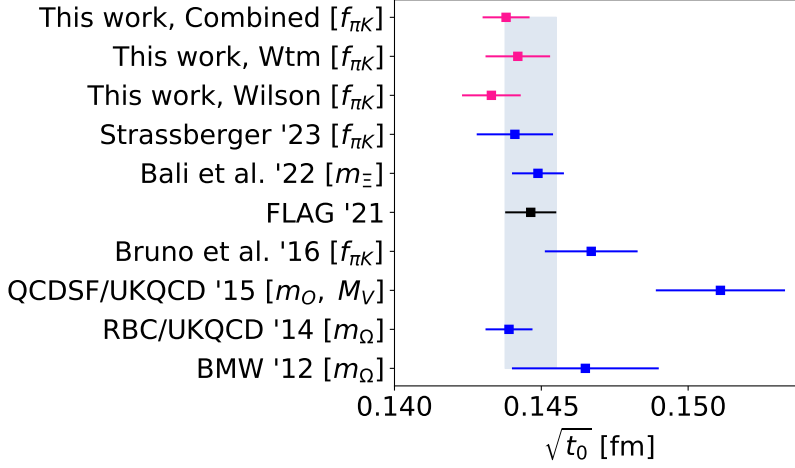
Figure 4.7: Comparison of our results in eqs. (4.36-4.38) with other determinations of $\sqrt{t_0}$ in the literature using $N_f = 2 + 1$ flavors of dynamical quarks. We specify between brackets the physical input used in each case to set the scale. BMW '12 refers to [23]. RBC/UKQCD '14 refers to [19] and QCDSF/UKQCD '15 to [21]. Bruno et al. '16 refers to [29], Bali et al. '22 to [10], Strassberger '23 to [123], and FLAG '21 to [5].

at the same value of the inverse coupling β, but using a symmetric point ensemble. Following [123] we fit this ratio to

$$F(\phi_2) = \sqrt{1 + p(\phi_2 - \phi_2^{\text{sym}})}. \tag{4.42}$$

We find this fit form to properly describe the lattice data. More specifically, no lattice artifacts are discerned from fits with $\mathcal{O}(a^2)$, $\mathcal{O}(a^2\phi_2)$ and/or $\mathcal{O}(a^2\alpha_S^{\Gamma})$ cutoff effects. The result of this fit is shown in Fig. 4.8. Once the data is fitted, we extract t_0^{sym} in physical units as

$$\sqrt{t_0^{\text{sym}}} = \frac{\sqrt{t_0^{\text{ph}}}}{F(\phi_2^{\text{ph}})}. \tag{4.43}$$

For t_0^{ph} and ϕ_2^{ph} we can use our determination for the Wilson, mixed action or combined data sets. The result for the scale at the symmetric point is, depending on this choice

$$\sqrt{t_0^{\text{sym}}} = 0.1429(9)_{\text{stat}}(4)_{\text{syst}} \text{ fm, Wilson,} \tag{4.44}$$

$$\sqrt{t_0^{\text{sym}}} = 0.1439(10)_{\text{stat}}(4)_{\text{syst}} \text{ fm, Mixed action,} \tag{4.45}$$

$$\sqrt{t_0^{\text{sym}}} = 0.1435(7)_{\text{stat}}(4)_{\text{syst}} \text{ fm, Combined.} \tag{4.46}$$
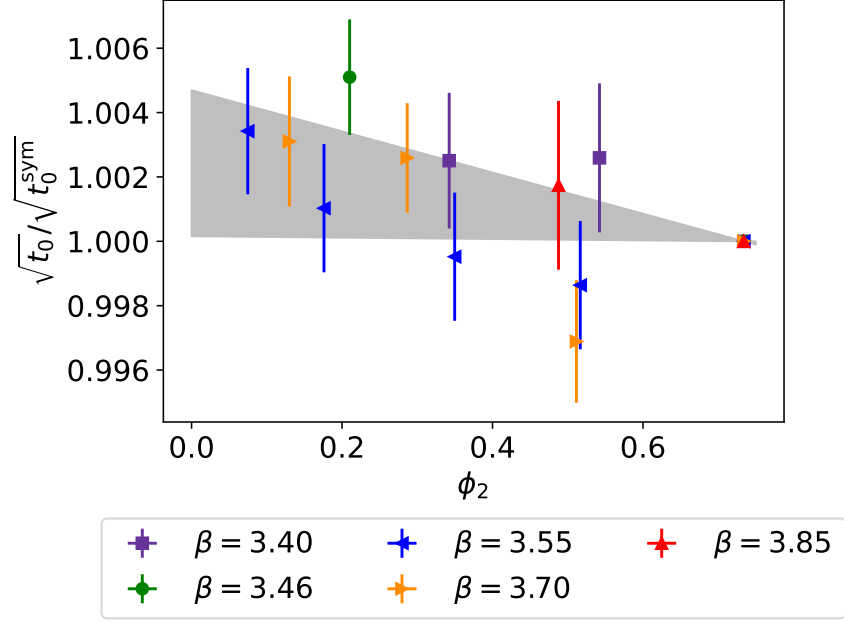
Figure 4.8: Fit to eq. (4.42) in order to extract t_0 at the symmetric point.

4.4   DETERMINATION OF THE LATTICE SPACING FOR CLS ENSEMBLES

Just as in the previous section, we can use the fit to $\frac{\sqrt{t_0/a^2}}{\sqrt{t_0^{\text{sym}}/a^2}}$ to compute

$$\left(\sqrt{\frac{t_0}{a^2}}\right)^{\text{ph}} = \sqrt{\frac{t_0^{\text{sym}}}{a^2}} F(\phi_2^{\text{ph}}). \tag{4.47}$$

Then, the lattice spacing is extracted as

$$a = \frac{\sqrt{t_0^{\text{ph}}}}{\left(\sqrt{\frac{t_0}{a^2}}\right)^{\text{ph}}}. \tag{4.48}$$

For ϕ_2^{ph} we can either use our determinations of t_0^{ph} for the Wilson, mixed action or combined data sets. Results for the lattice spacing are shown in Table 4.2.

β	a [fm] Wilson	a [fm] mixed action	a [fm] combined
3.40	$0.0842(6)_{\text{stat}}(2)_{\text{syst}}$	$0.0848(6)_{\text{stat}}(3)_{\text{syst}}$	$0.0845(5)_{\text{stat}}(2)_{\text{syst}}$
3.46	$0.0747(5)_{\text{stat}}(2)_{\text{syst}}$	$0.0752(5)_{\text{stat}}(2)_{\text{syst}}$	$0.0750(4)_{\text{stat}}(2)_{\text{syst}}$
3.55	$0.0629(4)_{\text{stat}}(2)_{\text{syst}}$	$0.0633(4)_{\text{stat}}(2)_{\text{syst}}$	$0.0631(3)_{\text{stat}}(2)_{\text{syst}}$
3.70	$0.0488(3)_{\text{stat}}(1)_{\text{syst}}$	$0.0491(3)_{\text{stat}}(2)_{\text{syst}}$	$0.0490(3)_{\text{stat}}(1)_{\text{syst}}$

| 3.85 | $0.0382(2)_{\text{stat}}(1)_{\text{syst}}$ | $0.0385(3)_{\text{stat}}(1)_{\text{syst}}$ | $0.0384(2)_{\text{stat}}(1)_{\text{syst}}$ |

Table 4.2: Values of the lattice spacing a in physical units extracted from the determination of the gradient flow scale t_0 with the Wilson, mixed action and combined analysis. The lattice spacing is extracted from measures of both t_0 at the physical and symmetric points using eq. (4.48).

4.5 DETERMINATION OF t_0^*

Yet another point in the (ϕ_2, ϕ_4) plane of interest corresponds to the reference point in [29]

$$\phi_4 = 1.11, \quad \phi_2 = \frac{2}{3}\phi_4 \equiv \phi_2^{\text{sym}}. \tag{4.49}$$

The scale t_0 evaluated at this point is

$$t_0^* = t_0 \left(\phi_2^{\text{sym}}, \ \phi_4 = 1.11\right), \tag{4.50}$$

and its ratio to $\sqrt{t_0^{\text{ph}}}$ enters in the computation of the strong coupling in [48]. To compute t_0^*, we repeat the analysis by mass shifting our ensembles to the value $\phi_4 = 1.11$ without error and compute the gradient flow scale at the symmetric point as explained in the Sec. 4.4.

The values we find for $\sqrt{t_0^*}$ in physical units for the Wilson, mixed action and combined cases are

$$\sqrt{t_0^*} = 0.1432(9)_{\text{stat}}(4)_{\text{syst}} \text{ fm, Wilson,} \tag{4.51}$$

$$\sqrt{t_0^*} = 0.1439(9)_{\text{stat}}(4)_{\text{syst}} \text{ fm, Mixed action,} \tag{4.52}$$

$$\sqrt{t_0^*} = 0.1436(7)_{\text{stat}}(4)_{\text{syst}} \text{ fm, Combined.} \tag{4.53}$$

IMPACT OF THE SCALE SETTING IN HADRONIC COMPUTATIONS

5.1 INTRODUCTION

In this Chapter we discuss hadronic computations involving the charm quark following our work [34], with special emphasis on the impact on these results of the scale t_0 we obtained in Chapter 4. In particular, we will see that with the high precision result we obtained in eq. (4.38) we can quote results for the renormalized charm quark mass and $D_{(s)}$ charmed mesons decay constants where the scale t_0 is not the dominant source of uncertainty.

For the extraction of charm observables we rely entirely on the mixed action setup, exploiting automatic $\mathcal{O}(a)$ improvement for valence observables, ensured by our mixed action setup once the matching of the sea and valence sectors, in addition to the tune to maximal twist explained in Sec. 3.5 are performed. This helps in keeping under control large discretization effects associated to the heavy mass of the charm quark.

In Sec. 5.2 we discuss the details of our strategy to match the charm quark mass to its physical value. In Sec. 5.3 we discuss chiral-continuum extrapolations of the renormalized charm quark mass and present our results for this quantity at the physical point after performing a model average of the different possible extrapolations. In Sec. 5.4 we present our results for the charmed mesons $D_{(s)}$ decay constants, showing the contribution to the final uncertainty coming from the determination of the scale t_0. For a complete discussion of these results we refer to our work [34].

In addition to these charmed mesons computations, in Appendix **??** we show some preliminary analysis of the light and strange quark masses.

5.2 MATCHING OF THE CHARM QUARK MASS

In Sec. 3 we performed the matching of the sea and valence sectors of our mixed action for the light and strange flavors, in addition to tuning to maximal twist. Once the valence parameters were determined to ensure these conditions, an independent set of computations of heavy propagators was performed for the study of charm physics. Heavy propagators are computed at three different values of the twisted mass $\mu_c^{(i)}$ around the physical charm region for the main set of ensembles, while for a subset of them only two masses have been used, so that

observables are interpolated at the physical value of the charm quark mass. In order to fix the charm quark mass to its physical value, we use different combinations of mesons masses m_H matched to their physical values. Since the charm is partially quenched, this matching procedure involves observables with only valence charm quark propagators.

We study two different charm scale settings based on two choices of $m_H^{(i)}$, $i = 1, 2$, and will often be expressed in units of $\sqrt{8t_0}$ as $\phi_H^{(i)} = \sqrt{8t_0} m_H^{(i)}$.

The first possibility we explore, corresponding to $\phi_H^{(1)}$, consists in using the flavor average meson mass combination

$$m_H^{(1)} = m_{\overline{H}} \equiv \frac{2}{3} m_H + \frac{1}{3} m_{H_s}, \tag{5.1}$$

built from heavy-light H and heavy-strange H_s pseudoscalar meson masses with heavy-quark masses in neighbourhood of the charm. Since we mass shifted[1] the considered CLS ensembles in order to impose a constant value of ϕ_4 (see eq. (3.9)), we expect the flavor average combination $\phi_H^{(1)}$ to remain fairly constant along the chiral trajectory. The physical value of $m_H^{(1),\text{ph}}$ is obtained by setting $m_{H_{(s)}}$ to the following prescription for the isoQCD values of $D_{(s)}$ meson masses,

$$m_D^{\text{isoQCD}} = 1867.1(2.6) \text{ MeV}, \qquad m_{D_s}^{\text{isoQCD}} = 1967.1(1.3) \text{ MeV}. \tag{5.2}$$

The uncertainties in these isoQCD values are chosen to cover the deviation with respect to the experimental values [131] of the $D^{\pm}$ and $D_s^{\pm}$ meson masses, $m_{D^{\pm}}^{\text{exp}} = 1869.66(5)$ MeV and $m_{D_s^{\pm}}^{\text{exp}} = 1968.35(7)$ MeV, respectively. We observe that the larger uncertainty in the isoQCD inputs of the D and D_s meson masses in eq. (5.2) — as compared to the corresponding experimental values — does not induce a significant increase in the uncertainties of our target results. The input values in eq. (5.2) lead to the following flavor averaged meson mass,

$$m_H^{(1),\text{ph}} = m_{\overline{D}} = 1900.4(1.8) \text{ MeV}. \tag{5.3}$$

The second strategy, corresponding to $\phi_H^{(2)}$, is to consider the mass-degenerate pseudoscalar meson mass $m_{\eta_h}^{\text{conn}}$ extracted from the quark-connected two-point correlation function made of heavy quark propagators with a mass in the neighbourhood of the charm mass,

$$m_H^{(2)} = m_{\eta_h}^{\text{conn}}. \tag{5.4}$$

The physical value for this mass, $m_H^{(2),\text{ph}}$, is set from the experimental value of the η_c meson mass [131], $m_{\eta_c}^{\text{exp}} = 2983.9(4)$ MeV, from which

---

1 In the case of charmed observables like the ones in this Chapter, the mass shift was performed in a similar manner to what is discussed in Sec. 3.4, but this time using the dedicated measurements of the mass derivatives for each ensemble, instead of parametrizing them as functions of ϕ_2 and the lattice spacing.

a correction of about 6 MeV, with 100% error, is subtracted to account for the absence of quark-disconnected diagrams and QED effects [43, 44, 54, 57, 71]. Specifically, we employ,

$$m_H^{(2),\text{ph}} = m_{\eta_c}^{\text{conn}} = 2978(6)\text{ MeV}. \tag{5.5}$$

One potential advantage of this choice of matching observable is that the overall precision of the η_c^{conn} meson mass is substantially better than the one for heavy-light meson masses, as it does not suffer from the increase in noise-to-signal ratio with Euclidean time.

Any of these matching conditions can in principle be imposed ensemble by ensemble, even away from the physical point. However, by doing so we would as a result build in the charm quark mass a dependence on the value of the reference scale t_0^{ph}, as well as $\mathcal{O}(a^2)$ effects coming from the specific choice of m_H. To avoid this, we have opted instead for setting the physical charm quark mass jointly with the chiral-continuum extrapolation, in a similar way as the one we employ to hit the physical point in the light and strange sector. What this means in practice is that the charm quark mass dependence of any given observable is parameterized as $\mathcal{O}(a, \phi_2, \phi_H^{(i)})$, and we perform a global fit to obtain its physical value $\mathcal{O}(0, \phi_2^{\text{ph}}, \phi_H^{(i),\text{ph}})$. This will be the procedure applied below in the determination of the physical value of the charm quark mass and of the decay constants f_D and f_{D_s}.

5.3 DETERMINATION OF THE CHARM QUARK MASS

5.3.1 *Renormalised charm quark masses*

As discussed in Sec. 1.3.3, in the Wilson tm regularization, renormalized quark masses can be easily retrieved from bare Lagrangian twisted masses. In our mixed-action setup the resulting $\mathcal{O}(a)$ improved expression for the renormalised charm mass μ_c^R reads

$$\mu_c^R = Z_P^{-1}(g_0^2, a\mu_{\text{ren}}) \left[1 + a\bar{b}_\mu \text{tr}\left(M_q^{(s)}\right)\right] \mu_c, \tag{5.6}$$

where Z_P is the renormalisation constant for the non-singlet pseudoscalar density at some renormalisation scale μ_{ren} as discussed in Sec. 1.3.3. The improvement coefficient $\bar{b}_\mu$ is suppressed by the trace of the sea quark mass matrix $\text{tr}\left(M_q^{(s)}\right)$ where only light quarks enter, and therefore it can be neglected because its natural value is well below the precision of the computation. Thus $\mathcal{O}(a)$ improved renormalised quark masses can be obtained by just applying the renormalisation constants to the twisted masses μ_i in the Lagrangian.

The values of Z_P are listed in Table 2.1 and were computed at a fixed renormalization scale $\mu_{\text{had}} = 233(8)$ MeV. They allow to obtain renormalised quark masses for each of our ensembles, that can then be used

to determine the value of the charm quark mass in the continuum and at physical kinematics. Contact with other renormalisation schemes can then be made by computing the renormalisation group invariant (RGI) quark mass M_c^{RGI}, using the continuum (flavor-independent) ratio also computed in [35]

$$\frac{M}{\overline{m}(\mu_{\mathrm{had}})} = 0.9148(88) \,. \tag{5.7}$$

Values of renormalised masses in another renormalization scheme can then be obtained by using the perturbative value of $\frac{\overline{m}(\mu)}{M}$ at any convenient scale μ.

5.3.2 *Charm quark mass chiral-continuum fits*

Having determined the renormalised charm quark masses in the Schrödinger Functional scheme at the hadronic renormalisation scale μ_{had}, μ_c^{R}, for all the ensembles listed in Table C.1, we can perform the chiral-continuum fits to obtain results in the continuum limit and at the physical point. The matching procedure of the light and strange sectors is already devised so that the physical value of the kaon mass is recovered at $\phi_2 = \phi_2^{\mathrm{ph}}$, where the physical value of ϕ_2 is computed with the isoQCD values of the pion mass quoted in [5] (see eqs. (4.3)), and the physical scale t_0^{ph} is the one determined in eq. (4.38). The charm scale is matched through the two different prescriptions described in Sec. 5.2. All quantities entering the fit are made dimensionless through the appropriate power of the factor $\sqrt{8t_0}$, and physical units for the final result are restored by using our value for t_0^{ph}.

We parameterise the continuum dependence of the renormalised charm quark mass on ϕ_2 and any of the $\phi_H^{(i)}$ with the functional form

$$\sqrt{8t_0}\,\mu_c^{\mathrm{R}}(a = 0, \phi_2, \phi_H) = p_0 + p_1\phi_2 + p_2\phi_H \,. \tag{5.8}$$

Based on the heavy quark effective theory expansion [64] at lowest order, we expect a linear dependence of the charmed meson masses as a function of the the charm quark mass, hence the latter term in the ansatz. This assumption is supported by our data that show indeed a linear behaviour in the charmed meson masses, as illustrated in Figure 5.3. Note that this form is used only to describe the dependence within a short interval in mass values, and interpolate the charm scale from points close by. When considering the pion dependence of the charm quark mass, we assume that the leading order contributions exhibit a linear behaviour in ϕ_2. With the set of ensembles employed in this work we do not observe any deviations from the leading order term in the pion mass dependence.

Regarding the lattice spacing dependence of the charm quark mass, we assume the leading cutoff effects to be $\mathcal{O}(a^2)$, as discussed above.

Corrections of odd order in a are generically expected to be highly suppressed at maximal twist, by way of the extension of the argument for automatic $\mathcal{O}(a)$ improvement; we thus include a^4 terms to account for deviations from linear behaviour in a^2. Finally, we allow for terms proportional to m_π^2 and to various powers of the charm mass. The generic ansatz to parameterise lattice spacing dependence thus take the following form

$$c_{\mu_c}(a, \phi_2, \phi_H) = \frac{a^2}{8t_0}\left(c_1 + c_2\phi_2 + c_3\phi_H^2\right) + \frac{a^4}{(8t_0)^2}\left(c_4 + c_5\phi_H^2 + c_6\phi_H^4\right).$$
(5.9)

In order to estimate the systematic effects arising from the model variation, we consider all the possible combinations where some of the c_i coefficients vanish, save for c_1 which is always kept. Furthermore, following [72], we allow for cutoff effects to enter either linearly or non-linearly, viz.,

$$\sqrt{8t_0}\mu_c^{R,\text{linear}}(a, \phi_2, \phi_H) = \sqrt{8t_0}\mu_c^{R,\text{cont}} + c_{\mu_c}(a, \phi_2, \phi_H),$$
(5.10)

$$\sqrt{8t_0}\mu_c^{R,\text{non-lin}}(a, \phi_2, \phi_H) = \sqrt{8t_0}\mu_c^{R,\text{cont}} \times \left(1 + c_{\mu_c}(a, \phi_2, \phi_H)\right),$$

where $\sqrt{8t_0}\mu_c^{R,\text{cont}} = \sqrt{8t_0}\,\mu_c^{R}(a = 0, \phi_2, \phi_H)$. We thus end up with a total of 64 functional forms for each of the two charm matching conditions, i.e., a total of 128 models.

As in the analysis of the scale setting in Chapter 4, we perform a model average as introduced in Sec. 2.7 in order to study all the different choices for the chiral-continuum limit extrapolations, assigning to each fit a model weight through the Takeuchi's Information Criterion (TIC), obtaining thus a final weighted average result, as well as a systematic uncertainty coming from the model variation. For a complete discussion of the models considered and their relative weight we refer to our work [34].

In Table 5.1 we report the results for μ_c^R in units of $\sqrt{8t_0}$ obtained with each of the two matching conditions independently, as well as for the combined model average.

	$\phi_H^{(1)}$	$\phi_H^{(2)}$	combined
$\sqrt{8t_0}\mu_c^R$	3.354(28)(6)	3.363(27)(6)	3.361(26)(7)

Table 5.1: Results of the model average for the renormalised charm quark mass in units of $\sqrt{8t_0}$ based on the two charm quark mass matching conditions — $\phi_H^{(1)}$ denotes the flavor-averaged matching condition in eq. (5.1) and $\phi_H^{(2)}$ the η_h^{conn} matching prescription in eq. (5.4). The last column reports the combined result from these two matching procedures according to our model average prescription. The first error is statistical, while the second is the systematic uncertainty arising from the model variation.

Figure 5.1 illustrates typical fits for each of the matching conditions, chosen among those with higher weights according to the TIC prescription. The plot shows the continuum limit behaviour of the charm quark mass in units of $\sqrt{8t_0}$. Results coming from the two matching strategies perfectly agree in the continuum, in spite of displaying a qualitatively different structure in cutoff effects. We observe a scaling of the charm quark mass in reasonable agreement with the $\mathcal{O}(a^2)$ leading order, confirming the automatic $\mathcal{O}(a)$ improvement of our setup; nevertheless, we notice that given the current statistical accuracy, fits with $\mathcal{O}(a^4)$ terms are the preferred ones from the model average, since they allow to properly describe the curvature in our data. Note also the overall small size of scaling violations, which are at the few percent level. Finally, Figure 5.2 shows the pion mass dependence of the charm quark mass, while Figure 5.3 shows the heavy mass dependence of the charm quark mass. As expected, we observe a mild dependence of the charm mass on the light quark masses.

5.3.3 *Results for the charm quark mass*

The renormalised charm quark mass μ_c^R can be obtained once we combine the results collected in Table 5.1 with our determination of $\sqrt{t_0^{\text{ph}}}$ in eq. (4.38). As discussed at the beginning of this section, the knowledge of the renormalisation group running factors allows to quote results for the RGI and $\overline{\text{MS}}$ values of the charm quark mass.

After combining the results from our 128 fitting models through the model average procedure, and using the running factor in eq. (5.7), we quote for the three-flavor theory the value for the RGI quark mass

$$M_c^{\text{RGI}}(N_f = 3) = 1.485(8)_{\text{stat}}(3)_{\text{syst}}(14)_{\text{RGI}} \text{ GeV}, \qquad (5.11)$$

where the first error is statistical, including the uncertainty on t_0^{ph}, the second accounts for the systematic uncertainty, derived from the model average, and the third is the error contribution from the RGI running factor in eq. (5.7).

Figure 5.4 illustrates the relative contribution of various sources of error to the uncertainty of our determination of M_c^{RGI}. The dominant source of error comes from the renormalisation group running of
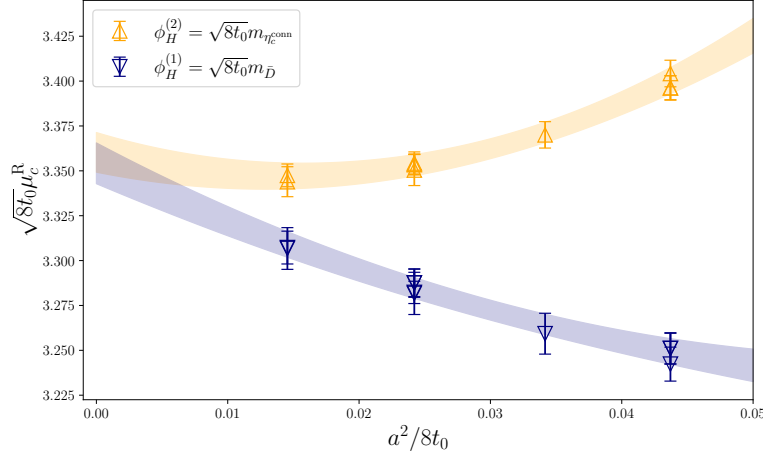
Figure 5.1: Comparison of the continuum limit approach for the two charm matching prescriptions. Shown are two of the fits with highest weights from the TIC, projected onto the lattice spacing dimension. In yellow we show results for the η_h^{conn} matching condition, while the blue points illustrate the flavor-averaged matching. Each datapoint in this plot is projected to the physical pion mass and the physical charm quark mass, in order to properly visualise the lattice spacing dependence.
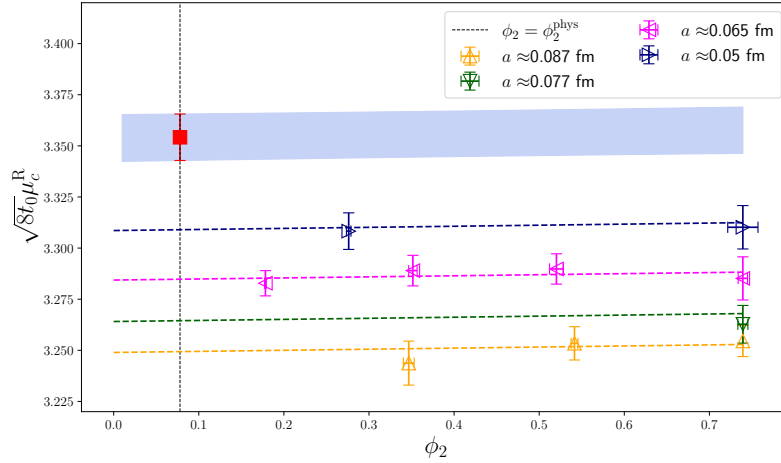
Figure 5.2: Pion mass dependence of the charm quark mass for one of the best fits according to the TIC criteria. Results are shown for the flavor-averaged matching condition. Each point corresponds to the value for a given ensemble, projected to the physical charm quark mass. The dashed lines represent the chiral trajectories at finite lattice spacing, while the blue shaded band is a projection to the continuum limit. The red point shows our final result extrapolated at the physical point in the continuum.
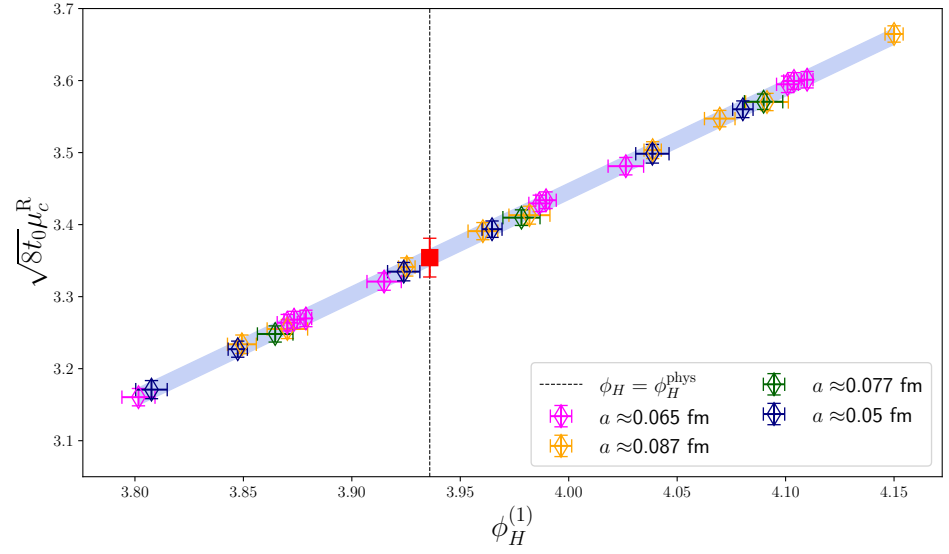
Figure 5.3: Heavy mass dependence of the renormalised charm quark mass μ_c^R in units of $\sqrt{8t_0}$ for one of the fits with larger weights according to the TIC criteria. Results shown for the flavor-averaged matching condition $\phi_H^{(1)} = \sqrt{8t_0}m_{\overline{H}}$. Dependencies other than $\phi_H^{(i)}$ in the chiral-continuum extrapolation have been projected to the physical point. The red square symbols indicate the continuum results at the physical value ϕ_H^{ph}. We observe a linear dependence of the charm quark mass on $\phi_H^{(1)} = \sqrt{8t_0}m_{\overline{H}}$.

$$M_c^{\mathrm{RGI}}(N_f = 3)$$

Figure 5.4: Relative contributions to the total variance of our final result for M_c^{RGI}. The dominant piece comes from the error in the non-perturbative determination of the renormalisation group running factor to the RGI mass quoted in eq. (5.7). The label statistical plus χ-continuum limit stands for the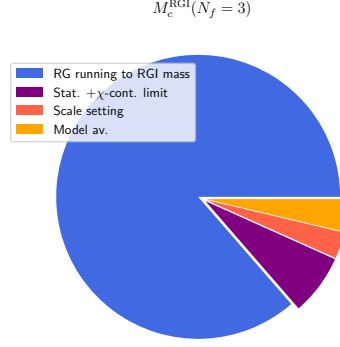 error arising from the statistical accuracy of our data and the chiral-continuum extrapolation, while the scale setting piece comes from the physical value of the gradient flow scale t_0^{ph}. Finally, the model average piece illustrates the systematic error arising from the set of models considered in this work.

eq. (5.7), while the second most relevant contribution arises from the statistical error of the correlation functions computed in each ensemble. The error coming from the uncertainty on t_0^{ph} based on our scale setting procedure, as well as the systematic error from the model average are subleading contributions. We therefore expect that the inclusion in this charm quark mass analysis of further ensembles or increased statistics will only have a significant impact if combined with improved determinations of the RGI running factor and the scale setting procedure.

In order to quote results in the $\overline{\mathrm{MS}}$ scheme, we use five-loop perturbation theory for the quark mass anomalous dimension [7, 9, 93] and the beta function [8, 75, 92]. The matching between the $N_f = 3$ and $N_f = 4$ theories uses the four-loop decoupling effects [83] incorporated into the RunDec package [38, 74, 118]. Renormalisation group equations are solved using as input the value $\Lambda_{\overline{\mathrm{MS}}}^{(3)} = 341(12)$ MeV from [28]. The correlation arising from the fact that a common subset of gauge field configuration ensembles were employed in the computation of $\Lambda_{\overline{\mathrm{MS}}}^{(3)}$ and the non-perturbative running factor in eq. (5.7) is
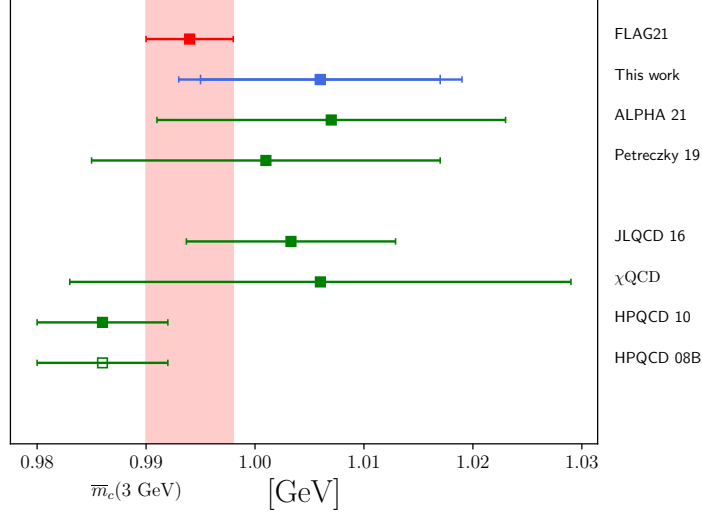
Figure 5.5: Comparison of our charm quark mass determinations in the $\overline{\text{MS}}$ scheme with the FLAG average [5] and the results from other lattice QCD calculations based on $N_f = 2 + 1$ dynamical simulations. In our results, shown in blue, we indicate both the total uncertainty and the error when excluding the uncertainty arising from $\Lambda_{\overline{\text{MS}}}^{(3)}$. *Top*: comparison for the $\overline{m}_c(\mu = 3\text{ GeV}, N_f = 4)$. *Bottom*: comparison for $\overline{m}_c(\mu = \overline{m}_c, N_f = 4)$. Starting from the bottom, results are taken from: PDG [131], HPQCD 08B [2], HPQCD 10 [99], χQCD [132], JLQCD 16 [105], Maezawa 16 [96], Petreczky 19 [113], ALPHA 21 [72].

taken into account. We thus arrive to the following results for the RGI and $\overline{\text{MS}}$-scheme charm quark masses in the 4-flavor theory,

$$M_c^{\text{RGI}}(N_f = 4) = 1.546(8)(3)(14)(4)_{\Lambda}(3)_{\text{trunc.}} \text{ GeV}, \qquad (5.12)$$

$$\overline{m}_c(\mu = 3\text{ GeV}, N_f = 4) = 1.006(5)(2)(9)(6)_{\Lambda}(3)_{\text{trunc.}} \text{ GeV}, \qquad (5.13)$$

where the first and second errors arise from the statistical and systematic errors, respectively, in the value of $M_c^{\text{RGI}}(N_f = 3)$ in eq. (5.11), the third error is due to the non-perturbative running factor in eq. (5.7), the fourth error is related to the uncertainty in $\Lambda_{\overline{\text{MS}}}^{(3)}$, and the fifth error is an estimate of the truncation uncertainty from the deviation between the 5-loop and 4-loop results.

In Figure 5.5 we compare our determinations of the charm quark mass in the $\overline{\text{MS}}$ scheme with the results from other lattice QCD calculations also based on $N_f = 2 + 1$ dynamical simulations and with the corresponding FLAG average [5]. We observe in particular a good agreement with the results from [72] which are also based on CLS ensembles but employ Wilson fermions in the valence sector.

For the determination of the decay constants of the charmed mesons $D_{(s)}$ we employ a similar methodology to the one for the renormalized charm quark mass. We match the charm quark mass to its physical value following the same prescription as in Sec. 5.2, and we explore different ways of performing the chiral-continuum limit extrapolations in order to obtain $f_{D_{(s)}}$ at the physical point. For a detailed discussion we refer to our work [34], here we will only show our main results emphasizing the impact on these of our determination of the scale t_0 in Chapter 4.

5.4.1   *Computation of decay constants*

The quantity we employ to extract $f_{D_{(s)}}$ in the continuum and at physical quark masses is

$$\Phi_{D_{(s)}} = (8t_0)^{3/4} f_{D_{(s)}} \sqrt{m_{D_{(s)}}}, \tag{5.14}$$

for which a Heavy Quark Effective Theory (HQET) scaling law in powers of the inverse heavy quark mass exists. The general continuum heavy and light quark mass dependence can be expressed as the product of the individual contributions to arrive at the generic expression

$$\Phi_{D_{(s)}} = \Phi_\chi \left[1 + \delta\Phi_{\chi\mathrm{PT}}^{D_{(s)}}\right] \left[1 + \delta\Phi_a^{D_{(s)}}\right]. \tag{5.15}$$

Here Φ_χ governs the heavy-quark mass dependence while $\delta\Phi_{\chi\mathrm{PT}}^{D_{(s)}}$ controls the light quark behaviour as approaching the physical point. Finally the lattice spacing dependence describing cut-off effects is regulated by $\delta\Phi_a^{D_{(s)}}$.

For an analysis of each of the terms appearing in eq. (5.15) we refer to our work [34]. Here we only comment that for Φ_χ we use expressions motivated by HQET, while the light-quark dependence in $\delta\Phi_{\chi\mathrm{PT}}^{D_{(s)}}$ admits an expression in Heavy Meson χPT (HMχPT). For cutoff effects, we consider $\mathcal{O}(a^2)$, $\mathcal{O}(a^2\phi_2)$ and $\mathcal{O}(a^2\phi_H)$ terms.

Similarly to the case of the charm quark mass, we consider several specific forms of the fit ansatz, by setting some combination of fit parameters to zero. We furthermore again match the charm scale using the two different procedures described in Sec. 5.2. The result is a total of 57 different models for each matching condition, and we use our TIC criterion to extract a systematic uncertainty associated to the variation within the full set of fits.

In Table 5.2 we show our determinations of Φ_D and Φ_{D_s} for each of the two procedures to match the charm scale, as well as the result from
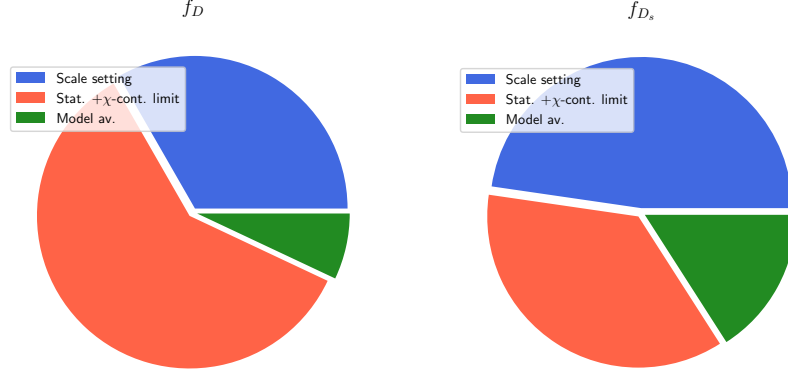
Figure 5.6: Relative contributions to the total error of our determinations of f_D (*left*) and f_{D_s} (*right*). The label statistical plus χ-continuum limit represents the error arising from the statistical accuracy of our data and the chiral-continuum extrapolations. The scale setting label denotes the error coming from the physical value t_0^{ph} as determined in Chapter 4, while the model average represents the systematic error arising from the model variation according to the TIC procedure.

their combination. Using this combination we arrive at the following results for the the $D_{(s)}$ meson decay constants,

	$\phi_H^{(1)}$	$\phi_H^{(2)}$	combined
Φ_D	0.8624(78)(7)	0.8583(75)(8)	0.8606(76)(21)
Φ_{D_s}	1.0352(61)(9)	1.0295(60)(11)	1.0328(60)(30)

Table 5.2: Model average results for the observables Φ_D and Φ_{D_s} — defined in eq. (5.14) — which are related to the f_D and f_{D_s} decay constants, respectively, for the two different matching quantities $\phi_H^{(i)}$. The last column reports the result of the combination of these two matching conditions. The first error is statistical while the second is the estimate of systematic uncertainty arising from the model averaging procedure.

5.4.2   *Direct determination of f_{D_s}/f_D*

In addition to the determination of f_D and f_{D_s}, we investigate the direct determination of the ratio f_{D_s}/f_D from a dedicated fit. This allows for a consistency check, since the ratio is dimensionless and thus does not require normalisation with a reference scale such as $\sqrt{8t_0}$. One particular consequence is thus that this approach is only indirectly subject to the uncertainty of the lattice scale setting. Another
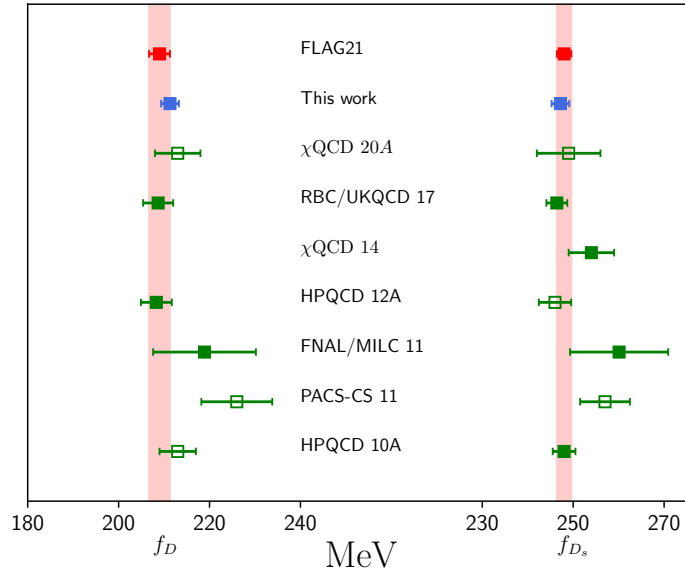
Figure 5.7: Comparison of our results for f_D and f_{D_s} with those from lattice QCD collaborations based on simulations with $N_f = 2 + 1$ dynamical flavors as well as with FLAG21 averages [5]. Only data points with filled symbols contribute to the FLAG averages. Starting from the bottom, results are taken from: HPQCD 10 [50], PACS-CS 11 [106], FNAL/MILC 11 [12], HPQCD 12A [104], χQCD 14 [132], RBC/UKQCD 17 [26], χQCD 20A [37].

advantage is that the ratio is exactly 1 by construction when $m_s = m_l$, i.e., the symmetric point of our $\phi_4 = $ const. trajectory, which is part of our line of constant physics. We can thus perform a fit that is highly constrained in the unphysical masses region, although at the price of reducing the total number of ensembles entering in the study of the approach to the physical point.

A first set of fit ansaetze is derived from HMχPT expressions as in the case for $\Phi_{D_{(s)}}$. The generic form is

$$\frac{\Phi_{D_s}}{\Phi_D} = \left[1 + \left(\delta\Phi_{\chi\text{PT}}^{D_s} - \delta\Phi_{\chi\text{PT}}^{D}\right)\right]\left[1 + \left(\delta\Phi_a^{D_s} - \delta\Phi_a^{D_s}\right)\right]. \quad (5.16)$$

Here $\delta\Phi_{\chi\text{PT}}^{D_{(s)}}$ labels the light quark mass dependence of the ratio, while $\delta\Phi_a^{D_{(s)}}$ controls the continuum approach. In this expression we consider all the possible combinations of non-vanishing fit parameters, and perform our TIC-weighted model average among the different functional forms tested to quote a systematic uncertainty.

We further explore the systematic uncertainties by considering also functional forms based on a Taylor expansion of $\Phi_{D_{(s)}}$. The generic expression then reads

$$\Phi_{D_{(s)}} = \left(\Phi_{D_{(s)}}\right)_\chi \left[1 + \delta\Phi_{h,\text{Taylor}}\right]\left[1 + \delta\Phi_{m,\text{Taylor}}^{D_{(s)}}\right]\left[1 + \delta\Phi_a^{D_{(s)}}\right],$$

$$(5.17)$$

where $\left(\Phi_{D_{(s)}}\right)_\chi$ is the value in the chiral limit and at the physical value of the heavy-quark mass.

Then, in order to arrive at a final determination of f_{D_s}/f_D we perform a model average among all the HMχPT and Taylor functional forms for the two different matching conditions simultaneously. Again, for details of the fit forms employed we refer to our work [34]. In Table 5.3 we report our results for the ratio of decay constants from the model average separately for each charm matching condition, as well as their combination. Also for the ratio we observe good agreement for the two different $\phi_H^{(i)}$ tested in this work. Finally, for the result combining the two matching conditions, we quote

$$\frac{f_{D_s}}{f_D} = 1.177(15)_\text{stat}(5)_\text{syst,} \quad (5.18)$$

where the first error is statistical and the second is the systematic uncertainty based on the model average procedure.

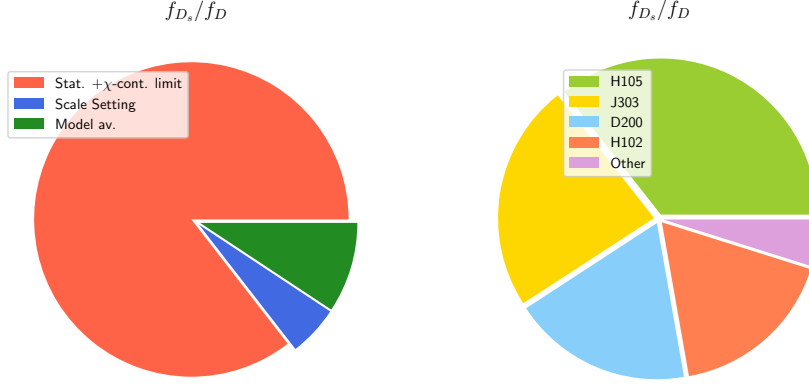|	$\phi_H^{(1)}$	$\phi_H^{(2)}$	combined
f_{D_s}/f_D	1.177(15)(6)	1.178(15)(6)	1.177(15)(5)

Figure 5.8: *Left*: Relative contributions to the total error on the determination of the ratio f_{D_s}/f_D. The label statistical plus χ-continuum limit represents the error arising from the statistical accuracy of our data and the chiral-continuum extrapolation. The scale setting label denotes the error coming from the physical value t_0^{ph}, while the model average represents the systematic error arising from the model variation according to the TIC procedure. *Right*: Details of the relative contributions to the statistical and chiral-continuum extrapolation error arising from specific gauge field configuration ensembles.

Table 5.3: Results of the model average for f_{D_s}/f_D for the two charm-quark matching conditions. The last column reports the combined result. The first error is statistical while the second is the systematic uncertainty arising from the model variation procedure.

In Figure 5.8 we show the major error sources contributing to our final determination of the ratio, where we notice that the major contribution is given by the statistical and chiral-continuum error. Finally, in Figure 5.9 we show a comparison between our result for f_{D_s}/f_D, the FLAG21 average and results from other collaborations.
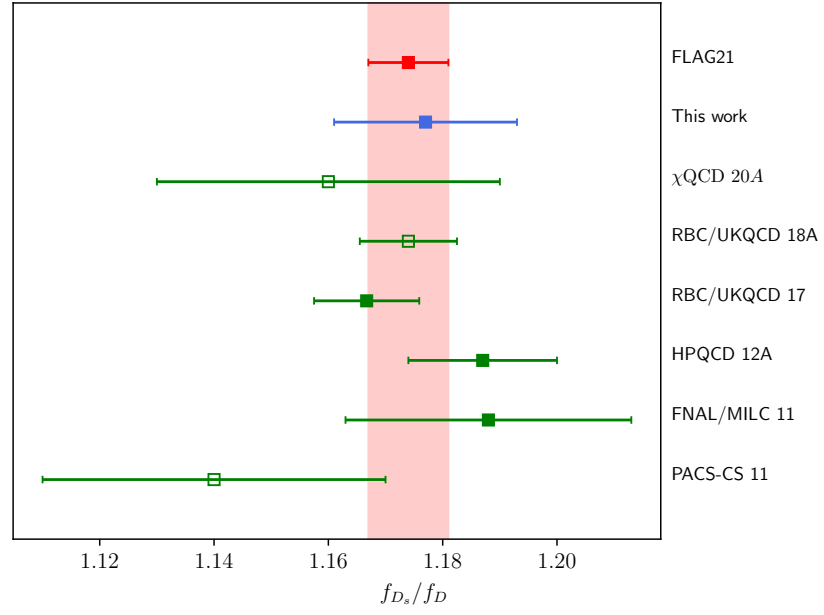
Figure 5.9: Comparison of our determination of f_{D_s}/f_D with those of the other lattice QCD collaborations based on $N_f = 2 + 1$ dynamical simulations as well as with the FLAG average [5]. Only the results with filled symbols contribute to this average. Starting from the bottom, results are taken from: PACS-CS 11 [106], FNAL/MILC 11 [12], HPQCD 12A [104], RBC/UKQCD 17 [26], RBC/UKQCD 18A [25], χQCD 20A [37].

Part IV

CONCLUSIONS

CONCLUSIONS AND OUTLOOK

In this Ph.D. thesis we have obtained high precision results from first-principles Lattice QCD calculations of the gradient flow scale t_0 and the lattice spacing for CLS ensembles. This is relevant in modern day "precision era" Lattice Field Theory computations, since as the community is reaching sub-percent level precision in lattice predictions, setting the scale with the same accuracy is required, such that the scale is not the dominant source of uncertainty. In addition to this and following our scale setting procedure, we obtained high precision results for the renormalized charm quark mass and charmed mesons $D_{(s)}$ decay constants. In particular, these results are of utmost importance for high precision tests of the Standard Model and the search for New Physics, as they are expected to contribute to the detailed understanding of heavy quark dynamics in the Standard Model.

In this work we used CLS lattice gauge ensembles [31, 103] with lattice spacings ranging from $a \approx 0.085$ fm to $a \approx 0.038$ fm, and pion masses from $m_\pi \approx 420$ MeV to the physical point $m_\pi \approx 130$ MeV. We have used a mixed action lattice regularization based on CLS gauge ensembles which uses $N_f = 2 + 1$ $\mathcal{O}(a)$ improved Wilson quarks in the sea and $N_f = 2 + 1 + 1$ Wilson twisted mass in the valence. We performed the matching of the mixed action through the pseudoscalar pion and kaon masses, which fixed equal physical quark masses for the up/down and strange quarks in the sea and valence sectors, treating the additional charm quark as a partially quenched flavor. This ensures unitarity of the theory in the continuum. Furthermore, we tuned the Wilson twisted mass parameters to impose maximal twist, ensuring automatic $\mathcal{O}(a)$ improvement [58, 120] for valence observables up to negligible effects coming from the sea.

We employed the Γ-method to estimate errors from Monte Carlo data and automatic differentiation to perform exact error propagation. This allows to achieve control of autocorrelations and propagate errors into derived quantities. All these techniques are implemented by the ADerrors.jl Julia library [114, 115].

We have presented an update of the scale setting of this mixed action regularization and determined t_0 in physical units with finer lattice spacings and physical pion masses. For this task we employed the pion and kaon decay constants as physical input. We quote as final results for t_0

$$\sqrt{t_0} = 0.1438(7)_{\text{stat}}(4)_{\text{syst}} \text{ fm, } [f_{\pi K}].$$
(5.19)

Using the kaon decay constant to set the scale relies on the determination of the CKM matrix element V_{us} which has bigger uncertainty

than V_{ud}. This large uncertainty affects the final result for the scale, in our case amounting to a $\sim 11\%$ contribution to the total squared error. In addition to this, f_K suffers from stronger QED corrections than f_π, whose uncertainty in our case amounts to a $\sim 3\%$ contribution to the total squared error. For these reasons it is of utmost importance to determine the scale using only the decay constant of the pion, task for which physical point ensembles are of particular relevance. Currently our efforts are focused on this, as well as in the determination of the up/down and strange quark physical masses from a combination of the Wilson unitary and mixed action regularizations.

Furthermore, following our work in [34] we have presented calculations of the determination of the physical charm quark mass and charmed mesons decay constants based on this mixed action setup, exploiting automatic $\mathcal{O}(a)$ improvement to reduce lattice artifacts associated with the heavy charm quark mass. Using our determination of the scale t_0 we quote as final results for the RGI charm quark mass in the three flavor theory

$$M_c^{\mathrm{RGI}}(N_f = 3) = 1.485(8)_{\mathrm{stat}}(3)_{\mathrm{syst}}(14)_{\mathrm{RGI}} \text{ GeV} . \tag{5.20}$$

Converting this result to the $\overline{\mathrm{MS}}$ scheme in the four flavor theory for comparison with the literature we obtain

$$M_c^{\mathrm{RGI}}(N_f = 4) = 1.546(8)_{\mathrm{stat}}(3)_{\mathrm{syst}}(14)_{\mathrm{RGI}}(4)_\Lambda(3)_{\mathrm{trunc.}} \text{ GeV} , \tag{5.21}$$

$$\overline{m}_c(\mu = 3 \text{ GeV}, N_f = 4) = 1.006(5)_{\mathrm{stat}}(2)_{\mathrm{syst}}(9)_{\mathrm{RGI}}(6)_\Lambda(3)_{\mathrm{trunc.}} \text{ GeV} . \tag{5.22}$$

The error of the RGI quark mass is completely dominated by the computation of the non-perturbative renormalization group running factor, and therefore, no substantial improvement can be achieved until a more precise calculation of this quantity is obtained. In particular, the uncertainty in the scale t_0 accounts for $\sim 3\%$ of the squared total error in $M_c^{\mathrm{RGI}}(N_f = 3)$.

For the $D_{(s)}$ decay constants we quote

$$f_D = 211.3(1.9)_{\mathrm{stat}}(0.6)_{\mathrm{syst}} \text{ MeV}, \tag{5.23}$$
$$f_{D_s} = 247.0(1.9)_{\mathrm{stat}}(0.7)_{\mathrm{syst}} \text{ MeV}, \tag{5.24}$$

while for the ratio

$$\frac{f_{D_s}}{f_D} = 1.177(15)_{\mathrm{stat}}(5)_{\mathrm{syst}}. \tag{5.25}$$

In this case, the error is completely dominated by the statistical uncertainty of the gauge ensembles and the chiral-continuum extrapolations, and in the individual results for $f_{D_{(s)}}$ decay constants the scale setting accounts for the second largest contribution.

The results in the charm sector are based on a subset of the ensembles used for the scale setting. Currently we are focused on including the whole set of ensembles in Table C.1 to the analysis of the charm sector.

We stress that the results obtained in this thesis are computed in the isosymmetric QCD limit, defined in [5]. Given the accuracy of our results, QED effects and strong isospin breaking effects are expected to be relevant, specially for charm observables. In future studies, where higher precision results can be achieved by increasing statistics and adding further ensembles, these effects will have to be taken into account.

CONCLUSIONES Y PERSPECTIVAS

Blabla, semileptónicas

Part V

APPENDICES

CONVENTIONS

In this Appendix we set some useful notation used throughout this work. We begin with the Dirac or Gamma matrices γ_μ, which are 4×4 complex matrices defined by the anticommutator relation

$$\{\gamma_\mu, \gamma_\nu\} = 2g_{\mu\nu}1_{4\times 4}, \tag{A.1}$$

with $g_{\mu\nu}$ the metric tensor of 4-dimensional space-time. We will work in the Euclidean and flat space, so

$$g_{\mu\nu} = \text{diag}(+1, +1, +1, +1). \tag{A.2}$$

Some useful properties of the Gamma matrices are

- Hermiticity: $\gamma_\mu^\dagger = \gamma_\mu$.

- They are traceless: $\text{tr}(\gamma_\mu) = 0$.

- Involutory: $\gamma_\mu^{-1} = \gamma_\mu$.

A fifth Gamma matrix can be defined as

$$\gamma_5 = \gamma_0\gamma_1\gamma_2\gamma_3, \tag{A.3}$$

which fulfills the same properties as above, and anticommutes with all other Gamma matrices

$$\{\gamma_5, \gamma_\mu\} = 0. \tag{A.4}$$

These matrices control the flavor content of hadrons, and as such appear in the definition of the lattice hadron interpolators. The relevant quark bilinears needed for this work are

- Scalar density: $S^{ij} = \bar{\psi}^i\psi^j$.

- Pseudoscalar density: $P^{ij} = \bar{\psi}^i\gamma_5\psi^j$.

- Axial current: $A_\mu^{ij} = \bar{\psi}^i\gamma_\mu\gamma_5\psi^j$.

- Vector current: $V_\mu^{ij} = \bar{\psi}^i\gamma_\mu\psi^j$.

These bilinears are defined in the physical basis $\{\psi, \bar{\psi}\}$. By the change of variables

$$\psi \to e^{i\frac{\pi}{2}\gamma_5 T/2}\psi, \quad \bar{\psi} \to \bar{\psi}e^{i\frac{\pi}{2}\gamma_5 T/2}, \tag{A.5}$$

we define the twisted basis, with T a diagonal matrix in flavor space. With this change of variables and at full twist with $N_f = 2 + 1 + 1$

$$T = \text{diag}(+1, -1, -1, +1), \tag{A.6}$$

the bilinears are rotated as

$$S^{ij} \to S^{ij}, \tag{A.7}$$

$$P^{ij} \to P^{ij}, \tag{A.8}$$

$$A_\mu^{ij} \to iV_\mu^{ij}, \tag{A.9}$$

$$V_\mu^{ij} \to -iA_\mu^{ij}, \tag{A.10}$$

for $(i,j) = (u,d), (u,s), (c,d), (c,s)$, and

$$S^{ij} \to -iP^{ij}, \tag{A.11}$$

$$P^{ij} \to iS^{ij}, \tag{A.12}$$

$$A_\mu^{ij} \to A_\mu^{ij}, \tag{A.13}$$

$$V_\mu^{ij} \to V_\mu^{ij}, \tag{A.14}$$

for $(i,j) = (u,u), (u,c), (d,d), (d,s), (s,s), (c,c)$.

B

GELL-MANN MATRICES AND STRUCTURE CONSTANTS

In this Appendix we give the expressions for the $SU(3)$ group generators in the fundamental representation, given by the Gell-Mann matrices, and the values for the $su(3)$ algebra structure constants.

The Gell-Mann matrices are given by

$$T^{(1)} = \begin{pmatrix} 0 & 1 & 0 \\ 1 & 0 & 0 \\ 0 & 0 & 0 \end{pmatrix}, \; T^{(2)} = \begin{pmatrix} 0 & -i & 0 \\ i & 0 & 0 \\ 0 & 0 & 0 \end{pmatrix}, \; T^{(3)} = \begin{pmatrix} 1 & 0 & 0 \\ 0 & -1 & 0 \\ 0 & 0 & 0 \end{pmatrix},$$

$$T^{(4)} = \begin{pmatrix} 0 & 0 & 1 \\ 0 & 0 & 0 \\ 1 & 0 & 0 \end{pmatrix}, \; T^{(5)} = \begin{pmatrix} 0 & 0 & -i \\ 0 & 0 & 0 \\ i & 0 & 0 \end{pmatrix}, \; T^{(6)} = \begin{pmatrix} 0 & 0 & 0 \\ 0 & 0 & 1 \\ 0 & 1 & 0 \end{pmatrix},$$

$$T^{(7)} = \begin{pmatrix} 0 & 0 & 0 \\ 0 & 0 & -i \\ 0 & i & 0 \end{pmatrix}, \; T^{(8)} = \frac{1}{\sqrt{3}} \begin{pmatrix} 1 & 0 & 0 \\ 0 & 1 & 1 \\ 0 & 0 & -2 \end{pmatrix}. \tag{B.1}$$

The structure constants of the group f_{abc} are obtained from the commutators of group generators

$$\left[T^{(a)}, T^{(b)} \right] = i f_{abc} T^{(c)}, \tag{B.2}$$

and they are universal, not depending on the choice of the representation. They are totally antisymmetric and given by

$$f_{123} = 1, \tag{B.3}$$

$$f_{147} = -f_{156} = f_{246} = f_{257} = f_{345} = -f_{367} = \frac{1}{2}, \tag{B.4}$$

$$f_{458} = f_{678} = \frac{\sqrt{3}}{2}, \tag{B.5}$$

and all other f_{abc} not related to the ones above by permuting indices are zero.

LATTICE ENSEMBLES

id	β	m_π [MeV]	m_K [MeV]	T/a	L/a	$m_\pi L$	cnfg	BC	charm
H101	3.40	421	421	96	32	5.8	1001,1009	OBC	yes
H102r001	3.40	355	442	96	32	4.9	997	OBC	yes
H102r002	3.40	360	445	96	32	5.0	1008	OBC	yes
H105	3.40	284	471	96	32	3.9	947,1042	OBC	yes
H105r005	3.40	286	467	96	32	3.9	837	OBC	yes
H400	3.46	426	426	96	32	5.2	505,540	OBC	yes
D450	3.46	222	480	128	64	5.4	1000	PBC	no
N202	3.55	416	416	128	48	6.4	899	OBC	yes
N203	3.55	348	446	128	48	5.4	756,787	OBC	yes
N200	3.55	287	468	128	48	4.4	856,856	OBC	yes
D200	3.55	203	486	128	64	4.2	2001	OBC	yes
E250	3.55	130	497	192	96	4.0	1009	PBC	no
N300r002	3.70	424	424	128	48	5.1	1521	OBC	yes
N302	3.70	348	453	128	48	4.2	2201	OBC	no
J303	3.70	259	480	192	64	4.1	1073	OBC	yes
E300	3.70	176	496	192	96	4.2	1139	OBC	no
J500	3.85	417	417	192	64	5.2	789,655,431	OBC	no
J501	3.85	340	453	192	64	4.3	1635,1142,1150	OBC	no

Table C.1: List of CLS ensembles [31, 103] under study. They use the Lüscher-Weisz gauge action defined in eq. (1.95) and non-perturbatively $\mathcal{O}(a)$ improved $N_f = 2 + 1$ Wilson fermions (see eq. (1.102)). All ensembles use open boundary conditions (OBC) in time except for E250 and D450 (periodic), and periodic boundary conditions for all spatial directions. The last column refers to whether the corresponding ensemble is included in the analysis of charm physics in Chapter 5.

LATTICE OBSERVABLES

id	t_0	ϕ_2	ϕ_4	m_{12}	m_{13}	f_π	f_K
H101	2.8619(99)	0.7664(39)	1.1496(59)	0.009206(49)	0.009206(49)	0.06353(33)	0.06353(33)
H102	2.8855(75)	0.5512(40)	1.1234(60)	0.006509(54)	0.010178(51)	0.06080(25)	0.06412(22)
H105	2.8875(80)	0.3475(46)	1.1153(63)	0.004007(51)	0.011385(70)	0.05729(48)	0.06474(26)
H400	3.6356(101)	0.7775(52)	1.1662(79)	0.008284(64)	0.008284(64)	0.05885(25)	0.05885(25)
D450	3.6942(69)	0.2108(22)	1.1034(62)	0.002134(24)	0.010788(23)	0.05000(34)	0.05722(32)
N202	5.1662(194)	0.7409(54)	1.1113(81)	0.006854(16)	0.006854(16)	0.04829(21)	0.04829(21)
N203	5.1519(55)	0.5191(31)	1.1106(52)	0.004743(18)	0.007907(17)	0.04645(15)	0.04909(15)
N200	5.1601(59)	0.3524(21)	1.1123(33)	0.003157(12)	0.008649(12)	0.04433(14)	0.04909(15)
D200	5.1789(56)	0.1767(13)	1.1040(18)	0.001542(9)	0.009385(8)	0.0423(14)	0.04914(10)
E250	5.2075(45)	0.0738(16)	1.0958(37)	0.000643(15)	0.009754(11)	0.0396(52)	0.04826(47)
N300	8.5665(247)	0.7730(51)	1.1595(77)	0.005509(7)	0.005509(7)	0.03802(18)	0.03802(18)
N302	8.5212(207)	0.5184(42)	1.1372(68)	0.003719(9)	0.006407(12)	0.03651(18)	0.03865(24)
J303	8.6189(127)	0.2915(17)	1.1332(35)	0.002048(7)	0.007196(7)	0.03415(22)	0.03873(15)
E300	8.6283(213)	0.1335(10)	1.1292(23)	0.000934(5)	0.007724(6)	0.03233(19)	0.03816(37)
J500	13.9802(319)	0.7376(54)	1.1063(81)	0.004219(5)	0.004219(5)	0.02976(23)	0.02976(23)
J501	14.0241(637)	0.4907(31)	1.1194(49)	0.002740(4)	0.004959(3)	0.02829(21)	0.03010(20)

Table D.1: Unshifted results for the lattice observables entering the scale setting analysis for the Wilson unitary setup. We quote the improved and renormalized decay constants, but bare unimproved PCAC quark masses. False replicas (H102r001, H102r002) and (H105, H105r005) are averaged together.

id	t_0	ϕ_2	ϕ_4	m_{12}	m_{13}	f_π	f_K
H101	2.8796(113)	0.7339(60)	1.1009(89)	0.008786(80)	0.008786(80)	0.06301(37)	0.06301(37)
H102	2.8946(91)	0.5422(37)	1.1009(89)	0.006386(50)	0.009920(96)	0.06058(26)	0.06371(22)
H105	2.8941(68)	0.3424(42)	1.1009(89)	0.003945(48)	0.011167(98)	0.05732(49)	0.06460(28)
H400	3.6579(101)	0.7339(60)	1.1009(89)	0.007778(94)	0.007778(94)	0.05631(32)	0.05631(32)
D450	3.6953(95)	0.2101(32)	1.1009(89)	0.002126(34)	0.010735(95)	0.05000(35)	0.05719(39)
N202	5.1696(204)	0.7339(60)	1.1009(89)	0.006785(77)	0.006785(77)	0.04823(23)	0.04823(23)
N203	5.1556(69)	0.5166(29)	1.1009(89)	0.004710(31)	0.007816(81)	0.04641(16)	0.04902(17)
N200	5.1647(69)	0.3497(24)	1.1009(89)	0.003134(20)	0.008537(82)	0.04433(16)	0.04900(19)
D200	5.1803(75)	0.1760(20)	1.1009(89)	0.001536(20)	0.009342(78)	0.04233(17)	0.04913(17)
E250	5.2051(60)	0.0747(22)	1.1009(89)	0.000655(26)	0.009775(74)	0.03965(53)	0.04834(51)
N300	8.5874(260)	0.7339(60)	1.1009(89)	0.005155(84)	0.005155(84)	0.03774(23)	0.03774(23)
N302	8.534(206)	0.5116(36)	1.1009(89)	0.003641(25)	0.006163(76)	0.03646(20)	0.03849(26)
J303	8.6319(150)	0.2866(20)	1.1009(89)	0.002013(13)	0.006960(71)	0.03409(25)	0.03851(19)
E300	8.6407(236)	0.1300(16)	1.1009(89)	0.000901(13)	0.007522(64)	0.03226(20)	0.03793(39)
J500	13.9817(332)	0.7339(60)	1.1009(89)	0.004200(43)	0.004200(43)	0.02978(23)	0.02978(23)
J501	14.0304(656)	0.4878(27)	1.1009(89)	0.002714(16)	0.004858(56)	0.02831(22)	0.03005(21)

Table D.2: Mass shifted results for the lattice observables entering the scale setting analysis for the Wilson unitary setup. The mass shift is done to impose eq. (3.19) as explained in Sec. 3.4. We quote the improved and renormalized decay constants, but bare unimproved PCAC quark masses. False replicas (H102r001, H102r002) and (H105, H105r005) are averaged together.

id	t_0	ϕ_2	ϕ_4	μ_{12}	μ_{13}	f_π	f_K
H101	2.8796(113)	0.7339(60)	1.1009(89)	0.006442(6)	0.006442(6)	0.06683(295)	0.06683(295)
H102	2.8946(91)	0.5422(37)	1.1009(89)	0.0047221(4)	0.0074111(5)	0.06456(220)	0.06822(171)
H105	2.8941(68)	0.3424(42)	1.1009(89)	0.00292(4)	0.0081555(7)	0.06197(246)	0.06855(198)
H400	3.6579(101)	0.7339(60)	1.1009(89)	0.0058396(6)	0.0058396(6)	0.05921(267)	0.05921(267)
D450	3.6953(95)	0.2101(32)	1.1009(89)	0.0015335(2)	0.0080004(7)	0.05330(360)	0.06052(313)
N202	5.1696(204)	0.7339(60)	1.1009(89)	0.0051151(5)	0.0051151(5)	0.04980(224)	0.04980(224)
N203	5.1556(69)	0.5166(29)	1.1009(89)	0.0035383(2)	0.0059928(6)	0.04817(203)	0.05086(180)
N200	5.1647(69)	0.3497(24)	1.1009(89)	0.0023932(2)	0.0065326(6)	0.04617(267)	0.05092(154)
D200	5.1803(75)	0.1760(20)	1.1009(89)	0.0012082(1)	0.0071335(7)	0.04461(144)	0.05073(156)
E250	5.2051(60)	0.0747(22)	1.1009(89)	0.0004842(2)	0.0074652(7)	0.04197(409)	0.05002(442)
N300	8.5874(260)	0.7339(60)	1.1009(89)	0.0041042(5)	0.0041042(5)	0.03848(231)	0.03848(231)
N302	8.534(206)	0.5116(36)	1.1009(89)	0.0028252(2)	0.0049066(6)	0.03733(234)	0.03956(232)
J303	8.6319(150)	0.2866(20)	1.1009(89)	0.0015912(1)	0.0054355(5)	0.03552(185)	0.03959(224)
E300	8.6407(236)	0.1300(16)	1.1009(89)	0.0007122(1)	0.0061255(5)	0.0336(218)	0.03938(538)
J500	13.9817(332)	0.7339(60)	1.1009(89)	0.0032933(3)	0.0032933(3)	0.03028(233)	0.03028(233)
J501	14.0304(656)	0.4878(27)	1.1009(89)	0.0021711(1)	0.0039285(5)	0.02874(184)	0.03054(195)

Table D.3: Results for the lattice observables entering the scale setting analysis for the mixed action setup. All results are mass shifted to impose eq. (3.19) as explained in Sec. 3.4 and matched though pseudoscalar masses as explained in Sec. 3.5. Values of t_0, ϕ_2 and ϕ_4 are identical to those in Table D.2 by construction. The bare quark masses are given by the bare twist parameters $\mu_l \equiv \mu_{12}$ and $\mu_s \equiv \mu_{13}$. False replicas (H102r001, H102r002) and (H105, H105r005) are averaged together.

SIMULATION DETAILS

In this Appendix we discuss the details of the generation of gauge field configurations with dynamical quarks for the study of Lattice QCD.

Typically, simulations of lattice QCD with dynamical quarks require a large amount of computer resources due to the large number of degrees of freedom, the need for big volumes and small lattice spacings. The constant efforts by the community paved the way for simulations with up to four dynamical quarks.

All ensembles studied in this thesis were generated using the open-QCD software, and hence the details we review here are those of the algorithms implemented for this software [86, 90].

As outlined in Sec. 1.4, the expectation value of a composite operator O can be computed on the lattice as

$$\langle O \rangle = \frac{1}{\mathcal{Z}} \int \mathcal{D}[U] e^{-S_{\mathrm{G}}[U] - S_{\mathrm{eff}}[U]} O[U] \approx \frac{1}{N_{\mathrm{cnfg}}} \sum_{i=1}^{N_{\mathrm{cnfg}}} O[U_i] + \mathcal{O}\left(\frac{1}{\sqrt{N_{\mathrm{cnfg}}}}\right),$$

(E.1)

where the gauge fields U_i are sampled from the probability density

$$dP[U] = \frac{e^{-S_{\mathrm{G}}[U] - S_{\mathrm{eff}}[U]}}{\int \mathcal{D}[U] e^{-S_{\mathrm{G}}[U] - S_{\mathrm{eff}}[U]}}.$$

(E.2)

The central idea is to perform an importance sampling of the distribution in eq. (E.2), such that regions of field space with high probability are highly populated with gauge configurations U_i. To achieve this, typically gauge configurations are generated following a Markov chain. This is defined as a sequence $\{U_k\}_{k=1}^{N_{\mathrm{cnfg}}}$ such that the k-th element is generated from the previous one, with k labeling the Monte Carlo (MC) time. This way, the Markov Chain is generated from the initial state U_1 and the transition probability $T(U_{k-1} \to U_k)$. Due to this gauge configurations in one same Markov Chain are highly correlated, issue which we deal with in Appendix F. The transition probabilities must obey the following conditions:

- Ergodicity: given a subset of states S from the Markov Chain, there are always at least two states $s \in S$ and $s' \notin S$ with $T(s \to s') > 0$. This is of particular importance in the context of Lattice QCD and Lattice Yang-Mills theories in order to ensure that the simulation algorithm is sampling correctly all topological sectors of the theory, which may not always be the case for different algorithms.

- Equilibrium: normalizing the transition probability as

$$\sum_s T(s \rightarrow s') = 1 \quad \forall s,$$
(E.3)

then it must hold that

$$\sum_s P(s)T(s \rightarrow s') = P(s') \quad \forall s',$$
(E.4)

where $P(s)$ is the equilibrium distribution in eq. (E.2). This ensures that starting from a random configuration, after applying iteratively the transition probability, we asymptotically reach the target equilibrium distribution in eq. (E.2).

Different choices for the transition probability $T(s \rightarrow s')$ satisfying the above conditions define the different sampling algorithms which we go on to review.

E.1 METROPOLIS ALGORITHM

The Metropolis algorithm [100] is one of the most popular choices for generating a Markov Chain of gauge field configurations for pure gauge theories, for which the target distribution is

$$dP[U] = \frac{e^{-S_G[U]}}{\int \mathcal{D}[U] e^{-S_G[U]}}.$$
(E.5)

The idea is to define an a priori selection probability $T_0(U_i \rightarrow U_j)$ to update a single gauge link. One such choice is to take a random element g of the $SU(N)$ group close to the identity and update the gauge link $U_\mu(n)$ as $U_\mu(n)' = gU_\mu(n)$ such that the new gauge configuration U_j is close to the original one U_i. In order for the transition to be symmetric, group elements g and g^{-1} have to be selected with equal probability. After updating with this a priori transition probability, one supplements the updating process with an accept-reject step, such that the new proposed gauge link is accepted with probability

$$P_{\text{acc}}(i,j) = \min\left(1, e^{-\Delta S}\right), \quad \Delta S = S[U_j] - S[U_i].$$
(E.6)

Then the total transition probability is given by

$$T(U_i \rightarrow U_j) = T_0(U_i \rightarrow U_j)P_{\text{acc}}(i,j) + \delta_{ij}\sum_k T_0(U_i \rightarrow U_j)(1 - P_{\text{acc}}(i,j)).$$
(E.7)

This T satisfies all the desired properties for a transition probability and asymptotically reaches the target distribution probability for pure gauge theories.

The drawback of this algorithm is that it only updates a single gauge link at each step and as such is highly inefficient, particularly for large volume simulations. Over the years new alternatives for pure gauge simulations have been proposed, such as the heat bath [45] and overrelaxation [1, 46] algorithms.

Having as target distribution that of pure gauge theory is equivalent to treating quarks in the sea as static sources (infinitely heavy). In order to simulate full QCD, one needs to have dynamical quarks in the sea, meaning having target distribution eq. (E.2), where S_{eff} introduces non-local dependencies in the gauge links due to the quark determinant. Therefore, algorithms like Metropolis, which updates the gauge configurations link by link, experience a significant computational cost that increases with the lattice volume squared, which makes the algorithm unpractical for dynamical simulations purposes. The Hybrid Monte Carlo (HMC) algorithm [56, 67] significantly improves efficiency by doing global updates of the gauge configurations.

The HMC uses the classical equations of motion to propose new gauge configurations. To this purpose, the field space is extended with the introduction of the conjugate momenta $\pi_\mu(x)$ of the link variables $U_\mu(x)$. The Hamiltonian of the system is

$$H[\pi, U] = \frac{1}{2} \sum_{x,\mu} \pi_\mu^a(x) \pi_\mu^a(x) + S_G[U] + S_{\text{eff}}[U]. \qquad (E.8)$$

This way expectation values can be computed as

$$\langle O \rangle = \frac{\int \mathcal{D}[\pi, U] e^{-H[\pi,U]} O[U]}{\int \mathcal{D}[\pi, U] e^{-H[\pi,U]}}. \qquad (E.9)$$

Now the classical equations of motion read

$$\dot{\pi}_\mu(x) = -F_\mu(x), \quad F_\mu(x) = \left. \frac{\partial S[e^\omega U]}{\partial \omega} \right|_{\omega=0}, \quad \omega \in su(N), \quad (E.10)$$

$$\dot{U}_\mu(x) = \pi_\mu(x) U_\mu(x), \qquad (E.11)$$

where the dot notation "$\dot{a}$" means derivation with respect to MC time. This way, starting from an initial configuration at zero MC time, integrating the equations of motion provides with a global new gauge configuration to be used as proposal for the update of the gauge links. This new global proposal is subject to an accept-reject step like the one in the Metropolis algorithm with

$$P_{\text{acc}} = \min\left(1, e^{-\Delta H}\right), \quad \Delta H = H[\pi', U'] - H[\pi, U]. \qquad (E.12)$$

We have presented the basic formulation of the HMC algorithm but further refinements and improvements, specially in terms of the integration of the classical equations of motion have taken place over the years [70, 112, 127].

This far we have not given details on how to compute the effective fermion action

$$S_{\text{eff}}[U] = -\sum_{i=1}^{N_f} \log \det(D_i). \qquad (E.13)$$

This is a typically challenging task, since it involves dealing with Grassmann variables. A popular solution is to use pseudofermion fields $\Phi(x)$ [126], which are auxiliary fields that carry color and spinor indices c, α but that are complex instead of Grassmann numbers. Restricting to the mass-degenerate doublet of light quarks, where the effective action becomes

$$e^{-S_{\mathrm{eff}}} = \det(D_l)\det(D_l) = \det(D_l^\dagger D_l), \tag{E.14}$$

in the pseudo-fermion representation this becomes up to an irrelevant factor c

$$\det(D_l^\dagger D_l) = c \int \mathcal{D}[\Phi] e^{-S_{\mathrm{pf}}[U,\Phi]}, \tag{E.15}$$

with the pseudo-fermion action given by

$$S_{\mathrm{pf}}[U,\Phi] = \Phi^\dagger \left(D_l^\dagger D_l \right)^{-1} \Phi. \tag{E.16}$$

Now we have all ingredients needed for HMC sampling with dynamical fermions. First, one samples randomly a set of conjugate momenta π_μ and pseudo-fermion fields Φ with Gaussian distribution $\propto \exp\left(-\frac{1}{2}\pi_\mu\pi_\mu - S_{\mathrm{pf}}\right)$. Together with an initial gauge field configuration U_i, the classical equations of motion are integrated up to some later time. At this point one implements the accept-reject step and updates the gauge configuration to U_{i+1}.

This far we assumed two degenerate flavors of quarks to compute the effective fermion action. The inclusion of a strange quark, as in the case of the CLS ensembles we use in this work, complicates things since it does not belong to a mass-degenerate doublet, and thus one needs to compute $\det(D_s)$ and not $\det(D_l^\dagger D_l)$. When this happens, the quark determinant is not ensured to be positive anymore due to explicit chiral symmetry breaking by the Wilson term in Wilson quarks. This is of particular relevance because if the strange quark determinant gets a negative value one cannot interpret the factor $e^{-S_{\mathrm{G}} - S_{\mathrm{eff}}}$ appearing in the path integral as a probability. In CLS ensembles this difficulty is tackled by the Rational Hybrid Monte Carlo algorithm [39, 80]. However, in [102] it was found that some configurations still suffered from a negative strange quark determinant. In this case we introduce a reweighting factor with minus sign to account for the effect. Reweighting is discussed in the next section.

E.3   REWEIGHTING

The idea of reweighting was first proposed in [88] in order to deal with exceptional gauge configurations in the HMC algorithm. These are gauge configurations with near to zero eigenvalues for the Dirac operator, which can appear due to the explicit chiral symmetry breaking induced by the Wilson term in the Wilson fermion action.

In the context of CLS ensembles, a small twisted mass term μ_0 is included in the light quark determinant as [90]

$$\det\left(Q^\dagger Q\right) \to \det\left(\left(Q^\dagger Q + \mu_0^2\right)^2 \left(Q^\dagger Q + 2\mu_0^2\right)^{-1}\right), \qquad \text{(E.17)}$$

with the Hermitian Dirac operator given by $Q = \gamma_5 D$. This provides an infrared cutoff to cancel low-mode eigenvalues. Using the Hasenbusch's mass factorization [70]

$$\det\left(\left(Q^\dagger Q + \mu_0^2\right)^2 \left(Q^\dagger Q + 2\mu_0^2\right)^{-1}\right) \qquad \text{(E.18)}$$

$$= \det\left(Q^\dagger Q + \mu_n^2\right) \det\left(\frac{Q^\dagger Q + \mu_0^2}{Q^\dagger Q + 2\mu_0^2}\right) \times \Pi_{i=1}^n \det\left(\frac{Q^\dagger Q + \mu_{i-1}^2}{Q^\dagger Q + \mu_i^2}\right), \qquad \text{(E.19)}$$

where the twisted mass factors are ordered as $\mu_0 < \mu_1 < ... < \mu_n$. We used γ_5-hermiticity of the Dirac operator D so that

$$Q^\dagger Q = \gamma_5 D^\dagger \gamma_5 D = D^\dagger D. \qquad \text{(E.20)}$$

The values of the twisted mass factors have to be properly chosen as large values might lead to large fluctuations and poor efficiency of the algorithm. After introducing such twisted masses, in order to account for their effect and recover the target desired distribution $dP[U]$ of QCD (in which this twisted mass is not present) a reweighting of expectation values over gauge configurations is needed

$$\langle O \rangle_{\text{rw}} = \frac{\langle OW \rangle}{\langle W \rangle}, \qquad \text{(E.21)}$$

where W is the reweighting factor and in this case reads

$$W = \det\left(Q^\dagger Q \left(Q^\dagger Q + 2\mu_0^2\right) \left(Q^\dagger Q + \mu_0^2\right)^{-2}\right). \qquad \text{(E.22)}$$

In addition to twisted mass reweighting, reweighting is also needed due to the use of the RHMC algorithm to simulate the strange quark determinant. This algorithm uses the rational approximation to the strange quark determinant [39, 80], which is expected to make it positive. However, as mentioned in the previous section, in [102] it was found that some configurations still got a negative sign for the strange quark determinant. This is solved by a reweighting factor of $W_s = -1$ for said configurations, which we list in Table E.1 for the ensembles of interest in this thesis.

id	cnfg
H105r001	3

H105r002	1
H105r005	254, 255, 256, 257, 259, 260, 261, 264, 265, 266, 269, 280, 282, 283, 284, 285, 286, 287, 288, 289, 291, 299, 301, 313, 314, 315, 316, 331, 332, 333, 334, 335, 336, 337, 338, 339, 340, 341, 342
J303r003	324, 325, 326

Table E.1: List of configurations with negative sign of the strange quark determinant for each affected ensemble in this study. A reweighting factor $W_s = -1$ is introduced in said configuration in order to account for the effect [102].

ERROR ANALYSIS

In this Appendix we discuss how to perform the data analysis of correlation functions and the different lattice observables extracted from lattice simulations.

As detailed in Appendix E, lattice data is measured from Monte Carlo (MC) sampling, and estimates of expectation values of physical observables are extracted from means over the MC time. A crucial step is to assign a proper statistical and systematic uncertainties to these mean values, for which it is needed to take into account the autocorrelated nature of MC measurements. This autocorrelation arises from the fact that each gauge configuration is proposed from the previous one (Markov chain). Some popular methods to deal with these correlations are binning, bootstrap and the jack-knife methods.

A recent technique which we will use in this work was proposed by the ALPHA collaboration [114, 117, 130] and is known as Γ-method, which explicitly computes the autocorrelation function to estimate the statistical uncertainty.

In lattice simulations typically one measures a primary observable p_i over several ensembles (defined by the simulation parameters like the inverse coupling β and κ parameter)

$$p_i^\alpha(k), k = 1, ..., N_\alpha, \tag{F.1}$$

where α labels the ensemble and k is the MC time running over the total number of gauge configurations N_α of the given ensemble. In our context, primary observable means a correlation function for some given Euclidean time. An estimate for the true value P_i^α is given by the mean value

$$\bar{p}_i^\alpha = \frac{1}{N_\alpha} \sum_{k=1}^{N_\alpha} p_i^\alpha(k) \xrightarrow[N_\alpha \to \infty]{} P_i^\alpha. \tag{F.2}$$

This is an unbiased estimator. Fluctuations over the MC time can be computed as

$$\delta_i^\alpha(k) = p_i^\alpha(k) - \bar{p}_i^\alpha. \tag{F.3}$$

Due to the Central Limit theorem, we are ensured that $\bar{p}_i^\alpha$ behaves as a Gaussian distribution independently of the distribution of $p_i^\alpha(k)$, and so the statistical uncertainty associated to $\bar{p}_i^\alpha$ is simply given by the standard deviation σ_i^α,

$$P_i^\alpha \approx \bar{p}_i^\alpha \pm \sigma_i^\alpha. \tag{F.4}$$

This standard deviation can be computed from the autocorrelation Γ function

$$(\sigma_i^\alpha)^2 = \frac{1}{N_\alpha} \sum_{k=-\infty}^{\infty} \Gamma_{ii}^{\alpha\alpha}(k), \tag{F.5}$$

where the Γ function is defined as

$$\Gamma_{ij}^{\alpha\beta}(k) = \frac{\delta_{\alpha\beta}}{N_\alpha - k} \sum_{k'=1}^{N_\alpha - k} \delta_i^\alpha(k + k')\delta_j^\alpha(k'). \tag{F.6}$$

From the primary observable p_i^α we can compute derived observables $F = f(p_i^\alpha)$, such as meson masses coming from pseudoscalar two point functions. As in the primary observable case, we can estimate this derived observable as

$$\bar{F} = f(\bar{p}_i^\alpha). \tag{F.7}$$

To compute the statistical uncertainty, we can expand f around the true value P_i^α

$$f(P_i^\alpha + \epsilon_i^\alpha) = f(P_i^\alpha) + \bar{f}_i^\alpha \epsilon_i^\alpha + \mathcal{O}((\epsilon_i^\alpha)^2), \tag{F.8}$$

with

$$\bar{f}_i^\alpha = \left. \frac{\partial f(x)}{\partial x} \right|_{x=P_i^\alpha}. \tag{F.9}$$

Now the autocorrelation function of the derived observable F for ensemble α can be defined as

$$\Gamma_F^\alpha(k) = \sum_{ij} \bar{f}_i^\alpha \bar{f}_j^\alpha \Gamma_{ij}^{\alpha\alpha}(k), \tag{F.10}$$

from which the standard deviation of F can be derived

$$\sigma_F^2 = \sum_\alpha \frac{\Gamma_F^\alpha(0)}{N_\alpha} 2\tau_{\text{int}}^\alpha(F), \tag{F.11}$$

where we assumed that several ensembles contribute to F, and hence the sum $\sum_\alpha$ over the subset of them which contribute. The integrated autocorrelation time $\tau_{\text{int}}^\alpha(F)$ is defined as

$$\tau_{\text{int}}^\alpha(F) = \frac{1}{2} + \sum_{k=1}^{\infty} \frac{\Gamma_F^\alpha(k)}{\Gamma_F^\alpha(0)}. \tag{F.12}$$

To estimate it, a truncation in MC time k is needed. The autocorrelation function admits the following expansion [89, 117]

$$\Gamma(k) \approx \sum_{n=0}^{\infty} e^{-k/\tau_n}. \tag{F.13}$$

The slowest mode $\tau_0 \equiv \tau_{\text{exp}}$ is called the exponential autocorrelation time and it gives the decay rate of $\Gamma(k)$. Truncating eq. (F.12) at MC time $k = W_F^\alpha$ introduces a systematic uncertainty of $\mathcal{O}(\exp(-W_F^\alpha / \tau_{\text{exp}}^\alpha))$. The Γ-method proposes as optimal window that which minimizes the sum of statistical (estimated in [95]) and systematic contributions

$$W_F^\alpha = \min_W \left(\sqrt{\frac{2(2W+1)}{N_\alpha}} + e^{-W/\tau_{\text{exp}}^\alpha} \right). \tag{F.14}$$

In [130] it was proposed to set $\tau_{\text{exp}} = S_\tau \tau_{\text{int}}$, with S_τ some value between 2 and 5. One can also vary W_F^α until saturation in τ_{int}^α is reached. Finally, it was also proposed to add an exponential tail [130]

$$\tau_{\text{exp}}^\alpha \frac{\Gamma_F^\alpha(W_F^\alpha + 1)}{\Gamma_F^\alpha(0)}, \tag{F.15}$$

to eq. (F.12) to account for the systematic effect of truncating the sum over MC time. For this, an estimate of τ_{exp}^α is needed for each ensemble. In the case of CLS ensembles an estimation is given in [31]

$$\tau_{\text{exp}}^\alpha = 14(3)\frac{t_0}{a^2}. \tag{F.16}$$

In this thesis we use the Γ-method explained above as it is implemented by the ADerrors.jl julia package [115].

SOLVERS

G.1 STOCHASTIC METHODS

For the computation of correlation functions of fermions on the lattice (e.g. a two-point function, see eq. (1.81)) the inversion of the Dirac operator is required. In particular one needs to compute the inverse of $D(x, y)$ for all spatial positions $\vec{x}, \vec{y}$. This is referred to as inverting the all-to-all Dirac operator. This is computationally very expensive, and stochastic methods can be employed to reduce the computational cost [86]. A set of stochastic noise sources η are introduced such that

$$\langle \eta_i(x) \rangle_\eta = 0, \quad \left\langle \eta_i^\dagger(x) \eta_j(y) \right\rangle_\eta = \delta_{x,y} \delta_{i,j}, \tag{G.1}$$

with $\langle . \rangle_\eta$ meaning average over the N_η samples of some noise distribution. Some common choices are Gaussian, Z_2 or $U(1)$. From these we define

$$\xi_i^q(x) = \sum_y D_q^{-1}(x, y) \eta_i(y), \quad \zeta_{i,B}^r(x) = \sum_y D_r^{-1}(x, y) \gamma_5 \Gamma_B^\dagger \eta_i(y), \tag{G.2}$$

with Γ_B some Gamma matrix. Now, two-point functions like the one in eq. (1.81) can be expressed as

$$\left\langle O_A^{rq}(x_0) O_B^{qr}(y_0) \right\rangle \approx -\frac{a^6}{L^3} \frac{1}{N_\eta} \sum_{i=1}^{N_\eta} \sum_{\vec{x}} \left\langle (\Gamma_A \gamma_5 \zeta_{i,B}^r(x))^\dagger \xi_i^q(x) \right\rangle, \tag{G.3}$$

without the need to compute the all-to-all inverted Dirac operator, therefore reducing significantly the computational effort.

G.2 ITERATIVE SOLVERS

The inversion of the Dirac operator is still needed to compute correlation functions. This means solving the Dirac equation

$$D_q(x, y) \psi_r(y) = \delta_{x,y} \delta_{q,r} \equiv \eta_{x,y,q,r}, \tag{G.4}$$

where q and r are flavor indices. This is usually done by an iterative procedure. The basic idea is to start from an initial approximate solution ψ_0 and define the residue ρ (we suppress indices for simplicity)

$$\rho = D\psi_0 - \eta. \tag{G.5}$$

Then, one solves

$$D\psi_1 = \rho, \tag{G.6}$$

finds the new residue and iterates the process. The algorithm stops when some convergence criterion is met

$$|\rho| < \epsilon, \tag{G.7}$$

with the final approximate solution given by

$$\psi = \psi_0 + \psi_1 + \dots \tag{G.8}$$

The difference between the true and approximate solutions is

$$|\psi - \psi_{\text{true}}| < \epsilon \kappa(D), \tag{G.9}$$

with $\kappa(D)$ the condition number of matrix D

$$\kappa(D) = |D||D^{-1}|. \tag{G.10}$$

The main solvers used in modern lattice simulations use the iterative procedure outlined above to solve the Dirac equation. Some popular choices are the CG, BiCGstab and GCR algorithms, which are all based on the Krylov subspace method and belong to the class of conjugate gradient solvers. For a pedagogical introduction we refer to [63, 86].

G.3 PRECONDITIONING

The smaller the condition number of the Dirac operator, the less iterative steps one needs to perform in order to find the solution to the Dirac equation. Thus, convergence can be improved by suitably transforming the system into one with a smaller $\kappa(D)$. This can be done by finding some similarity transformations easily invertible such that one can write

$$LDR\psi' = L\eta, \quad \psi = R\psi'. \tag{G.11}$$

This is called preconditioning, and there are many different variations. One of the most used is even-odd preconditioning [51]. Lattice sites can be categorized as even or odd depending on the sum of their space-time coordinates. If the points are ordered such that all the even ones come first, the Dirac operator takes the block form

$$D = \begin{pmatrix} D_{ee} & D_{eo} \\ D_{oe} & D_{oo} \end{pmatrix}, \tag{G.12}$$

where D_{eo} captures the terms which couple the odd to the even sites. The block on the diagonal do not couple different lattice sites, and as such $D_{ee,oo}$ are easily invertible. Choosing the preconditioners

$$L = \begin{pmatrix} 1 & -D_{eo}D_{oo}^{-1} \\ 0 & 1 \end{pmatrix}, \quad R = \begin{pmatrix} 1 & 0 \\ -D_{oo}^{-1}D_{oe} & 1 \end{pmatrix}, \tag{G.13}$$

we get

$$LDR = \begin{pmatrix} \hat{D} & 0 \\ 0 & D_{oo} \end{pmatrix}, \quad \hat{D} = D_{ee} - D_{eo}D_{oo}^{-1}D_{oe}. \tag{G.14}$$

The condition number of $\hat{D}$ is usually less than half that of D, and thus even-odd preconditioning leads to an acceleration of the solver by a factor ≥ 2.

Another popular preconditioning which we use in the sector of charm physics is distance preconditioning, for which we refer to [52].

LEAST-SQUARES FITTING

We employ a least-squares method to fit our data to some fit function. This method is based on finding the minimum of the χ^2 function

$$\chi^2 = \sum_{i,j=1}^{N_{\text{dat}}} (y_i - f(x_i; \vec{p})) \, \mathcal{W}_{ij} \, (y_j - f(x_j; \vec{p})) \,, \tag{H.1}$$

where $\{x_i, y_i\}_{i=1,...,N_{\text{dat}}}$ are the data points we want to fit, x being the independent variable and y the abscissa. $\mathcal{W}$ is a matrix which gives different weights to the different data points entering the fit. When $\mathcal{W}$ is chosen to be the inverse of the covariance matrix of the y-data, C^{-1}, the fit is said to be fully correlated. For fits employing a large number of data points, inverting the covariance matrix can be challenging, and alternatively only the diagonal part of C can be used as weight matrix $\mathcal{W}$. This case is referred to as uncorrelated fit. $f(x; \vec{p})$ is the fit function with fit parameters $\vec{p} = (p_1, ..., p_{N_{\text{param}}})$. For a given fit function $f(x; \vec{p})$, the method finds the parameters values that minimize eq. (H.1) for given data points $\{x_i, y_i\}_{i=1,...,N_{\text{dat}}}$.

In our case we perform fits to extract the ground state signal of lattice observables, fitting e.g. an effective mass to a constant plus exponential signals along the lattice time extent. In this case, Euclidean time plays the role of the x. This means fitting $\sim 96 - 192$ points, for which we have to rely on uncorrelated fits since we cannot compute an invertible covariance matrix. However, after minimizing the χ^2 using only the diagonal part of C, uncertainties are properly propagated intro the relevant quantities taking into account all the correlations between the data.

In [30] a method to measure the quality of fits was proposed in terms of p-values, irrespective of the choice of the weight matrix $\mathcal{W}$. There it is also defined a method to compute the expected value of the minimum of χ^2, $\langle \chi^2 \rangle$. In the case of a fully correlated fit it holds that $\langle \chi^2 \rangle = \text{dof}$.

We also perform fits for the chiral-continuum extrapolation of $\sqrt{8t_0} f_{\pi K}$ to set the scale. In this case, the y variable is $\sqrt{8t_0} f_{\pi K}$ while the x is ϕ_2, and thus the latter has its own uncertainty. In this situation,

a generalized χ^2 function can be defined to include uncertainties in x as

$$\chi^2 = \sum_{i,j=1}^{2N_{\text{dat}}} \left(Y_i - F(X_i; \vec{p}, \vec{q})\right) \mathcal{W}_{ij} \left(Y_j - F(X_j; \vec{p}, \vec{q})\right), \tag{H.2}$$

$$Y = (x_1, ..., x_{N_{\text{dat}}}, y_1, ..., y_{N_{\text{dat}}}), \quad X = (x_1, ..., x_{N_{\text{dat}}}, x_1, ..., x_{N_{\text{dat}}}), \tag{H.3}$$

$$F(X_i; \vec{p}, \vec{q}) = \begin{cases} q_i & \text{if } 1 \leq i \leq N_{\text{dat}} \\ f(x_i; \vec{p}) & \text{if } N_{\text{dat}} + 1 \leq i \leq 2N_{\text{dat}} \end{cases}. \tag{H.4}$$

A fully correlated fit in this context means setting $\mathcal{W}$ to the inverse covariance matrix of the generalized data vector Y, $\mathcal{C}$. In our case we cannot invert the full covariance matrix $\mathcal{C}$ either, so we opt for the use of the block of $\mathcal{C}$ corresponding to the covariance matrix of the $\sqrt{8t_0}f_{\pi K}$ data, setting to zero all other elements of $\mathcal{C}$. This amounts to neglect the correlations in the ϕ_2 data and those among ϕ_2 and $\sqrt{8t_0}f_{\pi K}$ in the definition of the χ^2. However, to properly propagate the errors to the relevant quantities after the fit is performed we take into account all the correlations between the data, and in particular between ϕ_2 and $\sqrt{8t_0}f_{\pi K}$. After the fits we observe

$$\frac{\langle \chi^2 \rangle}{\text{dof}} \sim 0.98, \tag{H.5}$$

indicating that using only the covariance matrix of $\sqrt{8t_0}f_{\pi K}$ captures most of the correlations.

GEVP METHOD

For the extraction of meson masses involving heavy flavors (see Sec. 5), we employ a generalised eigenvalue problem (GEVP) variational method defined as

$$\mathbb{C}_X(t)v_n(t,t_{\text{ref}}) = \lambda_n(t,t_{\text{ref}})\mathbb{C}_X(t_{\text{ref}})v_n(t,t_{\text{ref}}) \qquad n = 0,\ldots,N-1,$$

(I.1)

with $t > t_{\text{ref}}$ and where $\mathbb{C}(t)_X$ is a $N \times N$ matrix of Euclidean correlation functions C_X. In particular we use

$$\mathbb{C}_P(t) = \begin{pmatrix} C_P(t) & C_P(t+\tau) \\ C_P(t+\tau) & C_P(t+2\tau) \end{pmatrix},$$

(I.2)

where $C_P(t) \equiv C_P(t+y_0,y_0)$, $t = x_0 - y_0$ and τ is the value of the time shift. Several values of the time shift have been tested, and we observe a mild dependence on small values of τ for the extraction of eigenvalues and eigenvectors. The GEVP is solved in the regime $t_{\text{ref}} \geq t/2$, where a better control over excited state contributions is achieved [18]. We refer to [34] for a detailed discussion of our setup, together with sanity checks on the GEVP. In what follows we set $\tau = 3a$. The ground state meson mass m is extracted from the eigenvalues of the GEVP using

$$am_{\text{eff}}(t,t_{\text{ref}}) = \log\left(\frac{\lambda_0(t,t_{\text{ref}})}{\lambda_0(t+a,t_{\text{ref}})}\right).$$

(I.3)

An example of a GEVP plateau for the heavy-light pseudoscalar mass is shown in Figure I.1.

In the case of meson decay constants involving heavy quarks (see Sec. 5), we employ again the GEVP method to extract the ground state signal of the matrix element $\langle 0|P^{ij}|P^{ij}(\mathbf{p}=\mathbf{0})\rangle$. This is done by considering the normalised eigenvector $v_n(t,t_{\text{ref}})$ in eq. (I.1), where $|P^{ij}(\mathbf{p}=\mathbf{0})\rangle$ stands for the ground state of the meson with flavor content i,j. Namely, we define for each state n the number [18]

$$R_n = (v_n(t,t_{\text{ref}}),\mathbb{C}_P(t)v_n(t,t_{\text{ref}}))^{-1/2}\,e^{E_n t/2},$$

(I.4)

where $(\cdot,\cdot)$ is the usual scalar product and $\mathbb{C}_P$ is the GEVP matrix from eq. (I.2). Then, the ground state matrix element is given by

$$p_{\text{eff}}(t,t_{\text{ref}}) = (v_0(t,t_{\text{ref}}),C_{P,0})R_0, \qquad (C_{P,0})_k = (\mathbb{C}_P)_{k0}$$
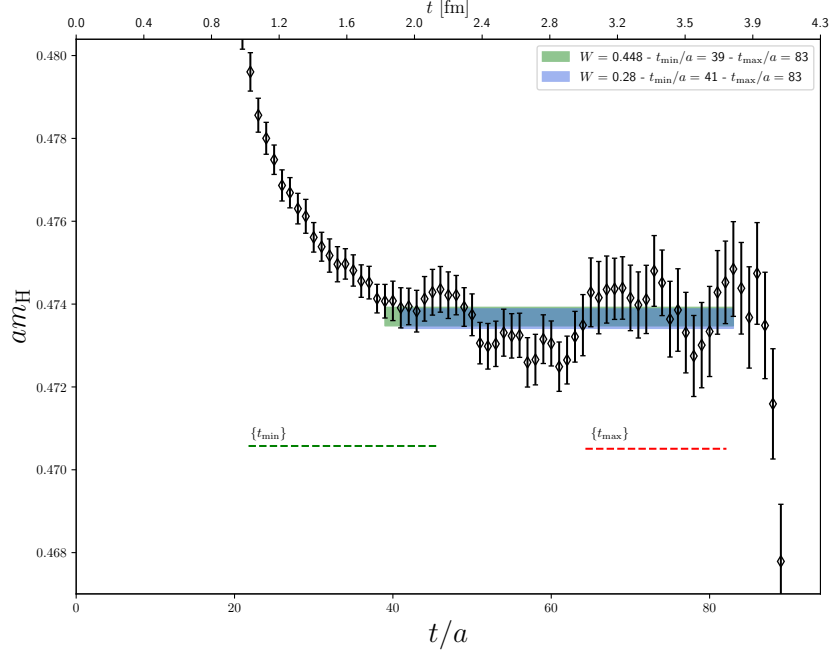
(I.5)

Figure I.1: Illustration of the extraction of the ground-state mass after apply-
ing a GEVP analysis, illustrated for the ensemble J303. We show
the heavy-light pseudoscalar meson mass plateau with the two fit
intervals with higher weights W contributing to the model average
introduced in Sec. 2.7. We also indicate the range of variations
allowed for the interval in Euclidean time where the plateau is
taken. The shaded blue band corresponds to the model average
result.

The large distance behaviour of the effective matrix element is gov-
erned by

$$p_{\text{eff}}(t, t_{\text{ref}}) = p_0 + O(e^{-(E_{N+1}-E_0)t_{\text{ref}}}), \qquad p_0 = \langle 0|P^{ij}|P^{ij}(\mathbf{p}=\mathbf{0})\rangle, \quad (\text{I.6})$$

in the regime where the condition $t_{\text{ref}} \geq t/2$ is satisfied, where E_0 is
the ground state meson mass. In Figure I.2 we show a representative
plateau for a heavy-light decay constant.
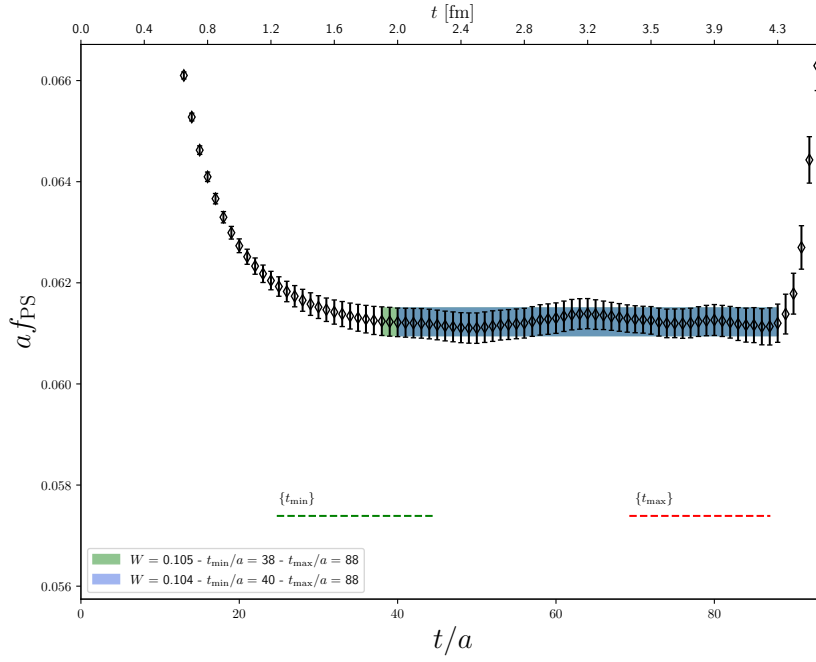
Figure I.2: Illustration of the extraction of the heavy-light pseudoscalar decay
constants, after applying a GEVP analysis, for ensemble J303. We
show the plateau for the heavy-light pseudoscalar decay constant
for the two fit intervals with higher weights in the model average
introduced in Sec. 2.7. The shaded blue band represents the model
average result.

FINITE VOLUME EFFECTS

Simulating QCD in a finite box introduces finite volume effects which can be a source for systematic uncertainties. In Table C.1 we show the volume of each ensemble in terms of $m_\pi L$. It is conventional to consider finite volume effects under control and negligible if $m_\pi L \geq 4$.

ChPT provides us with formulae to account for these finite volume effects. In particular, to NLO the pion and kaon masses and decay constants receive the following corrections [40, 41]

$$X^{(\infty)} = X^{(L)} \frac{1}{1 + R_X}, \tag{J.1}$$

where $X^{(\infty)}$ is observable X at infinite volume and $X^{(L)}$ is said observable at a finite volume L^3, with $X = m_\pi, m_K, f_\pi, f_K$,

$$R_{m_\pi} = \frac{1}{4} \xi_\pi \tilde{g}_1(\lambda_\pi) - \frac{1}{12} \xi_\eta \tilde{g}_1(\lambda_\eta), \tag{J.2}$$

$$R_{m_K} = \frac{1}{6} \xi_\eta \tilde{g}_1(\lambda_\eta), \tag{J.3}$$

$$R_{f_K} = -\xi_\pi \tilde{g}_1(\lambda_\pi) - \frac{1}{2} \xi_K \tilde{g}_1(\lambda_K), \tag{J.4}$$

$$R_{f_\pi} = -\frac{3}{8} \xi_\pi \tilde{g}_1(\lambda_\pi) - \frac{3}{4} \xi_K \tilde{g}_1(\lambda_K) - \frac{3}{8} \xi_\eta \tilde{g}_1(\lambda_\eta), \tag{J.5}$$

$$\xi_{PS} = \frac{m_{PS}^2}{(4\pi f_\pi)^2}, \tag{J.6}$$

$$\lambda_{PS} = m_{PS} L, \tag{J.7}$$

$$\tilde{g}_1(x) = \sum_{n=1}^{\infty} \frac{4m(n)}{\sqrt{n}x} K_1(\sqrt{n}x), \tag{J.8}$$

$$m_\eta^2 = \frac{4}{3} m_K^2 - \frac{1}{3} m_\pi^2, \tag{J.9}$$

where $K_1(x)$ is a Bessel function of the second kind, and the multiplicities $m(n)$ [40] are listed in Table J.1. It is manifest that the lighter the pion mass and the smaller the volume, the stronger the volume corrections. We find these corrections to be less than half a standard deviation for the ensembles with the smallest volumes and lightest pion masses. We nonetheless apply the corrections to all the ensembles.

PCAC quark masses are short distance observables and as such do not receive any infinite volume correction.

n	1	2	3	4	5	6	7	8	9	10
$m(n)$	6	12	8	6	24	24	0	12	30	24

n	11	12	13	14	15	16	17	18	19	20
$m(n)$	24	8	24	48	0	6	48	36	24	24

Table J.1: Multiplicities $m(n)$ calculated in [40] for $n \leq 20$.

$\sqrt{t_0}$: MODEL VARIATION

Wilson analysis	
$[SU(3)\chi PT]$	Eq. (4.13)
$[Tay]$	Eq. (4.20)
$[Tay4]$	Eq. (4.21)
$[SU(2)\chi PT]$	Eq. (4.19)
$[a^2]$	Eq. (4.22)
$[a^2\alpha_S^\Gamma]$	Eq. (4.23)
$[a^2 + a^2\phi_2]$	Eq. (4.24)
$[-]$	No cut in data
$[\beta > 3.40]$	Remove $\beta = 3.40$ ensembles
$[\beta > 3.46]$	Remove $\beta = 3.40$ and $\beta = 3.46$ ensembles
$[m_\pi < 420\ MeV]$	Remove symmetric point ensembles
$[m_\pi < 350\ MeV]$	Remove $\phi_2 > 0.4$ ensembles
$[\beta > 3.40\ \&\ m_\pi < 420\ MeV]$	Remove symmetric point and $\beta = 3.40$ ensembles
$[m_\pi L > 4.1]$	Remove ensembles with volumes $m_\pi L \leq 4.1$

Table K.1: Correspondence between each fit model for the chiral-continuum extrapolation of $\sqrt{8t_0}f_{\pi K}$ and the labels used in Tables K.2-K.4 and Figs. 4.3-4.5. For the combined analysis, we are dealing with two independent cutoff effects, those of the Wilson results and those of the mixed action. In this case we will use two labels for these effects, the first referring to the lattice artifacts explored for the Wilson results, the second one for the mixed action results. If only one label is used it means the same dependence for the lattice artifacts were explored for both regularizations but with independent parameters.

Wilson analysis			
Model	p-value	W	$\sqrt{t_0}$ [fm]
$[\chi SU(3)][a^2][-]$	0.537	0.0768	0.1434(7)
$[\chi SU(3)][a^2][\beta > 3.40]$	0.437	0.0279	0.1432(9)
$[\chi SU(3)][a^2][\beta > 3.46]$	0.4048	0.0122	0.1427(10)

$[\chi SU(3)][a^2][m_\pi < 420\ MeV]$	0.391	0.0178	0.1433(7)
$[\chi SU(3)][a^2][\beta > 3.40\ \&\ m_\pi < 420\ MeV]$	0.2832	0.004	0.1427(11)
$[\chi SU(3)][a^2][m_\pi < 350\ MeV]$	0.187	0.0014	0.1434(9)
$[\chi SU(3)][a^2][m_\pi L > 4.1]$	0.4492	0.0158	0.1436(8)
$[\chi SU(3)][a^2\alpha_s^{\hat{\Gamma}}][-]$	0.5334	0.0729	0.1435(7)
$[\chi SU(3)][a^2\alpha_s^{\hat{\Gamma}}][\beta > 3.40]$	0.4256	0.0271	0.1432(9)
$[\chi SU(3)][a^2\alpha_s^{\hat{\Gamma}}][\beta > 3.46]$	0.4068	0.0122	0.1428(11)
$[\chi SU(3)][a^2\alpha_s^{\hat{\Gamma}}][m_\pi < 420\ MeV]$	0.3806	0.0169	0.1434(7)
$[\chi SU(3)][a^2\alpha_s^{\hat{\Gamma}}][\beta > 3.40\ \&\ m_\pi < 420\ MeV]$	0.2792	0.004	0.1427(11)
$[\chi SU(3)][a^2\alpha_s^{\hat{\Gamma}}][m_\pi < 350\ MeV]$	0.189	0.0014	0.1436(9)
$[\chi SU(3)][a^2\alpha_s^{\hat{\Gamma}}][m_\pi L > 4.1]$	0.4362	0.0148	0.1437(8)
$[\chi SU(3)][a^2 + a^2\phi_2][-]$	0.5014	0.0518	0.1429(11)
$[\chi SU(3)][a^2 + a^2\phi_2][\beta > 3.40]$	0.3868	0.0165	0.1427(14)
$[\chi SU(3)][a^2 + a^2\phi_2][\beta > 3.46]$	0.3306	0.0064	0.1423(17)
$[\chi SU(3)][a^2 + a^2\phi_2][m_\pi < 420\ MeV]$	0.3134	0.0093	0.1430(15)
$[\chi SU(3)][a^2 + a^2\phi_2][m_\pi L > 4.1]$	0.3628	0.0084	0.1433(14)
$[Tay][a^2][-]$	0.4376	0.0463	0.1438(8)
$[Tay][a^2][\beta > 3.40]$	0.3396	0.0172	0.1436(10)
$[Tay][a^2][\beta > 3.46]$	0.3132	0.008	0.1431(11)
$[Tay][a^2][m_\pi < 420\ MeV]$	0.3298	0.0121	0.1437(8)
$[Tay][a^2][\beta > 3.40\ \&\ m_\pi < 420\ MeV]$	0.2058	0.0027	0.1431(11)
$[Tay][a^2][m_\pi < 350\ MeV]$	0.1098	0.0008	0.1438(9)
$[Tay][a^2][m_\pi L > 4.1]$	0.4644	0.0173	0.1440(8)
$[Tay][a^2\alpha_s^{\hat{\Gamma}}][-]$	0.4386	0.0436	0.1439(8)
$[Tay][a^2\alpha_s^{\hat{\Gamma}}][\beta > 3.40]$	0.3374	0.0166	0.1436(10)
$[Tay][a^2\alpha_s^{\hat{\Gamma}}][\beta > 3.46]$	0.3152	0.008	0.1432(11)
$[Tay][a^2\alpha_s^{\hat{\Gamma}}][m_\pi < 420\ MeV]$	0.32	0.0114	0.1438(8)
$[Tay][a^2\alpha_s^{\hat{\Gamma}}][\beta > 3.40\ \&\ m_\pi < 420\ MeV]$	0.2132	0.0027	0.1432(11)
$[Tay][a^2\alpha_s^{\hat{\Gamma}}][m_\pi < 350\ MeV]$	0.1144	0.0008	0.1439(10)
$[Tay][a^2\alpha_s^{\hat{\Gamma}}][m_\pi L > 4.1]$	0.4534	0.0166	0.1441(8)
$[Tay][a^2 + a^2\phi_2][-]$	0.4392	0.0379	0.1431(11)
$[Tay][a^2 + a^2\phi_2][\beta > 3.40]$	0.3244	0.0121	0.1428(14)
$[Tay][a^2 + a^2\phi_2][\beta > 3.46]$	0.2656	0.0047	0.1423(18)
$[Tay][a^2 + a^2\phi_2][m_\pi < 420\ MeV]$	0.275	0.0068	0.1431(15)
$[Tay][a^2 + a^2\phi_2][m_\pi L > 4.1]$	0.43	0.0107	0.1433(14)
$[Tay4][a^2][-]$	0.4258	0.0287	0.1433(9)
$[Tay4][a^2][\beta > 3.40]$	0.3196	0.0094	0.1431(11)
$[Tay4][a^2][\beta > 3.46]$	0.2582	0.0042	0.1427(12)

$[Tay4][a^2][m_\pi < 420\ MeV]$	0.265	0.006	0.1433(10)
$[Tay4][a^2][\beta > 3.40\ \&\ m_\pi < 420\ MeV]$	0.1566	0.0013	0.1426(13)
$[Tay4][a^2][m_\pi < 350\ MeV]$	0.4866	0.0031	0.1417(13)
$[Tay4][a^2][m_\pi L > 4.1]$	0.3784	0.0082	0.1442(12)
$[Tay4][a^2 + a^2\phi_2][-]$	0.3604	0.0176	0.1430(11)
$[Tay4][a^2 + a^2\phi_2][\beta > 3.40]$	0.2508	0.0054	0.1428(14)
$[Tay4][a^2 + a^2\phi_2][\beta > 3.46]$	0.1896	0.0022	0.1425(18)
$[Tay4][a^2 + a^2\phi_2][m_\pi < 420\ MeV]$	0.2086	0.0029	0.1431(15)
$[Tay4][a^2 + a^2\phi_2][m_\pi L > 4.1]$	0.4362	0.0074	0.1431(14)
$[\chi SU(2)][a^2][-]$	0.498	0.0481	0.1432(9)
$[\chi SU(2)][a^2][\beta > 3.40]$	0.3802	0.0158	0.1430(11)
$[\chi SU(2)][a^2][\beta > 3.46]$	0.3546	0.0073	0.1426(11)
$[\chi SU(2)][a^2][m_\pi < 420\ MeV]$	0.3046	0.0078	0.1433(10)
$[\chi SU(2)][a^2][\beta > 3.40\ \&\ m_\pi < 420\ MeV]$	0.2054	0.0017	0.1427(13)
$[\chi SU(2)][a^2][m_\pi < 350\ MeV]$	0.4776	0.003	0.1417(14)
$[\chi SU(2)][a^2][m_\pi L > 4.1]$	0.3668	0.0087	0.1436(10)
$[\chi SU(2)][a^2\alpha_s^{\hat{\Gamma}}][-]$	0.493	0.0443	0.1433(9)
$[\chi SU(2)][a^2\alpha_s^{\hat{\Gamma}}][\beta > 3.40]$	0.3816	0.0153	0.1431(11)
$[\chi SU(2)][a^2\alpha_s^{\hat{\Gamma}}][\beta > 3.46]$	0.3508	0.0072	0.1427(12)
$[\chi SU(2)][a^2\alpha_s^{\hat{\Gamma}}][m_\pi < 420\ MeV]$	0.3104	0.0076	0.1434(10)
$[\chi SU(2)][a^2\alpha_s^{\hat{\Gamma}}][\beta > 3.40\ \&\ m_\pi < 420\ MeV]$	0.197	0.0017	0.1427(13)
$[\chi SU(2)][a^2\alpha_s^{\hat{\Gamma}}][m_\pi < 350\ MeV]$	0.4662	0.003	0.1418(14)
$[\chi SU(2)][a^2\alpha_s^{\hat{\Gamma}}][m_\pi L > 4.1]$	0.3552	0.0082	0.1437(10)
$[\chi SU(2)][a^2 + a^2\phi_2][-]$	0.4598	0.0283	0.1427(13)
$[\chi SU(2)][a^2 + a^2\phi_2][\beta > 3.40]$	0.3206	0.0085	0.1425(16)
$[\chi SU(2)][a^2 + a^2\phi_2][\beta > 3.46]$	0.2796	0.0037	0.1418(21)
$[\chi SU(2)][a^2 + a^2\phi_2][m_\pi < 420\ MeV]$	0.2512	0.0041	0.1427(16)
$[\chi SU(2)][a^2 + a^2\phi_2][m_\pi L > 4.1]$	0.3214	0.0053	0.1427(17)

Table K.2: Model average results for the determination of $\sqrt{t_0}$ at the physical point using the Wilson results. In the first column we label the fit model and data cuts considered according to Table K.1. In the second and third columns we show the quality of fits as measured by the p-value [30] and the assigned weight to each model according to eq. (4.33), respectively. Finally, in the fourth column we show the results coming from each fit model. In all models the penalization of eq. (4.32) was included, so even in "no cut" models points at $\beta = 3.40$ and $m_\pi = 420$ MeV are penalized in the fit.

Mixed action analysis			
Model	p-value	W	$\sqrt{t_0}$ [fm]
$[\chi SU(3)][a^2][-]$	0.595	0.0471	0.1445(9)
$[\chi SU(3)][a^2][\beta > 3.40]$	0.5118	0.0193	0.1445(12)
$[\chi SU(3)][a^2][\beta > 3.46]$	0.438	0.0072	0.1445(14)
$[\chi SU(3)][a^2][m_\pi < 420\,MeV]$	0.5452	0.0176	0.1443(9)
$[\chi SU(3)][a^2][\beta > 3.40\ \&\ m_\pi < 420\,MeV]$	0.3486	0.003	0.1445(15)
$[\chi SU(3)][a^2][m_\pi < 350\,MeV]$	0.351	0.0018	0.1447(10)
$[\chi SU(3)][a^2][m_\pi L > 4.1]$	0.8106	0.0305	0.1445(10)
$[\chi SU(3)][a^2\alpha_s^{\hat{\Gamma}}][-]$	0.5874	0.0473	0.1445(9)
$[\chi SU(3)][a^2\alpha_s^{\hat{\Gamma}}][\beta > 3.40]$	0.5098	0.0193	0.1445(12)
$[\chi SU(3)][a^2\alpha_s^{\hat{\Gamma}}][\beta > 3.46]$	0.4412	0.0072	0.1445(14)
$[\chi SU(3)][a^2\alpha_s^{\hat{\Gamma}}][m_\pi < 420\,MeV]$	0.5372	0.0176	0.1443(9)
$[\chi SU(3)][a^2\alpha_s^{\hat{\Gamma}}][\beta > 3.40\ \&\ m_\pi < 420\,MeV]$	0.3444	0.0029	0.1445(15)
$[\chi SU(3)][a^2\alpha_s^{\hat{\Gamma}}][m_\pi < 350\,MeV]$	0.3514	0.0018	0.1447(10)
$[\chi SU(3)][a^2\alpha_s^{\hat{\Gamma}}][m_\pi L > 4.1]$	0.8182	0.0304	0.1445(10)
$[\chi SU(3)][a^2 + a^2\phi_2][-]$	0.6046	0.0358	0.1438(12)
$[\chi SU(3)][a^2 + a^2\phi_2][\beta > 3.40]$	0.5048	0.0146	0.1435(17)
$[\chi SU(3)][a^2 + a^2\phi_2][\beta > 3.46]$	0.3632	0.0041	0.1441(21)
$[\chi SU(3)][a^2 + a^2\phi_2][m_\pi < 420\,MeV]$	0.4612	0.0092	0.1443(16)
$[\chi SU(3)][a^2 + a^2\phi_2][m_\pi L > 4.1]$	0.8084	0.0202	0.1435(17)
$[Tay][a^2][-]$	0.4208	0.022	0.1449(7)
$[Tay][a^2][\beta > 3.40]$	0.3316	0.0087	0.1449(10)
$[Tay][a^2][\beta > 3.46]$	0.2732	0.0035	0.1449(12)
$[Tay][a^2][m_\pi < 420\,MeV]$	0.388	0.0091	0.1447(8)
$[Tay][a^2][\beta > 3.40\ \&\ m_\pi < 420\,MeV]$	0.235	0.0016	0.1449(14)
$[Tay][a^2][m_\pi < 350\,MeV]$	0.2366	0.0011	0.1450(9)
$[Tay][a^2][m_\pi L > 4.1]$	0.8136	0.031	0.1449(8)
$[Tay][a^2\alpha_s^{\hat{\Gamma}}][-]$	0.4196	0.021	0.1449(7)
$[Tay][a^2\alpha_s^{\hat{\Gamma}}][\beta > 3.40]$	0.337	0.0088	0.1449(11)
$[Tay][a^2\alpha_s^{\hat{\Gamma}}][\beta > 3.46]$	0.281	0.0036	0.1449(13)
$[Tay][a^2\alpha_s^{\hat{\Gamma}}][m_\pi < 420\,MeV]$	0.3906	0.0091	0.1447(8)
$[Tay][a^2\alpha_s^{\hat{\Gamma}}][\beta > 3.40\ \&\ m_\pi < 420\,MeV]$	0.2346	0.0016	0.1449(14)
$[Tay][a^2\alpha_s^{\hat{\Gamma}}][m_\pi < 350\,MeV]$	0.241	0.001	0.1450(9)
$[Tay][a^2\alpha_s^{\hat{\Gamma}}][m_\pi L > 4.1]$	0.8228	0.0306	0.1449(8)
$[Tay][a^2 + a^2\phi_2][-]$	0.4362	0.0185	0.1441(11)
$[Tay][a^2 + a^2\phi_2][\beta > 3.40]$	0.3482	0.0071	0.1438(16)
$[Tay][a^2 + a^2\phi_2][\beta > 3.46]$	0.225	0.002	0.1446(21)

$[Tay][a^2 + a^2\phi_2][m_\pi < 420\ MeV]$	0.3198	0.005	0.1447(15)
$[Tay][a^2 + a^2\phi_2][m_\pi L > 4.1]$	0.8716	0.0252	0.1436(16)
$[Tay4][a^2][-]$	0.6728	0.042	0.1438(10)
$[Tay4][a^2][\beta > 3.40]$	0.6106	0.0182	0.1438(13)
$[Tay4][a^2][\beta > 3.46]$	0.447	0.0053	0.1439(14)
$[Tay4][a^2][m_\pi < 420\ MeV]$	0.5022	0.0098	0.1438(11)
$[Tay4][a^2][\beta > 3.40\ \&\ m_\pi < 420\ MeV]$	0.292	0.0016	0.1439(16)
$[Tay4][a^2][m_\pi < 350\ MeV]$	0.7832	0.0031	0.1432(14)
$[Tay4][a^2][m_\pi L > 4.1]$	0.739	0.0143	0.1448(14)
$[Tay4][a^2 + a^2\phi_2][-]$	0.6244	0.0246	0.1439(12)
$[Tay4][a^2 + a^2\phi_2][\beta > 3.40]$	0.5074	0.0098	0.1439(16)
$[Tay4][a^2 + a^2\phi_2][\beta > 3.46]$	0.4372	0.0036	0.1453(21)
$[Tay4][a^2 + a^2\phi_2][m_\pi < 420\ MeV]$	0.4972	0.0066	0.1448(15)
$[Tay4][a^2 + a^2\phi_2][m_\pi L > 4.1]$	0.8872	0.015	0.1437(16)
$[\chi SU(2)][a^2][-]$	0.7174	0.0543	0.1439(8)
$[\chi SU(2)][a^2][\beta > 3.40]$	0.6384	0.0228	0.1439(11)
$[\chi SU(2)][a^2][\beta > 3.46]$	0.4706	0.0067	0.1441(13)
$[\chi SU(2)][a^2][m_\pi < 420\ MeV]$	0.5222	0.0101	0.1438(10)
$[\chi SU(2)][a^2][\beta > 3.40\ \&\ m_\pi < 420\ MeV]$	0.2878	0.0016	0.1440(16)
$[\chi SU(2)][a^2][m_\pi < 350\ MeV]$	0.7764	0.0031	0.1432(13)
$[\chi SU(2)][a^2][m_\pi L > 4.1]$	0.7592	0.0178	0.1442(10)
$[\chi SU(2)][a^2\alpha_s^{\hat{\Gamma}}][-]$	0.7204	0.0545	0.1439(8)
$[\chi SU(2)][a^2\alpha_s^{\hat{\Gamma}}][\beta > 3.40]$	0.6196	0.0231	0.1439(12)
$[\chi SU(2)][a^2\alpha_s^{\hat{\Gamma}}][\beta > 3.46]$	0.4916	0.0067	0.1441(13)
$[\chi SU(2)][a^2\alpha_s^{\hat{\Gamma}}][m_\pi < 420\ MeV]$	0.5264	0.0101	0.1438(10)
$[\chi SU(2)][a^2\alpha_s^{\hat{\Gamma}}][\beta > 3.40\ \&\ m_\pi < 420\ MeV]$	0.3014	0.0016	0.1439(16)
$[\chi SU(2)][a^2\alpha_s^{\hat{\Gamma}}][m_\pi < 350\ MeV]$	0.7714	0.0031	0.1432(13)
$[\chi SU(2)][a^2\alpha_s^{\hat{\Gamma}}][m_\pi L > 4.1]$	0.7468	0.0177	0.1441(10)
$[\chi SU(2)][a^2 + a^2\phi_2][-]$	0.6492	0.0334	0.1441(13)
$[\chi SU(2)][a^2 + a^2\phi_2][\beta > 3.40]$	0.5466	0.0119	0.1440(18)
$[\chi SU(2)][a^2 + a^2\phi_2][\beta > 3.46]$	0.445	0.0041	0.1458(26)
$[\chi SU(2)][a^2 + a^2\phi_2][m_\pi < 420\ MeV]$	0.452	0.0058	0.1446(16)
$[\chi SU(2)][a^2 + a^2\phi_2][m_\pi L > 4.1]$	0.7178	0.0102	0.1433(19)

Table K.3: Model average results for the determination of $\sqrt{t_0}$ at the physical point using the mixed actions results. In the first column we label the fit model and data cuts considered according to Table K.1. In the second and third columns we show the quality of fits as measured by the p-value [30] and the assigned weight to each model according to eq. (4.33), respectively. Finally, in the fourth column we show the results coming from each fit model. In all models the penalization of eq. (4.32) was included, so even in "no cut" models points at $\beta = 3.40$ and $m_\pi = 420$ MeV are penalized in the fit.

Combined analysis			
Model	p-value	W	$\sqrt{t_0}$ [fm]
$[\chi SU(3)][a^2][-]$	0.5532	0.0643	0.1440(6)
$[\chi SU(3)][a^2][\beta > 3.40]$	0.5048	0.0144	0.1438(8)
$[\chi SU(3)][a^2][\beta > 3.46]$	0.563	0.0023	0.1435(10)
$[\chi SU(3)][a^2][m_\pi < 420\ MeV]$	0.5018	0.0069	0.1438(6)
$[\chi SU(3)][a^2][\beta > 3.40\ \&\ m_\pi < 420\ MeV]$	0.4848	0.0004	0.1434(10)
$[\chi SU(3)][a^2][m_\pi < 350\ MeV]$	0.2552	0.0	0.1441(8)
$[\chi SU(3)][a^2][m_\pi L > 4.1]$	0.5842	0.0051	0.1441(7)
$[\chi SU(3)][a^2\alpha_s^{\hat{\Gamma}}][-]$	0.5544	0.0624	0.1441(6)
$[\chi SU(3)][a^2\alpha_s^{\hat{\Gamma}}][\beta > 3.40]$	0.4846	0.0125	0.1439(8)
$[\chi SU(3)][a^2\alpha_s^{\hat{\Gamma}}][\beta > 3.46]$	0.5774	0.0025	0.1435(10)
$[\chi SU(3)][a^2\alpha_s^{\hat{\Gamma}}][m_\pi < 420\ MeV]$	0.509	0.0068	0.1438(6)
$[\chi SU(3)][a^2\alpha_s^{\hat{\Gamma}}][\beta > 3.40\ \&\ m_\pi < 420\ MeV]$	0.5004	0.0004	0.1435(10)
$[\chi SU(3)][a^2\alpha_s^{\hat{\Gamma}}][m_\pi < 350\ MeV]$	0.256	0.0	0.1441(8)
$[\chi SU(3)][a^2\alpha_s^{\hat{\Gamma}}][m_\pi L > 4.1]$	0.5732	0.0047	0.1441(7)
$[\chi SU(3)][a^2][a^2 + a^2\phi_2][-]$	0.6826	0.0662	0.1436(6)
$[\chi SU(3)][a^2][a^2 + a^2\phi_2][\beta > 3.40]$	0.6092	0.0131	0.1435(9)
$[\chi SU(3)][a^2][a^2 + a^2\phi_2][\beta > 3.46]$	0.5142	0.0011	0.1434(10)
$[\chi SU(3)][a^2][a^2 + a^2\phi_2][m_\pi < 420\ MeV]$	0.5646	0.0045	0.1435(7)
$[\chi SU(3)][a^2][a^2 + a^2\phi_2][\beta > 3.40\ \&\ m_\pi < 420\ MeV]$	0.4148	0.0001	0.1433(10)
$[\chi SU(3)][a^2][a^2 + a^2\phi_2][m_\pi < 350\ MeV]$	0.196	0.0	0.1439(8)
$[\chi SU(3)][a^2][a^2 + a^2\phi_2][m_\pi L > 4.1]$	0.728	0.0045	0.1436(7)
$[\chi SU(3)][a^2 + a^2\phi_2][a^2][[-]$	0.5918	0.0382	0.1443(7)
$[\chi SU(3)][a^2 + a^2\phi_2][a^2][\beta > 3.40]$	0.5262	0.0074	0.1441(10)
$[\chi SU(3)][a^2 + a^2\phi_2][a^2][\beta > 3.46]$	0.5056	0.001	0.1436(11)
$[\chi SU(3)][a^2 + a^2\phi_2][a^2][m_\pi < 420\ MeV]$	0.5566	0.0039	0.1441(8)
$[\chi SU(3)][a^2 + a^2\phi_2][a^2][\beta > 3.40\ \&\ m_\pi < 420\ MeV]$	0.3996	0.0001	0.1435(11)

$[\chi SU(3)][a^2 + a^2\phi_2][a^2][m_\pi < 350\ MeV]$	0.1814	0.0	0.1440(9)
$[\chi SU(3)][a^2 + a^2\phi_2][a^2][m_\pi L > 4.1]$	0.6358	0.0029	0.1444(9)
$[\chi SU(3)][a^2 + a^2\phi_2][-]$	0.6618	0.0449	0.1433(9)
$[\chi SU(3)][a^2 + a^2\phi_2][\beta > 3.40]$	0.5704	0.0078	0.1430(13)
$[\chi SU(3)][a^2 + a^2\phi_2][\beta > 3.46]$	0.4598	0.0005	0.1430(16)
$[\chi SU(3)][a^2 + a^2\phi_2][m_\pi < 420\ MeV]$	0.5206	0.0019	0.1435(13)
$[\chi SU(3)][a^2 + a^2\phi_2][m_\pi L > 4.1]$	0.6816	0.0026	0.1432(13)
$[Tay][a^2][-]$	0.4414	0.0288	0.1445(6)
$[Tay][a^2][\beta > 3.40]$	0.3932	0.0066	0.1443(8)
$[Tay][a^2][\beta > 3.46]$	0.4464	0.0011	0.1439(9)
$[Tay][a^2][m_\pi < 420\ MeV]$	0.4204	0.0033	0.1442(6)
$[Tay][a^2][\beta > 3.40\ \&\ m_\pi < 420\ MeV]$	0.3812	0.0002	0.1439(10)
$[Tay][a^2][m_\pi < 350\ MeV]$	0.1684	0.0	0.1444(7)
$[Tay][a^2][m_\pi L > 4.1]$	0.5902	0.005	0.1445(6)
$[Tay][a^2\alpha_s^{\hat{\Gamma}}][-]$	0.4354	0.0282	0.1445(6)
$[Tay][a^2\alpha_s^{\hat{\Gamma}}][\beta > 3.40]$	0.376	0.0058	0.1443(8)
$[Tay][a^2\alpha_s^{\hat{\Gamma}}][\beta > 3.46]$	0.4536	0.0012	0.1440(9)
$[Tay][a^2\alpha_s^{\hat{\Gamma}}][m_\pi < 420\ MeV]$	0.4206	0.0034	0.1443(6)
$[Tay][a^2\alpha_s^{\hat{\Gamma}}][\beta > 3.40\ \&\ m_\pi < 420\ MeV]$	0.3834	0.0002	0.1439(10)
$[Tay][a^2\alpha_s^{\hat{\Gamma}}][m_\pi < 350\ MeV]$	0.1644	0.0	0.1444(7)
$[Tay][a^2\alpha_s^{\hat{\Gamma}}][m_\pi L > 4.1]$	0.5768	0.005	0.1445(6)
$[Tay][a^2][a^2 + a^2\phi_2][-]$	0.5704	0.0351	0.1441(6)
$[Tay][a^2][a^2 + a^2\phi_2][\beta > 3.40]$	0.4726	0.0063	0.1439(8)
$[Tay][a^2][a^2 + a^2\phi_2][\beta > 3.46]$	0.3966	0.0005	0.1438(10)
$[Tay][a^2][a^2 + a^2\phi_2][m_\pi < 420\ MeV]$	0.4516	0.0024	0.1440(6)
$[Tay][a^2][a^2 + a^2\phi_2][\beta > 3.40\ \&\ m_\pi < 420\ MeV]$	0.3102	0.0001	0.1438(10)
$[Tay][a^2][a^2 + a^2\phi_2][m_\pi < 350\ MeV]$	0.127	0.0	0.1442(8)
$[Tay][a^2][a^2 + a^2\phi_2][m_\pi L > 4.1]$	0.749	0.0052	0.1441(7)
$[Tay][a^2 + a^2\phi_2][a^2][-]$	0.4672	0.0163	0.1447(6)
$[Tay][a^2 + a^2\phi_2][a^2][\beta > 3.40]$	0.3892	0.0032	0.1445(8)
$[Tay][a^2 + a^2\phi_2][a^2][\beta > 3.46]$	0.382	0.0005	0.1440(10)
$[Tay][a^2 + a^2\phi_2][a^2][m_\pi < 420\ MeV]$	0.4404	0.0019	0.1445(7)
$[Tay][a^2 + a^2\phi_2][a^2][\beta > 3.40\ \&\ m_\pi < 420\ MeV]$	0.3142	0.0001	0.1439(10)
$[Tay][a^2 + a^2\phi_2][a^2][m_\pi < 350\ MeV]$	0.1104	0.0	0.1444(8)
$[Tay][a^2 + a^2\phi_2][a^2][m_\pi L > 4.1]$	0.6274	0.0028	0.1448(7)
$[Tay][a^2 + a^2\phi_2][-]$	0.5658	0.0256	0.1435(9)
$[Tay][a^2 + a^2\phi_2][\beta > 3.40]$	0.4734	0.0043	0.1432(12)
$[Tay][a^2 + a^2\phi_2][\beta > 3.46]$	0.366	0.0003	0.1432(16)

$[Tay][a^2 + a^2\phi_2][m_\pi < 420\ MeV]$	0.4296	0.0011	0.1437(12)
$[Tay][a^2 + a^2\phi_2][m_\pi L > 4.1]$	0.7382	0.0038	0.1432(12)
$[Tay4][a^2][-]$	0.5152	0.0326	0.1437(8)
$[Tay4][a^2][\beta > 3.40]$	0.4556	0.0075	0.1435(10)
$[Tay4][a^2][\beta > 3.46]$	0.4954	0.0009	0.1433(11)
$[Tay4][a^2][m_\pi < 420\ MeV]$	0.421	0.0025	0.1436(9)
$[Tay4][a^2][m_\pi L > 4.1]$	0.526	0.0019	0.1444(11)
$[Tay4][a^2][a^2 + a^2\phi_2][-]$	0.6136	0.0278	0.1434(8)
$[Tay4][a^2][a^2 + a^2\phi_2][\beta > 3.40]$	0.5278	0.0053	0.1432(10)
$[Tay4][a^2][a^2 + a^2\phi_2][\beta > 3.46]$	0.4324	0.0004	0.1432(11)
$[Tay4][a^2][a^2 + a^2\phi_2][m_\pi < 420\ MeV]$	0.4832	0.0015	0.1434(9)
$[Tay4][a^2][a^2 + a^2\phi_2][m_\pi L > 4.1]$	0.684	0.0022	0.1442(11)
$[Tay4][a^2 + a^2\phi_2][a^2][-]$	0.5848	0.0271	0.1438(8)
$[Tay4][a^2 + a^2\phi_2][a^2][\beta > 3.40]$	0.4926	0.0044	0.1437(10)
$[Tay4][a^2 + a^2\phi_2][a^2][\beta > 3.46]$	0.4322	0.0004	0.1434(11)
$[Tay4][a^2 + a^2\phi_2][a^2][m_\pi < 420\ MeV]$	0.4808	0.0016	0.1438(9)
$[Tay4][a^2 + a^2\phi_2][a^2][m_\pi L > 4.1]$	0.569	0.0012	0.1446(11)
$[Tay4][a^2 + a^2\phi_2][-]$	0.5774	0.0166	0.1434(9)
$[Tay4][a^2 + a^2\phi_2][\beta > 3.40]$	0.4794	0.0027	0.1432(12)
$[Tay4][a^2 + a^2\phi_2][\beta > 3.46]$	0.3748	0.0002	0.1436(16)
$[Tay4][a^2 + a^2\phi_2][m_\pi < 420\ MeV]$	0.429	0.0008	0.1438(12)
$[Tay4][a^2 + a^2\phi_2][m_\pi L > 4.1]$	0.7878	0.0027	0.1432(12)
$[\chi SU(2)][a^2][-]$	0.5694	0.0484	0.1436(7)
$[\chi SU(2)][a^2][\beta > 3.40]$	0.5146	0.0115	0.1434(9)
$[\chi SU(2)][a^2][\beta > 3.46]$	0.5484	0.0014	0.1433(10)
$[\chi SU(2)][a^2][m_\pi < 420\ MeV]$	0.4556	0.0031	0.1437(8)
$[\chi SU(2)][a^2][m_\pi L > 4.1]$	0.5296	0.0027	0.1439(8)
$[\chi SU(2)][a^2\alpha_s^{\hat{\Gamma}}][-]$	0.5572	0.0497	0.1437(7)
$[\chi SU(2)][a^2\alpha_s^{\hat{\Gamma}}][\beta > 3.40]$	0.4862	0.01	0.1435(9)
$[\chi SU(2)][a^2\alpha_s^{\hat{\Gamma}}][\beta > 3.46]$	0.548	0.0015	0.1434(10)
$[\chi SU(2)][a^2\alpha_s^{\hat{\Gamma}}][m_\pi < 420\ MeV]$	0.4534	0.0029	0.1437(8)
$[\chi SU(2)][a^2\alpha_s^{\hat{\Gamma}}][m_\pi L > 4.1]$	0.5098	0.0025	0.1439(8)
$[\chi SU(2)][a^2][a^2 + a^2\phi_2][-]$	0.6798	0.0475	0.1434(7)
$[\chi SU(2)][a^2][a^2 + a^2\phi_2][\beta > 3.40]$	0.5846	0.0086	0.1432(9)
$[\chi SU(2)][a^2][a^2 + a^2\phi_2][\beta > 3.46]$	0.4866	0.0007	0.1432(10)
$[\chi SU(2)][a^2][a^2 + a^2\phi_2][m_\pi < 420\ MeV]$	0.5148	0.0018	0.1434(9)
$[\chi SU(2)][a^2][a^2 + a^2\phi_2][m_\pi L > 4.1]$	0.6726	0.0022	0.1436(8)
$[\chi SU(2)][a^2 + a^2\phi_2][a^2][-]$	0.6388	0.0394	0.1438(7)

$[\chi SU(2)][a^2 + a^2\phi_2][a^2][\beta > 3.40]$	0.5476	0.0059	0.1437(10)
$[\chi SU(2)][a^2 + a^2\phi_2][a^2][\beta > 3.46]$	0.4886	0.0006	0.1434(10)
$[\chi SU(2)][a^2 + a^2\phi_2][a^2][m_\pi < 420 \, MeV]$	0.5146	0.0019	0.1438(9)
$[\chi SU(2)][a^2 + a^2\phi_2][a^2][m_\pi L > 4.1]$	0.5846	0.0016	0.1441(8)
$[\chi SU(2)][a^2 + a^2\phi_2][-]$	0.635	0.0275	0.1432(10)
$[\chi SU(2)][a^2 + a^2\phi_2][\beta > 3.40]$	0.5424	0.0039	0.1429(14)
$[\chi SU(2)][a^2 + a^2\phi_2][\beta > 3.46]$	0.416	0.0003	0.1430(19)
$[\chi SU(2)][a^2 + a^2\phi_2][m_\pi < 420 \, MeV]$	0.4556	0.0009	0.1435(13)
$[\chi SU(2)][a^2 + a^2\phi_2][m_\pi L > 4.1]$	0.6594	0.0016	0.1426(15)

Table K.4: Model average results for the determination of $\sqrt{t_0}$ at the physical point using the combined analysis of both Wilson and mixed action results. In the first column we label the fit model and data cuts considered according to Table K.1. In the second and third columns we show the quality of fits as measured by the p-value [30] and the assigned weight to each model according to eq. (4.33), respectively. Finally, in the fourth column we show the results coming from each fit model. In all models the penalization of eq. (4.32) was included, so even in "no cut" models points at $\beta = 3.40$ and $m_\pi = 420$ MeV are penalized in the fit.

BIBLIOGRAPHY

[1] Stephen L. Adler. "An Overrelaxation Method for the Monte Carlo Evaluation of the Partition Function for Multiquadratic Actions." In: *Phys. Rev. D* 23 (1981), p. 2901. DOI: 10.1103/PhysRevD.23.2901.

[2] I. Allison et al. "High-Precision Charm-Quark Mass from Current-Current Correlators in Lattice and Continuum QCD." In: *Phys. Rev. D* 78 (2008), p. 054513. DOI: 10.1103/PhysRevD.78.054513. arXiv: 0805.2999 [hep-lat].

[3] C. Allton et al. "Physical Results from 2+1 Flavor Domain Wall QCD and SU(2) Chiral Perturbation Theory." In: *Phys. Rev. D* 78 (2008), p. 114509. DOI: 10.1103/PhysRevD.78.114509. arXiv: 0804.0473 [hep-lat].

[4] S. Aoki et al. "Review of lattice results concerning low-energy particle physics." In: *Eur. Phys. J. C* 77.2 (2017), p. 112. DOI: 10.1140/epjc/s10052-016-4509-7. arXiv: 1607.00299 [hep-lat].

[5] Y. Aoki et al. "FLAG Review 2021." In: *Eur. Phys. J. C* 82.10 (2022), p. 869. DOI: 10.1140/epjc/s10052-022-10536-1. arXiv: 2111.09849 [hep-lat].

[6] T. Aoyama et al. "The anomalous magnetic moment of the muon in the Standard Model." In: *Phys. Rept.* 887 (2020), pp. 1–166. DOI: 10.1016/j.physrep.2020.07.006. arXiv: 2006.04822 [hep-ph].

[7] P. A. Baikov, K. G. Chetyrkin, and J. H. Kühn. "Quark Mass and Field Anomalous Dimensions to $\mathcal{O}(\alpha_s^5)$." In: *JHEP* 10 (2014), p. 076. DOI: 10.1007/JHEP10(2014)076. arXiv: 1402.6611 [hep-ph].

[8] P. A. Baikov, K. G. Chetyrkin, and J. H. Kühn. "Five-Loop Running of the QCD coupling constant." In: *Phys. Rev. Lett.* 118.8 (2017), p. 082002. DOI: 10.1103/PhysRevLett.118.082002. arXiv: 1606.08659 [hep-ph].

[9] P. A. Baikov, K. G. Chetyrkin, and J. H. Kühn. "Five-loop fermion anomalous dimension for a general gauge group from four-loop massless propagators." In: *JHEP* 04 (2017), p. 119. DOI: 10.1007/JHEP04(2017)119. arXiv: 1702.01458 [hep-ph].

[10] Gunnar S. Bali, Sara Collins, Peter Georg, Daniel Jenkins, Piotr Korcyl, Andreas Schäfer, Enno E. Scholz, Jakob Simeth, Wolfgang Söldner, and Simon Weishäupl. "Scale setting and the light baryon spectrum in $N_f = 2 + 1$ QCD with Wil-

son fermions." In: *JHEP* 05 (2023), p. 035. DOI: 10.1007/JHEP05(2023)035. arXiv: 2211.03744 [hep-lat].

[11] Oliver Bar and Maarten Golterman. "Chiral perturbation theory for gradient flow observables." In: *Phys. Rev. D* 89.3 (2014). [Erratum: Phys.Rev.D 89, 099905 (2014)], p. 034505. DOI: 10.1103/PhysRevD.89.034505. arXiv: 1312.4999 [hep-lat].

[12] A. Bazavov et al. "B- and D-meson decay constants from three-flavor lattice QCD." In: *Phys. Rev. D* 85 (2012), p. 114506. DOI: 10.1103/PhysRevD.85.114506. arXiv: 1112.3051 [hep-lat].

[13] A. Bazavov et al. "Gradient flow and scale setting on MILC HISQ ensembles." In: *Phys. Rev. D* 93.9 (2016), p. 094510. DOI: 10.1103/PhysRevD.93.094510. arXiv: 1503.02769 [hep-lat].

[14] A. Bazavov et al. "*B*- and *D*-meson leptonic decay constants from four-flavor lattice QCD." In: *Phys. Rev. D* 98.7 (2018), p. 074512. DOI: 10.1103/PhysRevD.98.074512. arXiv: 1712.09262 [hep-lat].

[15] G. W. Bennett et al. "Final Report of the Muon E821 Anomalous Magnetic Moment Measurement at BNL." In: *Phys. Rev. D* 73 (2006), p. 072003. DOI: 10.1103/PhysRevD.73.072003. arXiv: hep-ex/0602035.

[16] Claude W. Bernard, Tom Burch, Kostas Orginos, Doug Toussaint, Thomas A. DeGrand, Carleton E. DeTar, Steven A. Gottlieb, Urs M. Heller, James E. Hetrick, and Bob Sugar. "The Static quark potential in three flavor QCD." In: *Phys. Rev. D* 62 (2000), p. 034503. DOI: 10.1103/PhysRevD.62.034503. arXiv: hep-lat/0002028.

[17] W. Bietenholz et al. "Flavour blindness and patterns of flavour symmetry breaking in lattice simulations of up, down and strange quarks." In: *Phys. Rev. D* 84 (2011), p. 054509. DOI: 10.1103/PhysRevD.84.054509. arXiv: 1102.5300 [hep-lat].

[18] Benoit Blossier, Michele Della Morte, Georg von Hippel, Tereza Mendes, and Rainer Sommer. "On the generalized eigenvalue method for energies and matrix elements in lattice field theory." In: *JHEP* 04 (2009), p. 094. DOI: 10.1088/1126-6708/2009/04/094. arXiv: 0902.1265 [hep-lat].

[19] T. Blum et al. "Domain wall QCD with physical quark masses." In: *Phys. Rev. D* 93.7 (2016), p. 074505. DOI: 10.1103/PhysRevD.93.074505. arXiv: 1411.7017 [hep-lat].

[20] V. G. Bornyakov et al. "Determining the scale in Lattice QCD." In: Dec. 2015. arXiv: 1512.05745 [hep-lat].

[21] V. G. Bornyakov et al. "Wilson flow and scale setting from lattice QCD." In: (Aug. 2015). arXiv: 1508.05916 [hep-lat].

[22] Sz. Borsanyi et al. "Leading hadronic contribution to the muon magnetic moment from lattice QCD." In: *Nature* 593.7857 (2021), pp. 51–55. DOI: 10.1038/s41586-021-03418-1. arXiv: 2002.12347 [hep-lat].

[23] Szabolcs Borsányi, Stephan Dürr, Zoltán Fodor, Christian Hoelbling, Sándor D. Katz, Stefan Krieg, Thorsten Kurth, Laurent Lellouch, Thomas Lippert, and Craig McNeile. "High-precision scale setting in lattice QCD." In: *JHEP* 09 (2012), p. 010. DOI: 10.1007/JHEP09(2012)010. arXiv: 1203.4469 [hep-lat].

[24] Philippe Boucaud et al. "Dynamical Twisted Mass Fermions with Light Quarks: Simulation and Analysis Details." In: *Comput. Phys. Commun.* 179 (2008), pp. 695–715. DOI: 10.1016/j.cpc.2008.06.013. arXiv: 0803.0224 [hep-lat].

[25] Peter A. Boyle, Luigi Del Debbio, Nicolas Garron, Andreas Juttner, Amarjit Soni, Justus Tobias Tsang, and Oliver Witzel. "SU(3)-breaking ratios for $D_{(s)}$ and $B_{(s)}$ mesons." In: (Dec. 2018). arXiv: 1812.08791 [hep-lat].

[26] Peter A. Boyle, Luigi Del Debbio, Andreas Jüttner, Ava Khamseh, Francesco Sanfilippo, and Justus Tobias Tsang. "The decay constants $\mathbf{f_D}$ and $\mathbf{f_{D_s}}$ in the continuum limit of $= \mathbf{2+1}$ domain wall lattice QCD." In: *JHEP* 12 (2017), p. 008. DOI: 10.1007/JHEP12(2017)008. arXiv: 1701.02644 [hep-lat].

[27] Nathan Joseph Brown. "Lattice Scales from Gradient Flow and Chiral Analysis on the MILC Collaboration's HISQ Ensembles." PhD thesis. Washington U., St. Louis, Washington U., St. Louis, 2018. DOI: 10.7936/K7S181ZQ.

[28] Mattia Bruno, Mattia Dalla Brida, Patrick Fritzsch, Tomasz Korzec, Alberto Ramos, Stefan Schaefer, Hubert Simma, Stefan Sint, and Rainer Sommer. "QCD Coupling from a Nonperturbative Determination of the Three-Flavor Λ Parameter." In: *Phys. Rev. Lett.* 119.10 (2017), p. 102001. DOI: 10.1103/PhysRevLett.119.102001. arXiv: 1706.03821 [hep-lat].

[29] Mattia Bruno, Tomasz Korzec, and Stefan Schaefer. "Setting the scale for the CLS $2+1$ flavor ensembles." In: *Phys. Rev. D* 95.7 (2017), p. 074504. DOI: 10.1103/PhysRevD.95.074504. arXiv: 1608.08900 [hep-lat].

[30] Mattia Bruno and Rainer Sommer. "On fits to correlated and auto-correlated data." In: *Comput. Phys. Commun.* 285 (2023), p. 108643. DOI: 10.1016/j.cpc.2022.108643. arXiv: 2209.14188 [hep-lat].

[31] Mattia Bruno et al. "Simulation of QCD with $N_f = 2+1$ flavors of non-perturbatively improved Wilson fermions." In: *JHEP* 02 (2015), p. 043. DOI: 10.1007/JHEP02(2015)043. arXiv: 1411.3982 [hep-lat].

[32] John Bulava, Michele Della Morte, Jochen Heitger, and Christian Wittemeier. "Non-perturbative improvement of the axial current in N_f=3 lattice QCD with Wilson fermions and tree-level improved gauge action." In: *Nucl. Phys. B* 896 (2015), pp. 555–568. DOI: 10.1016/j.nuclphysb.2015.05.003. arXiv: 1502.04999 [hep-lat].

[33] Andrea Bussone, Alessandro Conigli, Julien Frison, Gregorio Herdoíza, Carlos Pena, David Preti, José Ángel Romero, Alejandro Sáez, and Javier Ugarrio. "Hadronic physics from a Wilson fermion mixed-action approach: Setup and scale setting." In: *to appear* ().

[34] Andrea Bussone, Alessandro Conigli, Julien Frison, Gregorio Herdoíza, Carlos Pena, David Preti, Alejandro Sáez, and Javier Ugarrio. "Hadronic physics from a Wilson fermion mixed-action approach: charm quark mass and $D_{(s)}$ meson decay constants." In: *Eur. Phys. J. C* 84.5 (2024), p. 506. DOI: 10.1140/epjc/s10052-024-12816-4. arXiv: 2309.14154 [hep-lat].

[35] Isabel Campos, Patrick Fritzsch, Carlos Pena, David Preti, Alberto Ramos, and Anastassios Vladikas. "Non-perturbative quark mass renormalisation and running in $N_f = 3$ QCD." In: *Eur. Phys. J. C* 78.5 (2018), p. 387. DOI: 10.1140/epjc/s10052-018-5870-5. arXiv: 1802.05243 [hep-lat].

[36] Bernat Capdevila, Andreas Crivellin, and Joaquim Matias. "Review of semileptonic B anomalies." In: *Eur. Phys. J. ST* 1 (2023), p. 20. DOI: 10.1140/epjs/s11734-023-01012-2. arXiv: 2309.01311 [hep-ph].

[37] Ying Chen, Wei-Feng Chiu, Ming Gong, Zhaofeng Liu, and Yunheng Ma. "Charmed and ϕ meson decay constants from 2+1-flavor lattice QCD." In: *Chin. Phys. C* 45.2 (2021), p. 023109. DOI: 10.1088/1674-1137/abcd8f. arXiv: 2008.05208 [hep-lat].

[38] K. G. Chetyrkin, Johann H. Kuhn, and M. Steinhauser. "Run-Dec: A Mathematica package for running and decoupling of the strong coupling and quark masses." In: *Comput. Phys. Commun.* 133 (2000), pp. 43–65. DOI: 10.1016/S0010-4655(00)00155-7. arXiv: hep-ph/0004189.

[39] M. A. Clark and A. D. Kennedy. "Accelerating dynamical fermion computations using the rational hybrid Monte Carlo (RHMC) algorithm with multiple pseudofermion fields." In: *Phys. Rev. Lett.* 98 (2007), p. 051601. DOI: 10.1103/PhysRevLett.98.051601. arXiv: hep-lat/0608015.

[40] Gilberto Colangelo and Stephan Durr. "The Pion mass in finite volume." In: *Eur. Phys. J. C* 33 (2004), pp. 543–553. DOI: 10.1140/epjc/s2004-01593-y. arXiv: hep-lat/0311023.

[41]   Gilberto Colangelo, Stephan Durr, and Christoph Haefeli. "Finite volume effects for meson masses and decay constants." In: *Nucl. Phys. B* 721 (2005), pp. 136–174. DOI: 10.1016/j.nuclphysb.2005.05.015. arXiv: hep-lat/0503014.

[42]   Sara Collins, Kevin Eckert, Jochen Heitger, Stefan Hofmann, and Wolfgang Soeldner. "Charmed pseudoscalar decay constants on three-flavour CLS ensembles with open boundaries." In: *PoS* LATTICE2016 (2017), p. 368. DOI: 10.22323/1.256.0368. arXiv: 1701.05502 [hep-lat].

[43]   B. Colquhoun, C. T. H. Davies, R. J. Dowdall, J. Kettle, J. Koponen, G. P. Lepage, and A. T. Lytle. "B-meson decay constants: a more complete picture from full lattice QCD." In: *Phys. Rev. D* 91.11 (2015), p. 114509. DOI: 10.1103/PhysRevD.91.114509. arXiv: 1503.05762 [hep-lat].

[44]   Brian Colquhoun, Laurence J. Cooper, Christine T. H. Davies, and G. Peter Lepage. "Precise determination of decay rates for $\eta_c \to \gamma\gamma$, $J/\psi \to \gamma\eta_c$, and $J/\psi \to \eta_c e^+ e^-$ from lattice QCD." In: *Phys. Rev. D* 108.1 (2023), p. 014513. DOI: 10.1103/PhysRevD.108.014513. arXiv: 2305.06231 [hep-lat].

[45]   M. Creutz. "Monte Carlo Study of Quantized SU(2) Gauge Theory." In: *Phys. Rev. D* 21 (1980), pp. 2308–2315. DOI: 10.1103/PhysRevD.21.2308.

[46]   Michael Creutz. "Overrelaxation and Monte Carlo Simulation." In: *Phys. Rev. D* 36 (1987), p. 515. DOI: 10.1103/PhysRevD.36.515.

[47]   Mattia Dalla Brida, Patrick Fritzsch, Tomasz Korzec, Alberto Ramos, Stefan Sint, and Rainer Sommer. "Slow running of the Gradient Flow coupling from 200 MeV to 4 GeV in $N_f = 3$ QCD." In: *Phys. Rev. D* 95.1 (2017), p. 014507. DOI: 10.1103/PhysRevD.95.014507. arXiv: 1607.06423 [hep-lat].

[48]   Mattia Dalla Brida, Roman Höllwieser, Francesco Knechtli, Tomasz Korzec, Alessandro Nada, Alberto Ramos, Stefan Sint, and Rainer Sommer. "Determination of $\alpha_s(m_Z)$ by the nonperturbative decoupling method." In: *Eur. Phys. J. C* 82.12 (2022), p. 1092. DOI: 10.1140/epjc/s10052-022-10998-3. arXiv: 2209.14204 [hep-lat].

[49]   Mattia Dalla Brida, Tomasz Korzec, Stefan Sint, and Pol Vilaseca. "High precision renormalization of the flavour non-singlet Noether currents in lattice QCD with Wilson quarks." In: *Eur. Phys. J. C* 79.1 (2019), p. 23. DOI: 10.1140/epjc/s10052-018-6514-5. arXiv: 1808.09236 [hep-lat].

[50] C. T. H. Davies, C. McNeile, E. Follana, G. P. Lepage, H. Na, and J. Shigemitsu. "Update: Precision D_s decay constant from full lattice QCD using very fine lattices." In: *Phys. Rev. D* 82 (2010), p. 114504. DOI: 10.1103/PhysRevD.82.114504. arXiv: 1008.4018 [hep-lat].

[51] Thomas A. DeGrand. "A conditioning technique for matrix inversion for Wilson fermions." In: *Computer Physics Communications* 52.1 (1988), pp. 161–164. ISSN: 0010-4655. DOI: https://doi.org/10.1016/0010-4655(88)90180-4. URL: https://www.sciencedirect.com/science/article/pii/0010465588901804.

[52] G. M. de Divitiis, R. Petronzio, and N. Tantalo. "Distance preconditioning for lattice Dirac operators." In: *Phys. Lett. B* 692 (2010), pp. 157–160. DOI: 10.1016/j.physletb.2010.07.031. arXiv: 1006.4028 [hep-lat].

[53] Giulia Maria de Divitiis, Maurizio Firrotta, Jochen Heitger, Carl Christian Köster, and Anastassios Vladikas. "Non-perturbative determination of improvement b-coefficients in $N_f = 3$." In: *EPJ Web Conf.* 175 (2018). Ed. by M. Della Morte, P. Fritzsch, E. Gámiz Sánchez, and C. Pena Ruano, p. 10008. DOI: 10.1051/epjconf/201817510008. arXiv: 1710.07020 [hep-lat].

[54] G. C. Donald, C. T. H. Davies, R. J. Dowdall, E. Follana, K. Hornbostel, J. Koponen, G. P. Lepage, and C. McNeile. "Precision tests of the J/ψ from full lattice QCD: mass, leptonic width and radiative decay rate to η_c." In: *Phys. Rev. D* 86 (2012), p. 094501. DOI: 10.1103/PhysRevD.86.094501. arXiv: 1208.2855 [hep-lat].

[55] R. J. Dowdall et al. "The Upsilon spectrum and the determination of the lattice spacing from lattice QCD including charm quarks in the sea." In: *Phys. Rev. D* 85 (2012), p. 054509. DOI: 10.1103/PhysRevD.85.054509. arXiv: 1110.6887 [hep-lat].

[56] S. Duane, A. D. Kennedy, B. J. Pendleton, and D. Roweth. "Hybrid Monte Carlo." In: *Phys. Lett. B* 195 (1987), pp. 216–222. DOI: 10.1016/0370-2693(87)91197-X.

[57] Philippe de Forcrand, Margarita Garcia Perez, Hideo Matsufuru, Atsushi Nakamura, Irina Pushkina, Ion-Olimpiu Stamatescu, Tetsuya Takaishi, and Takashi Umeda. "Contribution of disconnected diagrams to the hyperfine splitting of charmonium." In: *JHEP* 08 (2004), p. 004. DOI: 10.1088/1126-6708/2004/08/004. arXiv: hep-lat/0404016.

[58] R. Frezzotti and G. C. Rossi. "Chirally improving Wilson fermions. 1. O(a) improvement." In: *JHEP* 08 (2004), p. 007. DOI: 10.1088/1126-6708/2004/08/007. arXiv: hep-lat/0306014.

[59] Roberto Frezzotti, Pietro Antonio Grassi, Stefan Sint, and Peter Weisz. "A Local formulation of lattice QCD without unphysical fermion zero modes." In: *Nucl. Phys. B Proc. Suppl.* 83 (2000). Ed. by M. Campostrini, S. Caracciolo, L. Cosmai, A. Di Giacomo, P. Rossi, and F. Rapuano, pp. 941–946. DOI: 10.1016/S0920-5632(00)91852-8. arXiv: hep-lat/9909003.

[60] Roberto Frezzotti, Pietro Antonio Grassi, Stefan Sint, and Peter Weisz. "Lattice QCD with a chirally twisted mass term." In: *JHEP* 08 (2001), p. 058. DOI: 10.1088/1126-6708/2001/08/058. arXiv: hep-lat/0101001.

[61] Roberto Frezzotti, Stefan Sint, and Peter Weisz. "O(a) improved twisted mass lattice QCD." In: *JHEP* 07 (2001), p. 048. DOI: 10.1088/1126-6708/2001/07/048. arXiv: hep-lat/0104014.

[62] Julien Frison. "Bayesian Inference for Contemporary Lattice Quantum Field Theory." In: *40th International Symposium on Lattice Field Theory*. Dec. 2023. arXiv: 2401.00577 [hep-lat].

[63] Christof Gattringer and Christian B. Lang. *Quantum chromodynamics on the lattice*. Vol. 788. Springer, 2010. DOI: 10.1007/978-3-642-01850-3.

[64] Howard Georgi. "An Effective Field Theory for Heavy Quarks at Low-energies." In: *Phys. Lett. B* 240 (1990), pp. 447–450. DOI: 10.1016/0370-2693(90)91128-X.

[65] Paul H. Ginsparg and Kenneth G. Wilson. "A Remnant of Chiral Symmetry on the Lattice." In: *Phys. Rev. D* 25 (1982), p. 2649. DOI: 10.1103/PhysRevD.25.2649.

[66] J. L. Goity. "Chiral perturbation theory for SU(3) breaking in heavy meson systems." In: *Phys. Rev. D* 46 (1992), pp. 3929–3936. DOI: 10.1103/PhysRevD.46.3929. arXiv: hep-ph/9206230.

[67] Steven A. Gottlieb, W. Liu, D. Toussaint, R. L. Renken, and R. L. Sugar. "Hybrid Molecular Dynamics Algorithms for the Numerical Simulation of Quantum Chromodynamics." In: *Phys. Rev. D* 35 (1987), pp. 2531–2542. DOI: 10.1103/PhysRevD.35.2531.

[68] A. Gray, I. Allison, C. T. H. Davies, Emel Dalgic, G. P. Lepage, J. Shigemitsu, and M. Wingate. "The Upsilon spectrum and m(b) from full lattice QCD." In: *Phys. Rev. D* 72 (2005), p. 094507. DOI: 10.1103/PhysRevD.72.094507. arXiv: hep-lat/0507013.

[69] Benjamin Grinstein, Elizabeth Ellen Jenkins, Aneesh V. Manohar, Martin J. Savage, and Mark B. Wise. "Chiral perturbation theory for f D(s) / f D and B B(s) / B B." In: *Nucl. Phys. B* 380 (1992), pp. 369–376. DOI: 10.1016/0550-3213(92)90248-A. arXiv: hep-ph/9204207.

[70] Martin Hasenbusch. "Speeding up the hybrid Monte Carlo algorithm for dynamical fermions." In: *Phys. Lett. B* 519 (2001), pp. 177–182. DOI: 10.1016/S0370-2693(01)01102-9. arXiv: hep-lat/0107019.

[71] D. Hatton, C. T. H. Davies, B. Galloway, J. Koponen, G. P. Lepage, and A. T. Lytle. "Charmonium properties from lattice QCD+QED : Hyperfine splitting, J/ψ leptonic width, charm quark mass, and a_μ^c." In: *Phys. Rev. D* 102.5 (2020), p. 054511. DOI: 10.1103/PhysRevD.102.054511. arXiv: 2005.01845 [hep-lat].

[72] Jochen Heitger, Fabian Joswig, and Simon Kuberski. "Determination of the charm quark mass in lattice QCD with $2+1$ flavours on fine lattices." In: *JHEP* 05 (2021), p. 288. DOI: 10.1007/JHEP05(2021)288. arXiv: 2101.02694 [hep-lat].

[73] M. Pilar Hernandez. "Lattice field theory fundamentals." In: *Les Houches Summer School: Session 93: Modern perspectives in lattice QCD: Quantum field theory and high performance computing*. Aug. 2009, pp. 1–91.

[74] Florian Herren and Matthias Steinhauser. "Version 3 of RunDec and CRunDec." In: *Comput. Phys. Commun.* 224 (2018), pp. 333–345. DOI: 10.1016/j.cpc.2017.11.014. arXiv: 1703.03751 [hep-ph].

[75] F. Herzog, B. Ruijl, T. Ueda, J. A. M. Vermaseren, and A. Vogt. "The five-loop beta function of Yang-Mills theory with fermions." In: *JHEP* 02 (2017), p. 090. DOI: 10.1007/JHEP02(2017)090. arXiv: 1701.01404 [hep-ph].

[76] Roman Höllwieser, Francesco Knechtli, and Tomasz Korzec. "Scale setting for $N_f = 3+1$ QCD." In: *Eur. Phys. J. C* 80.4 (2020), p. 349. DOI: 10.1140/epjc/s10052-020-7889-7. arXiv: 2002.02866 [hep-lat].

[77] Nikolai Husung. "Logarithmic corrections to O(a) and O(a^2) effects in lattice QCD with Wilson or Ginsparg–Wilson quarks." In: *Eur. Phys. J. C* 83.2 (2023). [Erratum: Eur.Phys.J.C 83, 144 (2023)], p. 142. DOI: 10.1140/epjc/s10052-023-11258-8. arXiv: 2206.03536 [hep-lat].

[78] Alan C. Irving, James C. Sexton, Eamonn Cahill, Joyce Garden, Balint Joo, Stephen M. Pickles, and Zbigniew Sroczynski. "Tuning actions and observables in lattice QCD." In: *Phys. Rev. D* 58 (1998), p. 114504. DOI: 10.1103/PhysRevD.58.114504. arXiv: hep-lat/9807015.

[79] Xiang-Dong Ji and M. J. Musolf. "Subleading logarithmic mass dependence in heavy meson form-factors." In: *Phys. Lett. B* 257 (1991), pp. 409–413. DOI: 10.1016/0370-2693(91)91916-J.

[80] A. D. Kennedy, Ivan Horvath, and Stefan Sint. "A New exact method for dynamical fermion computations with nonlocal actions." In: *Nucl. Phys. B Proc. Suppl.* 73 (1999). Ed. by Thomas A. DeGrand, Carleton E. DeTar, R. Sugar, and D. Toussaint, pp. 834–836. DOI: 10.1016/S0920-5632(99)85217-7. arXiv: hep-lat/9809092.

[81] Bartosz Kostrzewa et al. "Gradient-flow scale setting with $N_f = 2+1+1$ Wilson-clover twisted-mass fermions." In: *PoS* LATTICE2021 (2022), p. 131. DOI: 10.22323/1.396.0131. arXiv: 2111.14710 [hep-lat].

[82] G. Peter Lepage. "The Analysis of Algorithms for Lattice Field Theory." In: *Theoretical Advanced Study Institute in Elementary Particle Physics.* June 1989.

[83] Tao Liu and Matthias Steinhauser. "Decoupling of heavy quarks at four loops and effective Higgs-fermion coupling." In: *Phys. Lett. B* 746 (2015), pp. 330–334. DOI: 10.1016/j.physletb.2015.05.023. arXiv: 1502.04719 [hep-ph].

[84] M. Luscher and P. Weisz. "Computation of the Action for On-Shell Improved Lattice Gauge Theories at Weak Coupling." In: *Phys. Lett. B* 158 (1985), pp. 250–254. DOI: 10.1016/0370-2693(85)90966-9.

[85] M. Luscher and P. Weisz. "On-shell improved lattice gauge theories." In: *Commun. Math. Phys.* 98.3 (1985). [Erratum: Commun.Math.Phys. 98, 433 (1985)], p. 433. DOI: 10.1007/BF01205792.

[86] Martin Luscher. "Computational Strategies in Lattice QCD." In: *Les Houches Summer School: Session 93: Modern perspectives in lattice QCD: Quantum field theory and high performance computing.* Feb. 2010, pp. 331–399. arXiv: 1002.4232 [hep-lat].

[87] Martin Luscher. "Topology, the Wilson flow and the HMC algorithm." In: *PoS* LATTICE2010 (2010). Ed. by Giancarlo Rossi, p. 015. DOI: 10.22323/1.105.0015. arXiv: 1009.5877 [hep-lat].

[88] Martin Luscher and Filippo Palombi. "Fluctuations and reweighting of the quark determinant on large lattices." In: *PoS* LATTICE2008 (2008). Ed. by Christopher Aubin, Saul Cohen, Chris Dawson, Jozef Dudek, Robert Edwards, Balint Joo, Huey-Wen Lin, Kostas Orginos, David Richards, and Hank Thacker, p. 049. DOI: 10.22323/1.066.0049. arXiv: 0810.0946 [hep-lat].

[89] Martin Luscher and Stefan Schaefer. "Lattice QCD without topology barriers." In: *JHEP* 07 (2011), p. 036. DOI: 10.1007/JHEP07(2011)036. arXiv: 1105.4749 [hep-lat].

[90]   Martin Luscher and Stefan Schaefer. "Lattice QCD with open boundary conditions and twisted-mass reweighting." In: *Comput. Phys. Commun.* 184 (2013), pp. 519–528. DOI: `10.1016/j.cpc.2012.10.003`. arXiv: `1206.2809 [hep-lat]`.

[91]   Martin Luscher, Stefan Sint, Rainer Sommer, and Peter Weisz. "Chiral symmetry and O(a) improvement in lattice QCD." In: *Nucl. Phys. B* 478 (1996), pp. 365–400. DOI: `10.1016/0550-3213(96)00378-1`. arXiv: `hep-lat/9605038`.

[92]   Thomas Luthe, Andreas Maier, Peter Marquard, and York Schroder. "Complete renormalization of QCD at five loops." In: *JHEP* 03 (2017), p. 020. DOI: `10.1007/JHEP03(2017)020`. arXiv: `1701.07068 [hep-ph]`.

[93]   Thomas Luthe, Andreas Maier, Peter Marquard, and York Schröder. "Five-loop quark mass and field anomalous dimensions for a general gauge group." In: *JHEP* 01 (2017), p. 081. DOI: `10.1007/JHEP01(2017)081`. arXiv: `1612.05512 [hep-ph]`.

[94]   Martin Lüscher. "Properties and uses of the Wilson flow in lattice QCD." In: (2010). DOI: `10.1007/JHEP08(2010)071`. eprint: `arXiv:1006.4518`.

[95]   Neal Madras and Alan D. Sokal. "The Pivot algorithm: a highly efficient Monte Carlo method for selfavoiding walk." In: *J. Statist. Phys.* 50 (1988), pp. 109–186. DOI: `10.1007/BF01022990`.

[96]   Y. Maezawa and P. Petreczky. "Quark masses and strong coupling constant in 2+1 flavor QCD." In: *Phys. Rev. D* 94.3 (2016), p. 034507. DOI: `10.1103/PhysRevD.94.034507`. arXiv: `1606.08798 [hep-lat]`.

[97]   Aneesh V. Manohar and Mark B. Wise. "Heavy quark physics." In: *Camb. Monogr. Part. Phys. Nucl. Phys. Cosmol.* 10 (2000), pp. 1–191.

[98]   Robert D. Mawhinney. "Lattice QCD with zero, two and four quark flavors." In: *RHIC Summer Study 96: Brookhaven Theory Workshop on Relativistic Heavy Ions.* Nov. 1996. arXiv: `hep-lat/9705030`.

[99]   C. McNeile, C. T. H. Davies, E. Follana, K. Hornbostel, and G. P. Lepage. "High-Precision c and b Masses, and QCD Coupling from Current-Current Correlators in Lattice and Continuum QCD." In: *Phys. Rev. D* 82 (2010), p. 034512. DOI: `10.1103/PhysRevD.82.034512`. arXiv: `1004.4285 [hep-lat]`.

[100]   N. Metropolis, A. W. Rosenbluth, M. N. Rosenbluth, A. H. Teller, and E. Teller. "Equation of state calculations by fast computing machines." In: *J. Chem. Phys.* 21 (1953), pp. 1087–1092. DOI: `10.1063/1.1699114`.

[101] *Millennium Prize problems*. DOI: 10.1093/oi/authority.20110803100158288. URL: https://www.oxfordreference.com/view/10.1093/oi/authority.20110803100158288.

[102] Daniel Mohler and Stefan Schaefer. "Remarks on strange-quark simulations with Wilson fermions." In: *Phys. Rev. D* 102.7 (2020), p. 074506. DOI: 10.1103/PhysRevD.102.074506. arXiv: 2003.13359 [hep-lat].

[103] Daniel Mohler, Stefan Schaefer, and Jakob Simeth. "CLS 2+1 flavor simulations at physical light- and strange-quark masses." In: *EPJ Web Conf.* 175 (2018). Ed. by M. Della Morte, P. Fritzsch, E. Gámiz Sánchez, and C. Pena Ruano, p. 02010. DOI: 10.1051/epjconf/201817502010. arXiv: 1712.04884 [hep-lat].

[104] Heechang Na, Christine T. H. Davies, Eduardo Follana, G. Peter Lepage, and Junko Shigemitsu. "$|V_{cd}|$ from D Meson Leptonic Decays." In: *Phys. Rev. D* 86 (2012), p. 054510. DOI: 10.1103/PhysRevD.86.054510. arXiv: 1206.4936 [hep-lat].

[105] Katsumasa Nakayama, Brendan Fahy, and Shoji Hashimoto. "Short-distance charmonium correlator on the lattice with Möbius domain-wall fermion and a determination of charm quark mass." In: *Phys. Rev. D* 94.5 (2016), p. 054507. DOI: 10.1103/PhysRevD.94.054507. arXiv: 1606.01002 [hep-lat].

[106] Y. Namekawa et al. "Charm quark system at the physical point of 2+1 flavor lattice QCD." In: *Phys. Rev. D* 84 (2011), p. 074505. DOI: 10.1103/PhysRevD.84.074505. arXiv: 1104.4600 [hep-lat].

[107] Silvia Necco and Rainer Sommer. "The N(f) = 0 heavy quark potential from short to intermediate distances." In: *Nucl. Phys. B* 622 (2002), pp. 328–346. DOI: 10.1016/S0550-3213(01)00582-X. arXiv: hep-lat/0108008.

[108] Ethan T. Neil and Jacob W. Sitison. "Model averaging approaches to data subset selection." In: *Phys. Rev. E* 108.4 (2023), p. 045308. DOI: 10.1103/PhysRevE.108.045308. arXiv: 2305.19417 [stat.ME].

[109] Ethan T. Neil and Jacob W. Sitison. "Improved information criteria for Bayesian model averaging in lattice field theory." In: *Phys. Rev. D* 109.1 (2024), p. 014510. DOI: 10.1103/PhysRevD.109.014510. arXiv: 2208.14983 [stat.ME].

[110] Holger Bech Nielsen and M. Ninomiya. "Absence of Neutrinos on a Lattice. 1. Proof by Homotopy Theory." In: *Nucl. Phys. B* 185 (1981). Ed. by J. Julve and M. Ramón-Medrano. [Erratum: Nucl.Phys.B 195, 541 (1982)], p. 20. DOI: 10.1016/0550-3213(82)90011-6.

[111] Holger Bech Nielsen and M. Ninomiya. "No Go Theorem for Regularizing Chiral Fermions." In: *Phys. Lett. B* 105 (1981), pp. 219–223. DOI: 10.1016/0370-2693(81)91026-1.

[112] I.P. Omelyan, I.M. Mryglod, and R. Folk. "Symplectic analytically integrable decomposition algorithms: classification, derivation, and application to molecular dynamics, quantum and celestial mechanics simulations." In: *Computer Physics Communications* 151.3 (2003), pp. 272–314. ISSN: 0010-4655. DOI: https://doi.org/10.1016/S0010-4655(02)00754-3. URL: https://www.sciencedirect.com/science/article/pii/S0010465502007543.

[113] P. Petreczky and J. H. Weber. "Strong coupling constant and heavy quark masses in (2+1)-flavor QCD." In: *Phys. Rev. D* 100.3 (2019), p. 034519. DOI: 10.1103/PhysRevD.100.034519. arXiv: 1901.06424 [hep-lat].

[114] Alberto Ramos. "Automatic differentiation for error analysis of Monte Carlo data." In: *Comput. Phys. Commun.* 238 (2019), pp. 19–35. DOI: 10.1016/j.cpc.2018.12.020. arXiv: 1809.01289 [hep-lat].

[115] Alberto Ramos. "Automatic differentiation for error analysis." In: *PoS* TOOLS2020 (2021), p. 045. DOI: 10.22323/1.392.0045. arXiv: 2012.11183 [hep-lat].

[116] Giulia Ricciardi and Marcello Rotondo. "Determination of the Cabibbo-Kobayashi-Maskawa matrix element $|V_{cb}|$." In: *J. Phys. G* 47 (2020), p. 113001. DOI: 10.1088/1361-6471/ab9f01. arXiv: 1912.09562 [hep-ph].

[117] Stefan Schaefer, Rainer Sommer, and Francesco Virotta. "Critical slowing down and error analysis in lattice QCD simulations." In: *Nucl. Phys. B* 845 (2011), pp. 93–119. DOI: 10.1016/j.nuclphysb.2010.11.020. arXiv: 1009.5228 [hep-lat].

[118] Barbara Schmidt and Matthias Steinhauser. "CRunDec: a C++ package for running and decoupling of the strong coupling and quark masses." In: *Comput. Phys. Commun.* 183 (2012), pp. 1845–1848. DOI: 10.1016/j.cpc.2012.03.023. arXiv: 1201.6149 [hep-ph].

[119] B. Sheikholeslami and R. Wohlert. "Improved Continuum Limit Lattice Action for QCD with Wilson Fermions." In: *Nucl. Phys. B* 259 (1985), p. 572. DOI: 10.1016/0550-3213(85)90002-1.

[120] Andrea Shindler. "Twisted mass lattice QCD." In: *Phys. Rept.* 461 (2008), pp. 37–110. DOI: 10.1016/j.physrep.2008.03.001. arXiv: 0707.4093 [hep-lat].

[121] R. Sommer. "A New way to set the energy scale in lattice gauge theories and its applications to the static force and α_s in SU(2) Yang-Mills theory." In: *Nucl. Phys. B* 411 (1994), pp. 839–854. DOI: `10.1016/0550-3213(94)90473-1`. arXiv: `hep-lat/9310022`.

[122] Rainer Sommer. "Scale setting in lattice QCD." In: *PoS* LATTICE2013 (2014), p. 015. DOI: `10.22323/1.187.0015`. arXiv: `1401.3270 [hep-lat]`.

[123] Ben Straßberger. "Towards Higher Precision Lattice QCD Results: Improved Scale Setting and Domain Decomposition Solvers." PhD thesis. Humboldt U., Berlin, 2023. DOI: `10.18452/26517`.

[124] Ben Strassberger et al. "Scale setting for CLS 2+1 simulations." In: *PoS* LATTICE2021 (2022), p. 135. DOI: `10.22323/1.396.0135`. arXiv: `2112.06696 [hep-lat]`.

[125] Yusuke Taniguchi and Akira Ukawa. "Perturbative calculation of improvement coefficients to O(g**2a) for bilinear quark operators in lattice QCD." In: *Phys. Rev. D* 58 (1998), p. 114503. DOI: `10.1103/PhysRevD.58.114503`. arXiv: `hep-lat/9806015`.

[126] D. H. Weingarten and D. N. Petcher. "Monte Carlo Integration for Lattice Gauge Theories with Fermions." In: *Phys. Lett. B* 99 (1981), pp. 333–338. DOI: `10.1016/0370-2693(81)90112-X`.

[127] D. H. Weingarten and J. C. Sexton. "Hamiltonian evolution for the hybrid Monte Carlo algorithm." In: *Nucl. Phys. B Proc. Suppl.* 26 (1992), pp. 613–616. DOI: `10.1016/0920-5632(92)90349-W`.

[128] Frank Wilczek. "Quantum field theory." In: *Rev. Mod. Phys.* 71 (1999), S85–S95. DOI: `10.1103/RevModPhys.71.S85`. arXiv: `hep-th/9803075`.

[129] Kenneth G. Wilson. "Confinement of Quarks." In: *Phys. Rev. D* 10 (1974). Ed. by J. C. Taylor, pp. 2445–2459. DOI: `10.1103/PhysRevD.10.2445`.

[130] Ulli Wolff. "Monte Carlo errors with less errors." In: *Comput. Phys. Commun.* 156 (2004). [Erratum: Comput.Phys.Commun. 176, 383 (2007)], pp. 143–153. DOI: `10.1016/S0010-4655(03)00467-3`. arXiv: `hep-lat/0306017`.

[131] R. L. Workman et al. "Review of Particle Physics." In: *PTEP* 2022 (2022), p. 083C01. DOI: `10.1093/ptep/ptac097`.

[132] Yi-Bo Yang et al. "Charm and strange quark masses and f_{D_s} from overlap fermions." In: *Phys. Rev. D* 92.3 (2015), p. 034517. DOI: `10.1103/PhysRevD.92.034517`. arXiv: `1410.3343 [hep-lat]`.

[133] P. A. Zyla et al. "Review of Particle Physics." In: *PTEP* 2020.8 (2020), p. 083C01. DOI: `10.1093/ptep/ptaa104`.